UC Berkeley
UC Berkeley Electronic Theses and Dissertations

Title
Structural Characterization of and Plutonium Sorption on Mesoporous and Nanoparticulate Ferrihydrite

Permalink
https://escholarship.org/uc/item/8dn323kt

Author
Brogan, Luna Kestrel Schwaiger

Publication Date
2012

Peer reviewed|Thesis/dissertation

eScholarship.org Powered by the California Digital Library
University of California

Structural Characterization of and Plutonium Sorption on Mesoporous and Nanoparticulate Ferrihydrite

by

Luna Kestrel Schwaiger Brogan

A dissertation submitted in partial satisfaction of the
requirements for the degree of
Doctor of Philosophy

in

Chemistry

in the

Graduate Division
of the
University of California, Berkeley

Committee in charge:
Professor Heino Nitsche, Chair
Professor Peidong Yang
Professor Joonhong Ahn

Fall 2012

Structural Characterization of and Plutonium Sorption on Mesoporous and Nanoparticulate Ferrihydrite

Copyright 2012
by
Luna Kestrel Schwaiger Brogan

Abstract

Structural Characterization of and Plutonium Sorption on Mesoporous and Nanoparticulate Ferrihydrite

by

Luna Kestrel Schwaiger Brogan

Doctor of Philosophy in Chemistry

University of California, Berkeley

Professor Heino Nitsche, Chair

The interactions of plutonium with reactive metal oxide surfaces, such as iron oxide and oxyhydroxide minerals, is an area of great interest for scientists studying both environmental contaminant transport and actinide separation and sensing applications. The work presented here addresses both fields with the synthesis and characterization of two iron oxyhydroxide minerals.

The first mineral is manganese-substituted goethite, for which the synthesis and characterization were the primary concern. A wide range of percent substitutions were prepared, spanning from nearly zero percent up to twenty percent. These minerals were then characterized with respect to their structure, morphology, percent substitution, and solubility. Although smaller percent substitutions could be made, the minimum with a reliable concentration was around 0.5 %. Additionally, the manganese seemed to be more concentrated at the surface of the particles than at the center, suggesting an uneven distribution during particle formation. This trend was more pronounced for the lower substitutions. The 0.5 % and 1 % Mn-substituted goethite showed Fe solubility that matched well with published goethite solubility. The Mn solubility is less than other Mn oxides, but still significantly higher than Fe, which is expected.

The second mineral is ferrihydrite. For these studies three different 2-line ferrihydrite materials were synthesized and characterized: a suspended colloidal ferrihydrite, a dried and ground version of that suspension, and a nanocast mesoporous ferrihydrite. The data presented is an extended characterization of the structural and surface properties of these three materials, culminating in a study of the interactions of PuO_2^{2+} with the three materials as a function of pH, concentration, and light exposure.

All three materials were measured by X-ray diffraction to be 2-line ferrihydrite. The suspended ferrihydrite was measured to be in the expected 2-5 nm size range. The dried was considerably more aggregated, showing sizes from 20 nm up to 100 μm, and the mesoporous ferrihydrite ranged from 100 nm to 200 μm. The surface areas were also in agreement with the literature, with the dried ferrihydrite measuring at 300-350 m^2/g and the mesoporous ferrihydrite near 200 m^2/g. The point of zero charge, however, was very different from literature values at around pH 5.5 for the dried ferrihydrite and near pH 9 for the mesoporous

ferrihydrite. These values were supported by the plutonium sorption data though and suggest that although all three materials are 2-line ferrihydrite that the surfaces are dissimilar.

In batch sorption studies with Pu(VI), the suspended and dried ferrihydrite proved to be better plutonium scavengers than the mesoporous ferrihydrite, sorbing up to 22 milligrams of Pu per gram of solid compared to only 12 milligrams per gram. The mesoporous released the plutonium more reliably in desorption studies, further supporting the determination that the binding of Pu(VI) to the mesoporous ferrihydrite is not as strong as the binding to the dried and suspended ferrihydrite. All three materials were shown to be photocatalysts for the reduction of Pu(VI) to Pu(IV) using both batch sorption and X-ray absorption spectroscopy measurements, but under different conditions. Two mechanisms were suggested; one through the light-induced creation of Fe(II) in solution and the other through a direct surface electron transfer to the plutonium. Only the dried ferrihydrite exhibited this behavior under all conditions measured, but also demonstrated the weakest overall photocatalytic activity. The suspended ferrihydrite was only a weak photocatalyst at low pH, but was strong at higher pH conditions, likely due to high surface area and greater particle aggregation. The mesoporous ferrihydrite showed increasing photocatalytic activity with increasing pH, suggesting that the mesoporous ferrihydrite can only achieve a direct electron transfer and not the solution-mediated Fe(II) mechanism that the nanoparticulate ferrihydrite materials will undergo. These results highlight the differences between the surface chemistry and structure of these materials despite the fact that they are all 2-line ferrihydrite. This is particularly important for the understanding of the suspended and dried ferrihydrite, as distinctions between these two materials are not often considered.

For Lee, who waited so patiently and pushed when it was necessary.

Contents

List of Figures v

List of Tables x

1 Introduction 1

2 Plutonium Chemistry 4
2.1 Introduction . . . 4
2.2 Solution Chemistry . . . 4
2.2.1 Plutonium Redox Chemistry . . . 5
2.2.2 Plutonium Solubility and Speciation . . . 5
2.3 Preparation of Plutonium Solutions . . . 9
2.4 Alpha Particle-Induced Chemistry . . . 9
2.5 Plutonium Measurement with Liquid Scintillation Counting . . . 11

3 Surface Chemistry 14
3.1 Introduction . . . 14
3.2 Surface Complexation and Point of Zero Charge . . . 14
3.3 Semiconductor Surface Charge Transfer . . . 16

4 Manganese-Substituted Goethite 19
4.1 Introduction . . . 19
4.2 Synthesis . . . 20
4.3 Structure, Size, and Shape . . . 20
4.3.1 X-ray Diffraction . . . 20
4.3.2 Scanning Electron Microscopy . . . 21
4.4 Percent Substitution and Manganese Distribution . . . 25
4.5 Solubility of Mn-Substituted Goethite . . . 27

5 Ferrihydrite 30
5.1 Introduction . . . 30
5.2 Structure . . . 31
5.3 Synthesis . . . 32
5.3.1 Nanoparticulate Ferrihydrite . . . 32
5.3.2 Mesoporous Ferrihydrite . . . 34
5.4 Percent Composition . . . 36

5.5 Particle Size and Morphology . . . 38
5.6 X-ray Diffraction . . . 39
5.7 Surface Area Measurements . . . 42
5.7.1 Introduction . . . 42
5.7.2 BET Surface Area Measurements . . . 44
5.7.3 Problems with BET Measurements . . . 48
5.7.4 BET Surface Area Data . . . 49
5.7.5 Pore Size and Volume Measurements . . . 50
5.7.6 Problems with Pore Analysis Calculations . . . 53
5.7.7 Methylene Blue Surface Area Measurements . . . 53
5.8 Point of Zero Charge of Ferrihydrite . . . 55
5.8.1 Methods of Measurement of the PZC . . . 56
5.8.2 PZC Determination by Powder Addition . . . 57
5.8.3 PZC Determination by Mass Titration . . . 60
5.8.4 PZC Determination by Potentiometric Titration . . . 60
5.9 Plutonium Sorption onto Ferrihydrite . . . 61
5.9.1 Introduction . . . 61
5.9.2 Batch Studies . . . 62
5.9.3 Light-Induced Chemistry . . . 69
5.9.4 Plutonium Uptake Capacity Measurements . . . 78
5.9.5 Desorption Measurements . . . 80
5.9.6 XAS Measurements . . . 81

6 Conclusions **89**
6.1 Final Remarks . . . 89
6.2 Future Work . . . 90

Bibliography **93**

A Inductively Coupled Plasma Mass Spectrometry **107**
A.1 Introduction . . . 107
A.2 Advantages of the System . . . 107
A.3 Instrument Description . . . 107
A.4 Data Handling . . . 109
A.5 Preparation of Standards for ICP-MS . . . 110
A.6 Preparation of Samples for ICP-MS . . . 110
A.7 General Notes . . . 111
A.8 Fe Bleeding into the Mn Peak . . . 111

B Solubility of Cryptomelane and Pyrolusite **112**

C Acid Cleaning of Glassware **114**

D Ultrafiltration **118**
D.1 Introduction 118
D.2 Testing Filters With Transition Metals 119
D.2.1 Testing Results 120
D.3 Testing Filters with Plutonium(VI) 122
D.3.1 Testing Results 123

List of Figures

2.1 Plutonium(VI) exists as the 2+ plutonyl cation. . . . 4
2.2 Pourbaix diagram for plutonium in equilibrium with atmosphere. From Choppin *et al.* (1997) [18]. . . . 6
2.3 Plutonium solubility (non-hydrolyzed ions) as a function of pH as calculated by Choppin *et al.* (2002) [19]. . . . 7
2.4 Speciation diagram for Pu(VI) exposed to atmospheric carbonate. Solid lines represent the calculated data and dotted lines represent the asymmetric error bars to 1 σ. From Hu *et al.* (2010) and Hu (2011) [62, 61]. . . . 7
2.5 Pourbaix diagram for plutonium in an aqueous solution containing hydroxide, carbonate, and fluoride. The Eh/pH conditions found in natural waters are also outlined. From Runde (2000) [123]. . . . 8
2.6 Representative UV-visible spectrum of plutonium stocks used for experiments, which shows only Pu(VI) peaks. . . . 10
2.7 Approximate percentages of Pu(IV), Pu(V), and Pu(VI) in solution over time as a result of autoreduction. . . . 11

3.1 Surface charge below (top), at (center), and above (bottom) the point of zero charge. . . . 16

4.1 Diffraction of X-rays by a crystal. . . . 21
4.2 X-ray diffractograms of goethite and Mn-substituted goethite showing the shift in 2θ with increasing manganese substitution. . . . 22
4.3 Scanning electron micrograph of 1 % Mn-substituted goethite showing the morphology of the goethite particles. . . . 23
4.4 Scanning electron micrograph of 1 % Mn-substituted goethite showing the level of surface roughness and a broken joint between two particles that had aggregated during wet-mounting (arrow). Individual needle-shaped crystallites can almost be seen to form the surface. . . . 23
4.5 Scanning electron micrograph of 1 % Mn-substituted goethite showing the formation of the particle surface by the aggregation of small needle-shaped crystallites. . . . 24
4.6 Scanning electron micrograph of 0.5 % Mn-substituted goethite showing individual needle-shape crystallites broken off from a larger particle. . . . 24

4.7 Solubility of iron as a function of pH for 0.5 % and 1 % manganese-substituted goethite. Lines are added to guide the eye and vertical error bars of 1 σ are contained within the data points. 28
4.8 Solubility of manganese as a function of pH for 0.5 % and 1 % manganese-substituted goethite. Lines are added to guide the eye and vertical error bars of 1 σ are contained within the data points. 28

5.1 Hexagonal unit cell model for ferrihydrite. From Michel *et al.* (2007) [95]. . . 31
5.2 Possible sorption sites on ferrihydrite. Coordinating oxygens around the metal cations (blue) are generally not shown for simplicity. The boxed numbers indicate the number of possible second neighbors visible in EXAFS data. From Gilbert *et al.* (2009) [46]. 32
5.3 Transmission electron micrograph (TEM) of suspended ferrihydrite dried to a carbon grid. Right image shows approximate particle size measurements of particles visible in the left image. Diameters were measured using the software ruler feature. 33
5.4 Example EDS measurement of nanoparticulate ferrihydrite batch 8. 37
5.5 SEM image of dried ferrihydrite batch 8 showing the wide range of particle sizes. 39
5.6 SEM image of dried ferrihydrite batch 8 showing the surface roughness of particles. 40
5.7 SEM image of mesoporous ferrihydrite showing the range of particle sizes. . . 40
5.8 HR-TEM image of mesoporous ferrihydrite showing the mesoporous nature of the material. From H. Tüysüz. 41
5.9 X-ray diffractogram for 2-line ferrihydrite showing only two broad reflections. 41
5.10 X-ray diffractogram for 3D mesoporous 2-line ferrihydrite showing two broad reflections and the starts of some more crystalline peaks corresponding to hematite or 6-line ferrihydrite. 42
5.11 X-ray diffractogram for batch 8 showing stability as 2-line ferrihydrite for up to 5.5 months with no visible more crystalline peaks. 43
5.12 X-ray diffractogram for 2-line ferrihydrite showing two broad reflections as well as the more crystalline peaks of goethite and hematite. 43
5.13 Example pore shapes caused by the aggregation of same-sized spheres. 45
5.14 Shapes of the six common types of adsorption isotherms. From Klobes *et al.* (2006) [74]. 46
5.15 Shapes of the four common types of hysteresis found in adsorption isotherms. From Sing *et al.* (1985) [135]. 47
5.16 Representative dried ferrihydrite isotherm for those samples with hysteresis. 51
5.17 Representative dried ferrihydrite isotherm for those samples without hysteresis. 51
5.18 Representative mesoporous ferrihydrite isotherm. 52
5.19 Structure of the methylene blue molecule. 54
5.20 Representative plot of the type used for the determination of the point of zero charge of dried nanoparticulate ferrihydrite by the powder addition method. No error bars are calculated. The best fit line is a simple linear fit of the data. 58

5.21 Representative plot of the type used for the determination of the point of zero charge of 3D mesoporous ferrihydrite by the powder addition method. No error bars are calculated. The best fit line is a simple linear fit of the data. . 60
5.22 Plot of measured pH as a function of oxide:water ratio after 24 hours for dried ferrihydrite. No error bars are calculated. 61
5.23 Sorption curve for dried nanoparticulate ferrihydrite with 10 μM Pu(VI) in the light. The horizontal line indicates the μmoles of Pu originally added to the solution. 64
5.24 Sorption curve for suspended nanoparticulate ferrihydrite with 16 μM Pu(VI). The horizontal line indicates the μmoles of Pu originally added to the solution. 64
5.25 Sorption curve for suspended nanoparticulate ferrihydrite with 16 μM Pu(VI) compared to a Pu(VI) speciation diagram. The error bars on the speciation diagram have been removed for clarity. 65
5.26 Sorption curve for mesoporous ferrihydrite with 16 μM Pu(VI). The horizontal line indicates the μmoles of Pu originally added to the solution. 65
5.27 Sorption curve for dried nanoparticulate ferrihydrite with 16 μM Pu(VI) in the light. The horizontal line indicates the μmoles of Pu originally added to the solution. 66
5.28 Sorption curve for dried nanoparticulate ferrihydrite with 16 μM Pu(VI) without light-induced chemistry. The horizontal line indicates the μmoles of Pu originally added to the solution. 67
5.29 Sorption curve for suspended nanoparticulate ferrihydrite with 16 μM Pu(VI) without light-induced chemistry. The horizontal line indicates the μmoles of Pu originally added to the solution. 68
5.30 Sorption curve for mesoporous ferrihydrite with 16 μM Pu(VI) without light-induced chemistry. The horizontal line indicates the μmoles of Pu originally added to the solution. 68
5.31 Experimental data and model fit for sorption of 4.2 μM U(VI) to ferrihydrite in 0.01 M NaCl solution containing 0.01 M carbonate. From Wazne *et al.* (2003) [171]. 69
5.32 Speciation of 4.2 μM U(VI) in 0.01 M NaCl solution containing 0.01 M carbonate. From Wazne *et al.* (2003) [171]. 70
5.33 Sorption of 16 μM Pu on dried ferrihydrite as a function of light exposure. The vertical line indicates the deliberate exposure of the dark sample to light following the assay on day 23. The horizontal line indicates the μmoles of Pu originally added to the solution. 71
5.34 Sorption of 16 μM Pu on dried ferrihydrite when exposed to glovebox and laboratory lights. The horizontal line indicates the μmoles of Pu originally added to the solution. 71
5.35 Sorption of 16 μM Pu on dried ferrihydrite shielded from glovebox and laboratory lights. The vertical line indicates the deliberate exposure of the sample to light. The horizontal line indicates the μmoles of Pu originally added to the solution. 72

5.36 Sorption of 16 μM Pu on suspended ferrihydrite when exposed to glovebox and laboratory lights. The horizontal line indicates the μmoles of Pu originally added to the solution. 72
5.37 Sorption of 16 μM Pu on suspended ferrihydrite shielded from glovebox and laboratory lights. The vertical line indicates the deliberate exposure of the sample to light. The horizontal line indicates the μmoles of Pu originally added to the solution. 73
5.38 Sorption of 16 μM Pu on mesoporous ferrihydrite when exposed to glovebox and laboratory lights. The horizontal line indicates the μmoles of Pu originally added to the solution. 73
5.39 Sorption of 16 μM Pu on mesoporous ferrihydrite shielded from glovebox and laboratory lights. The vertical line indicates the deliberate exposure of the sample to light. The horizontal line indicates the μmoles of Pu originally added to the solution. 74
5.40 Sorption of 16 μM Pu on suspended "ferri-goethite" when exposed to glovebox and laboratory lights. The horizontal line indicates the μmoles of Pu originally added to the solution. 75
5.41 Sorption of 16 μM Pu on suspended "ferri-goethite" shielded from glovebox and laboratory lights. The vertical line indicates the deliberate exposure of the sample to light. The horizontal line indicates the μmoles of Pu originally added to the solution. 75
5.42 Emission spectrum of the fluorescent light bulbs used in the glovebox and for the general laboratory lighting for plutonium sorption experiments as measured by an Ocean Optics USB2000 spectrometer from 400 to 800 nm. The spectrum has not been energy or intensity calibrated. Comparison of the mercury line at 546.074 nm [118] to the spectrum suggests that the measured wavelengths are red shifted by about 1.5 nm. 76
5.43 Representative Pu L_{III} edge XAS spectrum with the XANES and EXAFS regions labeled. Courtesy of D. L. Wang. 82
5.44 Standard XANES spectra used for fitting Pu(IV), Pu(V), and Pu(VI) during XAS data processing. The shoulder from about 18070 to 18090 eV caused by scattering from the axial oxygens is clearly visible for Pu(V) and Pu(VI), and missing for Pu(IV). The edge shift based on oxidation state is also visible. [22, 110] 84
5.45 Fit of experimental XANES data to Pu(IV), Pu(V), and Pu(VI) standard XANES spectra for dried ferrihydrite at pH 7.77, which was kept in the dark as much as possible. 85
5.46 Fit of experimental XANES data to Pu(IV), Pu(V), and Pu(VI) standard XANES spectra for dried ferrihydrite at pH 7.77 after exposure to light (after previously limiting light exposure as much as possible). 85
5.47 Fit of experimental XANES data to Pu(IV), Pu(V), and Pu(VI) standard XANES spectra for dried ferrihydrite at pH 7.88, which was exposed to light as much as possible. 86

A.1 Diagram of a Perkin Elmer Elan DRC II instrument. From Armstrong (2008) [5]. 108

B.1 Pyrolusite solubility in parts per million as a function of pH in 0.1 M $NaClO_4$. 112
B.2 Cryptomelane solubility in parts per million as a function of pH in 0.1 M $NaClO_4$. 113

D.1 Results of pretreatments for Nanosep filters measured on the same day as sample preparation, represented as the percent of the total Pu lost as a function of pH and pretreatment. Positive values indicate that Pu was lost during filtration; negative values indicate that the sample became more concentrated with filtration. 124
D.2 Results of pretreatments for Nanosep filters measured one week after sample preparation, represented as the percent of the total Pu lost as a function of pH and pretreatment. Positive values indicate that Pu was lost during filtration; negative values indicate that the sample became more concentrated with filtration. 124
D.3 Results of pretreatments for Vivacon filters measured on the same day as sample preparation, represented as the percent of the total Pu lost as a function of pH and pretreatment. Positive values indicate that Pu was lost during filtration; negative values indicate that the sample became more concentrated with filtration. 125
D.4 Results of pretreatments for Vivacon filters measured one week after sample preparation, represented as the percent of the total Pu lost as a function of pH and pretreatment. Positive values indicate that Pu was lost during filtration; negative values indicate that the sample became more concentrated with filtration. 125
D.5 Results of direct filtering for Nanosep filters, represented as the percent of the total Pu lost as a function of pH. Positive values indicate that Pu was lost during filtration; negative values indicate that the sample became more concentrated with filtration. 126
D.6 Results of direct filtering for Nanosep filters, represented as the percent of the total Pu lost as a function of the concentration in CPM of Pu. Positive values indicate that Pu was lost during filtration; negative values indicate that the sample became more concentrated with filtration. 127
D.7 Results of direct filtering for Vivacon filters, represented as the percent of the total Pu lost as a function of pH. Positive values indicate that Pu was lost during filtration; negative values indicate that the sample became more concentrated with filtration. 127
D.8 Results of direct filtering for Vivacon filters, represented as the percent of the total Pu lost as a function of the concentration in CPM of Pu. Positive values indicate that Pu was lost during filtration; negative values indicate that the sample became more concentrated with filtration. 128

List of Tables

2.1 Molar absorptivities for selected strong peaks of each plutonium oxidation state. From Cleveland (1979) [21]. 9

4.1 Percent substitution of Mn-substituted goethite as measured by ICP-MS, XPS, and EDS. When more than one measurement was made, the standard deviation is in parentheses for XPS and EDS. The error in parentheses for ICP-MS represents 1 σ. All measurements are for the 63-212 μm size fraction unless otherwise noted. A * next to an EDS measurement indicates that no peak was visible. 26

5.1 Experimental parameters relating to the calcining temperature necessary for successful mesoporous ferrihydrite synthesis. 36
5.2 Atomic percent ratios and standard deviations of Fe, O, and Si in ferrihydrite batches as measured by SEM-EDAX. For all reported numbers the standard deviation is in parentheses following the value. The standard deviations of secondary elements are not reported, and Al, C, and Cu were not reported as they were from the measurement substrate. 38
5.3 Surface area values for ferrihydrite batches using nitrogen adsorption data using the BET method. 49
5.4 Powder addition point of zero charge data for dried nanoparticulate ferrihydrite. Error from the best fit line is listed in parentheses. A * in the "Estimated Equilibrium PZC" column indicates poor or non-existent equilibrium. 58
5.5 Percent of plutonium bound to the solid. Initial loading was 99 $\pm$ 10 μM Pu(VI) on 8 mg of dried and suspended ferrihydrite and 13 mg of mesoporous ferrihydrite in 8 mL. pH_{24h} and pH_{120h} refer to the measured pH at 24 and 120 hours, respectively. 79
5.6 Amount of plutonium bound to the solid in milligrams of Pu per gram of solid. pH_{24h} and pH_{120h} refer to the measured pH at 24 and 120 hours, respectively. 79
5.7 Amount of plutonium bound to the solid before and after treatment with acid to remove the plutonium. All Pu(VI) concentrations are listed in micromoles. 81
5.8 Percentage of Pu(IV), Pu(V), and Pu(VI) determined from least-squares fitting of Pu L_{III} data. The "Dark" and "Light" labels indicate if the sample was exposed to laboratory lights or not. The mg of Pu(IV) is calculated based on the percent shown here and the amount of Pu bound to the surface. . . . 84

C.1 Summary of average element content of 12 plastics and borosilicate glass. From Moody and Lindstrom 1977. [97] 115
C.2 Background levels of Fe, Mn, and Al in 15 mL Falcon polypropylene vials as measured by ICP-MS for vials leached with 10 % HCl. Note that concentrations are in ppt. 116

Acknowledgments

Just as completing a full graduate career with no help from anyone else is a ridiculous idea, I never would have achieved this thesis at all without first making it to graduate school. So, I would like to begin by thanking the people who helped me arrive in Berkeley. Mom and Dad, thank you for letting me be the overachiever that I have always been, and encouraging me to push forward no matter what. Dad, I miss you dearly, but I hope somehow that you'll be able to read this thesis and understand the science you've never seen before as you always somehow manage to do. Mom, thank you for taking care of me through all the frantic phone calls when everything in grad school fell apart. Finally, Merlin, I hope you're not too mad at the fact that you'll now have to call me "Doctor."

I would also like to thank the person who helped me most to complete this journey with my mind and emotions intact. Lee, you've always been there to help me solve my problems when I was stuck and thinking about them in all the wrong ways. Thank you for bringing me up when I've been down, but still making sure that I don't get too full of myself. Thank you for supporting me in every way that you can, and for keeping me both happier and more sane than I would be otherwise.

But of course this thesis would be nothing without the other graduate students of the Nitsche group. For the foundation of my laboratory skills, I need to thank Joey Hu. By somehow convincing me to do a large portion of your labwork because I "needed to learn how to do this," you may have slowed my progress toward an individual project, but you greatly increased my ability to do experiments in lab and to find the answers I need on my own. I am now an expert on finding references for obscure concepts and balancing the pH of mineral solutions. I am, however, conflicted on whether to thank you for the perpetual night shifts at beamlines 11-2 and 2-3, despite the fact that they "build character."

For comradery in the "valley of tears" known to both of us as organically modified silica, I would like to thank Tashi Parsons-Moss. I'm very glad that we've both managed to make it out of the valley, although it appears we may have sent Eva down there in our stead (sorry Eva). Thank you for your friendship and patience this last five years, and best of luck on your thesis. You will certainly get the distinction of completing the largest number of experiments of anyone in our group.

Deborah, Deborah, Deborah: thank you for making my grad school career better, and "fool" of laughter, noms, and good rants. Thank you as well for getting through all of my XAS data, and in what I'm sure is record time, assuming that there's a record for that. I know for sure that I still owe you some early mornings in lab, but if you'll forgive those, then I'll forgive the crunches.

Oliver, thank you for feeding me delicious food, keeping me on my toes as a GSI, and making me feel like my light-induced chemistry was a benefit to science in general. Oh, and dynamic cross ball (now it's in here too). Jen and Erin, thank you for all of the fun afternoons in 70 when none of us felt like doing work. You've both been a joy to have in the group, and I will definitely miss the delicious cupcakes. And Erin, thank you for all of the edits on this thesis; I'm positive that it reads more cleanly because of your careful eye. Nick, thank you for the hugs and encouragement, and for adding to our numbers at House of Curries when it started to look like I had no friends. And to Eva and Philip–you're both great additions to our group, and it is too bad that I was only to overlap with you by a year.

My experience was also improved significantly by the staff at LBNL. To Wayne and John van Wart, thank you for being always helpful and ever reasonable for every question and situation. Corwin, thank you for all of the patient hours at the beamline, driving our samples down to Stanford, and showing me that good science can still actually be somewhat close to a 9-to-5 job. And to Joern, thank you, thank you, thank you for your assistance, patience, and advice. Dear Elan would have been quite a bear to work with without your help, and our discussions formed the foundation of much of my analytical chemistry mentality. Also thanks to you I can now troubleshoot just about every problem that a high-sensitivity balance can have.

Another important contribution to my work came from a simple comment from Brian Powell at Pacifichem 2010. Brian, thank you for cluing me in to the possibility of light-induced reduction and saving me from however much time it would have taken me to come to that realization on my own. I would also like to thank Harun Tüysüz for providing me with my mesoporous ferrihydrite.

And now that I have already said so many thank you's, there is one more without which this thesis would not be complete. Heino, thank you so much for the last five years. I'm very glad that I finally decided to join your group, as the chemistry has been interesting and company has been great. Thank you for being a flexible and understanding boss, and for caring about your students as people rather than data factories. Thank you for providing suggestions when I needed them, and for letting me pursue the ferrihydrite chemistry as I saw fit. I think I've turned into a full-blown scientist, and you've been instrumental in getting me there.

Chapter 1

Introduction

Iron oxides are ubiquitous in the environment [26], and understanding their chemistry is paramount for increasing our knowledge of environmental systems and contaminant transport. Goethite, hematite, and ferrihydrite are three of the most common iron oxides [65, 161], but have been studied in unequal amounts, particularly with respect to certain contaminants. Hematite is one of the most stable iron oxides and the end of the transformations of other iron oxides [26], and has thus been studied in relative abundance in both the bulk [6, 7, 26, 58, 59, 81, 132] and nanoscale [121, 169, 173, 181]. Goethite is also quite common, and has also been frequently studied [26, 37, 45, 51, 96, 99, 125, 131, 136, 169], but usually only in its pure form. Because goethite in nature also exists in a form that will have minor substitutions of other elements [26], studying those minor substitutions brings us one step closer to understanding the natural world. Ferrihydrite is one of the least stable, most variable forms of iron oxide. Although it has been only intermittently studied, ferrihydrite is one of the most important iron oxides for contaminant transport, as it forms readily in lakes, rivers, and waterways as a colloidal species. It is also important due to its transformation to both goethite and hematite. With high surface reactivity, ferrihydrite is often a primary sorbent for heavy metals, actinides, and other contaminants and can therefore also be a vector for contaminant transport. [39, 65, 79] A fuller understanding of ferrihydrite chemistry is crucial for understanding its role in the environment.

There are many environmental contaminants of interest, arising from mining, factories, agriculture, and hundreds of other processes and industries. Of interest in the current age, when the need for cleaner energies is urgent and the use of nuclear power is on the rise, are radionuclides. The study of radionuclides in environmental conditions is increasing, but has not yet seen the advances of other fields. There are many recent studies on the interactions of uranium with iron oxide minerals [6, 7, 37, 45, 51, 58, 59, 81, 96, 99, 131, 132, 136, 145, 181], but many fewer with plutonium [57, 62, 87, 115, 121, 125]. While the chemistry of the two elements is often close and certainly related, it is nonetheless worthwhile to study plutonium interactions independently. Plutonium is a significant product of the nuclear fuel cycle, and will be present in any waste from that industry.

In addition to environmental transport, the proliferation of elements, such as uranium and plutonium, that can be used for weapons is also of current concern. It is therefore crucial to ensure the defense of our borders against the theft and transport of actinides. To enact this protection, methods must be discovered to selectively sense the actinides chemically,

because detecting them by their alpha particle radiation is too easy to prevent and too difficult to employ. There are several steps along the way before selective sensing can be achieved: first the ability to bind the actinides in high quantity, then the ability to separate them from other analytes and, ideally, from each other. An understanding must be gained of what sort of materials will and will not achieve this sequestration and separation. Only then can the development of a sensing apparatus begin, once the behavior of the actinide ions and complexes is more fully understood.

This work is the joining of these two separate aims. The initial impetus was a continuation of the work of Richard Wilson [176], who studied plutonium sorption on pure goethite, and Dawn Shaughnessy [129], who studied plutonium sorption on manganese oxides. This led to joint work with Yung-Jin Hu [62, 61] on the role of minor manganese substitutions into the goethite structure. Goethite had shown no ability to reduce Pu(VI) to Pu(IV), whereas the manganese oxides had. The goal of the Mn-substituted goethite was not only to characterize the model mineral, but also to determine its capacity for causing plutonium reduction. It was shown that even small substitutions of manganese were sufficient to cause reduction. The portion of this joint effort presented here focuses on the characterization of the mineral apart from its interactions with plutonium. The portion of the work relating to the plutonium sorption and binding characterization can be found in Hu *et al.* (2010) and Hu (2011) [62, 61].

The next step was to expand to another iron oxide, ferrihydrite, using knowledge of iron oxide behavior gained from the Mn-substituted goethite, but hoping to do research useful to two different fields. As mentioned above, ferrihydrite is a common iron oxide phase and important to understanding contaminant transport [65]. It has a large surface area and high surface reactivity, which make it important for environmental contaminant modeling, but also make it attractive for applications that require this high reactivity. Ferrihydrite is already used as an industrial sorbent and catalyst [41, 65, 182], but the material is not highly understood yet. This makes ferrihydrite a prime candidate for successful actinide sorption, and a full understanding of its surface properties may lead to the ability to selectively sequester actinides. It is also relatively inexpensive to produce [16], making it even more attractive for a possible scale-up to an industrial process. Plutonium has been studied on other iron oxides [57, 62, 87, 115, 121, 125] and on mixed element natural hydrous ferric oxides [69], but never before on pure ferrihydrite (to the knowledge of the author).

However, the practical application of ferrihydrite to many processes is difficult. Nanoparticulate suspensions are not simple to handle in a process, as they cannot easily be filtered nor do they tend to be as stable as a dried version in the case of ferrihydrite. However, even dried nanoparticulate ferrihydrite is not particularly stable with respect to aging [39, 126], and while the synthesis is fairly simple and straightforward, the grinding process necessary for its overall production is both time consuming and tedious (Section 5.3.1). The surface, pore size distribution, and particle size can be highly variable, making reproducibility a matter of question. Therefore, the synthesis of a material that has many of the surface reactivity characteristics of ferrihydrite, but a more ordered structure and a particle structure that is more readily dealt with seemed to be highly advantageous. This notion led to the idea of using an ordered mesoporous ferrihydrite.

It was with these ideas in mind that your intrepid author embarked on the work that makes up the largest portion of this thesis. Three ferrihydrite materials–a never dried suspension, the same suspension when dried and ground, and a nanocast ordered mesoporous

powder–were synthesized and compared with respect to their structure, surface chemistry, and interactions with plutonium(VI). While most authors who have studied ferrihydrite (often referred to as hydrous ferric oxide) have investigated the dried solid, the use of the suspension is relatively uncharted, despite it being the more common form of the mineral in nature. Thus, the comparison of these two materials will aid in identifying which aspects of previous work apply to both materials, and which are properties of one alone. There was also particular care taken in identifying and maintaining the form of ferrihydrite as the less crystalline 2-line and not the more crystalline 6-line, as this distinction is often muddled or not stated in ferrihydrite studies. However, the truly new material is the ordered mesoporous ferrihydrite, first reported by H. Tüysüz in 2008 [164]. There are several previous syntheses of mesoporous ferrihydrites [82, 91, 139, 177], but none have exhibited a regular, ordered network of pores as this synthesis does.

This is by no means a complete study of ferrihydrite structure, surface chemistry, or interactions with plutonium. It is, however, a significant step toward understanding how 2-line ferrihydrite behaves under the conditions tested and the ensuing potential use of ferrihydrite for actinide remediation or detection.

Chapter 2

Plutonium Chemistry

2.1 Introduction

The primary analyte isotope for this research was plutonium-239. Plutonium is a highly redox active element, and can exist as four different oxidation states simultaneously in solution: Pu(III), Pu(IV), Pu(V)O_2^+, and Pu(VI)O_2^{2+}. Pu(VII) is also possible, but is much more difficult to form and is not found under environmental conditions. In noncomplexing acidic conditions, such as perchloric acid, Pu(III) and Pu(IV) exist as simple hydrated cations, but Pu(V) and Pu(VI) exist as the plutonyl moieties, with two axial oxygens bound to the central plutonium atom and effective charges of 2.3 and 3.3, respectively. [21, 123] Plutonium(VI) is shown in Figure 2.1. In general, the more oxidized forms are more soluble than the more reduced forms (see Figure 2.3), particularly at higher pH [18, 20, 21]. This also makes the oxidized plutonyl forms more mobile in aqueous environmental systems, although colloidal transport of the reduced forms is also possible. Pu(IV), (V), and (VI) are found in oxic waters, and are therefore highly relevant to environmental studies and the understanding of mineral interactions. For this reason, as well as for the ease of use due to the higher solubility and stability under a wide range of pH conditions, Pu(VI) was chosen as the oxidation state of interest.

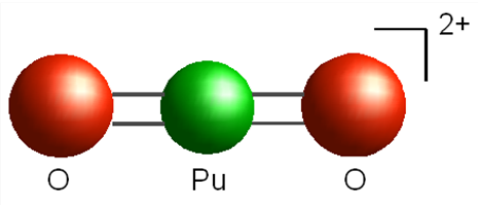


Figure 2.1: Plutonium(VI) exists as the 2+ plutonyl cation.

2.2 Solution Chemistry

Understanding how plutonium, and plutonium(VI) in particular for this work, behaves in solution is paramount for understanding how it will react with a mineral at the solid/solution

interface. The following sections establish some basic behavior to further define the systems involved in Chapter 5.

2.2.1 Plutonium Redox Chemistry

Due to the small redox potential difference between oxidation states of around 1.0 V (in 1 M $HClO_4$; they are lower for higher pH conditions) [17, 20], Pu can easily change oxidation state in solution. This is particularly true for the plutonyl Pu(VI)-Pu(V) pair and the bare cationic Pu(IV)-Pu(III) pair because no loss or gain of oxygen atoms is necessary. The similar redox couples also allow multiple oxidation states to co-exist in solution, greatly complicating the chemistry of plutonium. The common disproportionation reactions are shown by the following equations [21], which depend on which Pu species are present in solution. For the disproportionation of Pu(IV), the reactions are:

$$2Pu^{4+} + 2H_2O \rightleftharpoons Pu^{3+} + PuO_2^+ + 4H^+ \tag{2.1}$$

$$Pu^{4+} + PuO_2^+ \rightleftharpoons Pu^{3+} + PuO_2^{2+} \tag{2.2}$$

And for the disproportionation of Pu(V) in the presence of Pu(III), the reactions are:

$$PuO_2^+ + Pu^{3+} + 4H^+ \rightleftharpoons 2Pu^{4+} + 2H_2O \tag{2.3}$$

$$PuO_2^+ + Pu^{4+} \rightleftharpoons Pu^{3+} + PuO_2^{2+} \tag{2.4}$$

For the disproportionation of Pu(V) if only Pu(V) is present, the reaction is:

$$2PuO_2^+ + 4H^+ \rightleftharpoons Pu^{4+} + PuO_2^{2+} + 2H_2O \tag{2.5}$$

In all cases, if the reaction involves the making or breaking of Pu-oxygen bonds it will be much slower than if the reaction only involves electron transfer. These reactions are not the only redox reactions that can occur in solution, but they are important for understanding the solution oxidation state distribution.

A Pourbaix diagram can also be constructed to display which oxidation state and species are stable under various Eh and pH conditions. Figure 2.2 shows the rough stability regions of the four Pu oxidation states commonly found in aqueous solution. This calculations to produce diagram included the complexes formed from both plutonium hydrolysis and exposure to atmospheric carbonate.

2.2.2 Plutonium Solubility and Speciation

When metal ions are in aqueous solution they can undergo pH dependent hydrolysis reactions, such as:

$$M^{+n} + mH_2O = M(OH)_m^{+(n-m)} + mH^+ \tag{2.6}$$

Mononuclear hydrolysis products form first, but these will eventually form oligomers and polymers. For plutonium, the pH at which hydrolysis begins is dependent on the oxidation

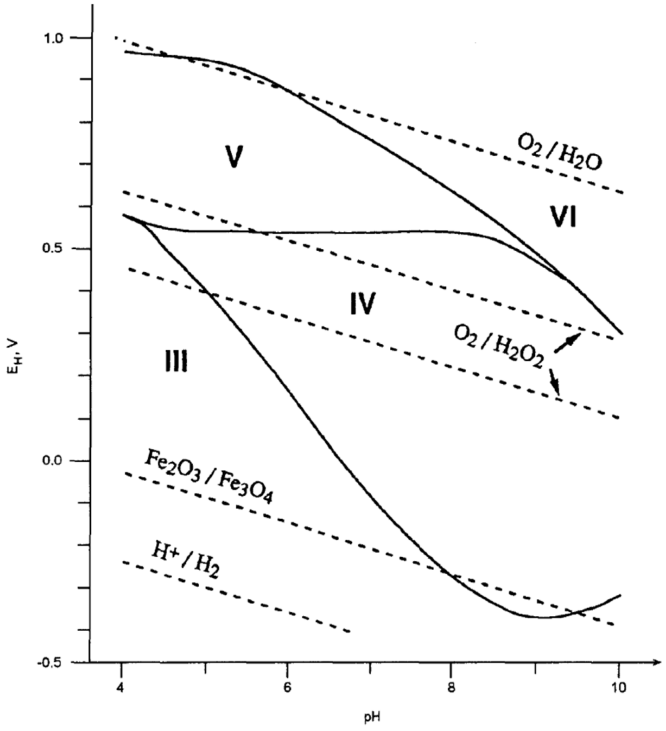


Figure 2.2: Pourbaix diagram for plutonium in equilibrium with atmosphere. From Choppin *et al.* (1997) [18].

state, with Pu(IV) requiring the lowest pH, followed by Pu(VI), then Pu(III), and finally Pu(V) requiring the highest pH. This is also depicted in Figure 2.3. [19]

The speciation of Pu(VI) is highly important for discussions of aqueous solutions at variable pH conditions and sorption to surfaces under these conditions. In general, Pu(VI) forms the positively charged plutonyl at low pH (see Figure 2.4), positive and neutral hydrolysis products in the neutral pH range, and then neutral to negatively charged carbonate complexes at higher pH when exposed to air. While the error associated with determining these species is quite significant, the speciation diagram presented in Figure 2.4 gives a good understanding of which species are likely to be present in solution at various pH conditions. It should be noted that this speciation may change depending on solution conditions, plutonium oxidation state distribution, and which, if any, solid is present in solution. For example, examination of a more detailed Pourbaix diagram for Pu in the presence of hydroxide, carbonate, and fluoride (Figure 2.5 gives the speciation as a function of both Eh and pH.

Carbonate complexes form in a similar manner when Pu solutions are exposed to air. They only form at higher pH because the carbonate anion is only present in solution above approximately pH 6. Thus, the Pu carbonate complexes do not begin to form until around pH 6, as shown in Figure 2.4. The formation of carbonate complexes does increase the solubility of Pu(VI) in basic conditions.

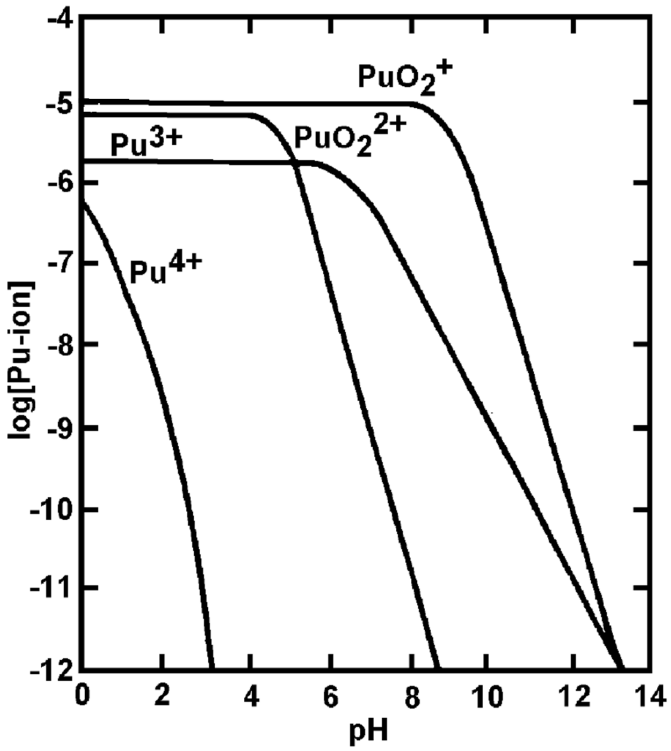


Figure 2.3: Plutonium solubility (non-hydrolyzed ions) as a function of pH as calculated by Choppin *et al.* (2002) [19].

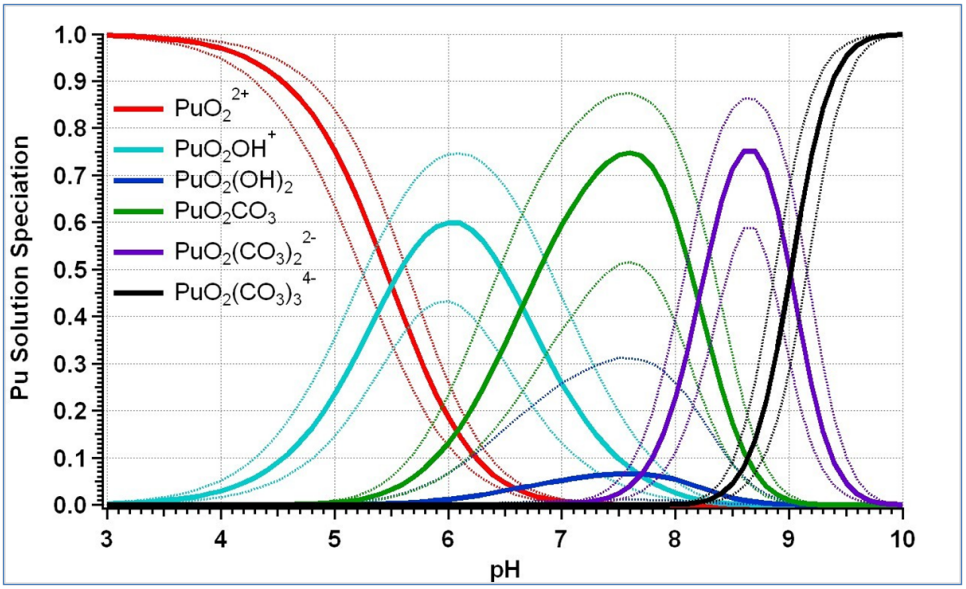


Figure 2.4: Speciation diagram for Pu(VI) exposed to atmospheric carbonate. Solid lines represent the calculated data and dotted lines represent the asymmetric error bars to 1 σ. From Hu *et al.* (2010) and Hu (2011) [62, 61].

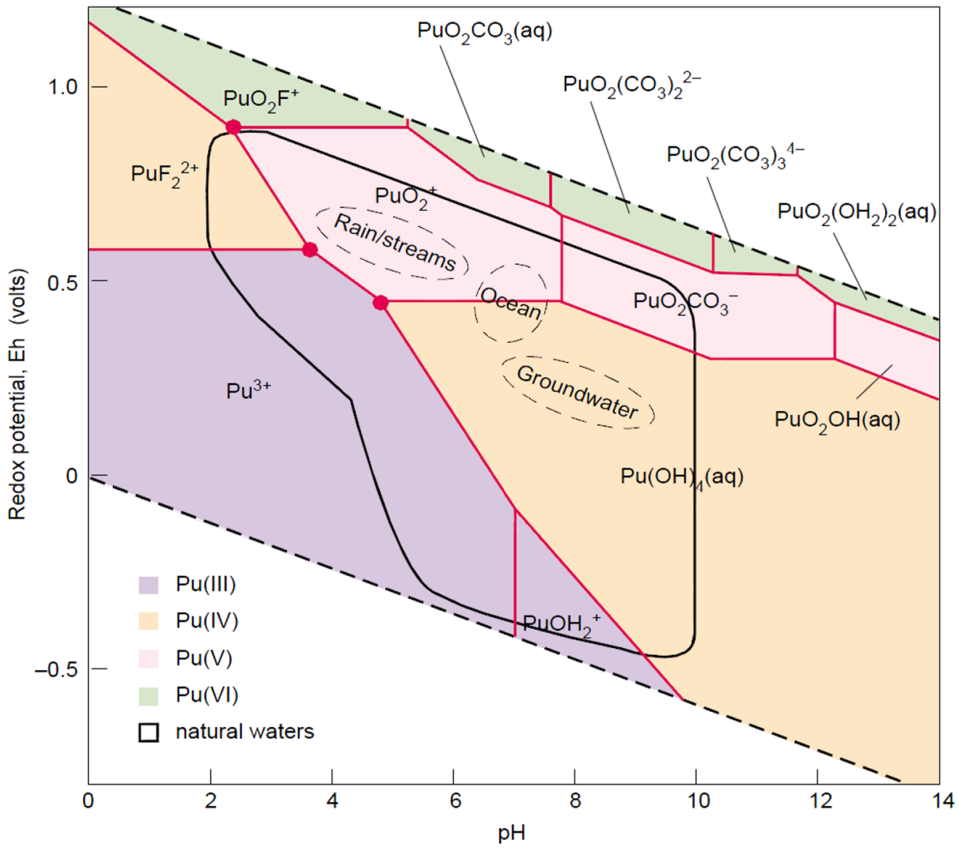


Figure 2.5: Pourbaix diagram for plutonium in an aqueous solution containing hydroxide, carbonate, and fluoride. The Eh/pH conditions found in natural waters are also outlined. From Runde (2000) [123].

Oxidation State	Peak Wavelength	Extinction Coefficient
Pu(VI)	830.3	550
Pu(V)	569	17.1
Pu(IV)	470	49.6
Pu(III)	600	35.3

Table 2.1: Molar absorptivities for selected strong peaks of each plutonium oxidation state. From Cleveland (1979) [21].

2.3 Preparation of Plutonium Solutions

All solutions of plutonium in these experiments were prepared as Pu(VI). To accomplish this, plutonium oxide was first dissolved in nitric acid, then processed through an anion exchange column to separate the Pu from other contaminants such as iron, uranium, and its daughter americium. A description of this column can be found in Hu (2011) [61]. The solution was then boiled initially with concentrated nitric acid to digest any organics, and then with concentrated perchloric acid to ensure that it was completely oxidized to Pu(VI). *Caution: The presence of any organic material, even the smallest amounts, may cause an explosion when placed in contact with hot perchloric acid.* Smaller secondary stocks were prepared from the main stock and diluted with 1 M $HClO_4$. UV-visible spectra were collected on each new stock to verify that it was Pu(VI) and did not contain significant percentages of the lower oxidation states. A representative UV-visible spectrum is shown in Figure 2.6. Unfortunately, the extinction coefficients of the lower oxidation states are significantly less than for Pu(VI) (see Table 2.1), so small percentages of the other oxidation states are below the detection capabilities of the UV-visible system used, which was an Ocean Optics USB2000 fiber optic spectrometer measuring from 400-1000 nm.

2.4 Alpha Particle-Induced Chemistry

Plutonium decays primarily by alpha decay. The isotope used in these investigations, ^{239}Pu, has a half-life of 24,110 years [163] and emits alpha particles with an average energy of 5.15 MeV [117]. In aqueous solution, this energy (approximately 0.4 eV per day per atom of plutonium [21]) is deposited into water, ionizing it and releasing an electron. This electron can then further ionize surrounding water, creating a track of radiolysis products, which can include H_2, H_2O_2, and H and OH radicals [140]. Other radiolysis products can also be produced from any other surrounding molecules. These radiolysis products can interact with plutonium ions to cause redox chemistry to occur; in general, reduction of more oxidized forms to more reduced forms is the most common, but oxidation of reduced forms also occurs. Examples of some of these reactions are [13]:

$$\mathrm{Pu(III)} \xrightarrow{\mathrm{OH,H,HO_2}} \mathrm{Pu(IV)} \xrightarrow{\mathrm{OH}} \mathrm{Pu(V)} \underset{\mathrm{e_{aq}^-,H,HO_2}}{\overset{\mathrm{OH}}{\rightleftharpoons}} \mathrm{Pu(VI)} \tag{2.7}$$

This means that solutions prepared as Pu(VI) will slowly undergo reduction to Pu(V) and

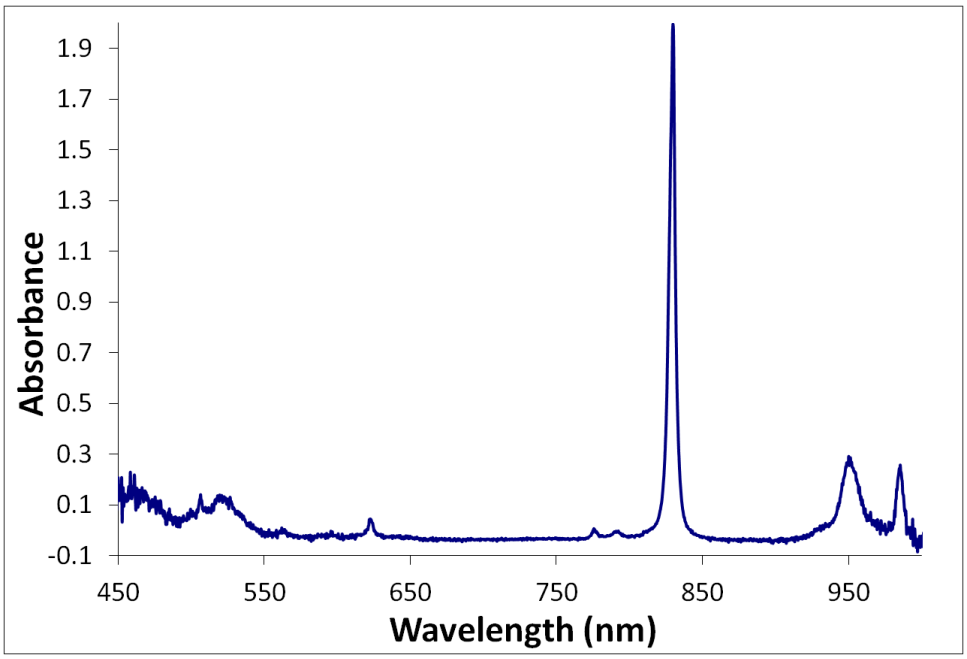


Figure 2.6: Representative UV-visible spectrum of plutonium stocks used for experiments, which shows only Pu(VI) peaks.

then to Pu(IV), a phenomenon known as alpha particle-induced reduction, or autoreduction. [12, 21, 105] This reduction can be described by an overall change in the oxidation number. The oxidation number is a representation of the distribution of oxidation states in a solution and is described by [117]:

$$\bar{ox} = \frac{([\text{Pu(III)}] + [\text{Pu(IV)}] + [\text{Pu(V)}] + [\text{Pu(VI)}])}{[\text{PuTotal}]} \tag{2.8}$$

Autoreduction causes a change in oxidation number of -0.013 to -0.018 per day [21, 104, 117]. Unfortunately, this representation of autoreduction does not directly indicate the percentages of each oxidation state, so it is only moderately useful in predicting the oxidation state composition of an aged solution. However, it is a good indication of the overall rate at which reduction occurs, which is generally rather slow. Plutonium will also reduce much more readily to Pu(V) than it will to Pu(IV) or Pu(III) [21] at a rate of about 1.5 % per day [105], so it can generally be assumed that in the early stages of autoreduction for a solution, the amount of Pu(V) will exceed the amount of Pu(IV) by a significant amount. Rough calculations show that the percentage of Pu(IV) in a solution can be estimated to be less than 5 % after one week, so it likely does not play a significant role in many experiments until the concentration of Pu(IV) is greater than 10 % at approximately the two week mark (see Figure 2.7). Note however that these are approximations based on previously reported oxidation number changes, and the Pu oxidation state changes were not actually monitored. Additionally, the reduction rate is lowered to almost zero when the solution is in concentrated perchloric acid due to the oxidizing capabilities of $HClO_4$. Because the primary plutonium stock was always held in concentrated $HClO_4$, autoreduction was not nearly as large of a

factor for the primary stock as it was for the secondary stocks and samples, and it was only necessary to reboil the primary stocks every several months.

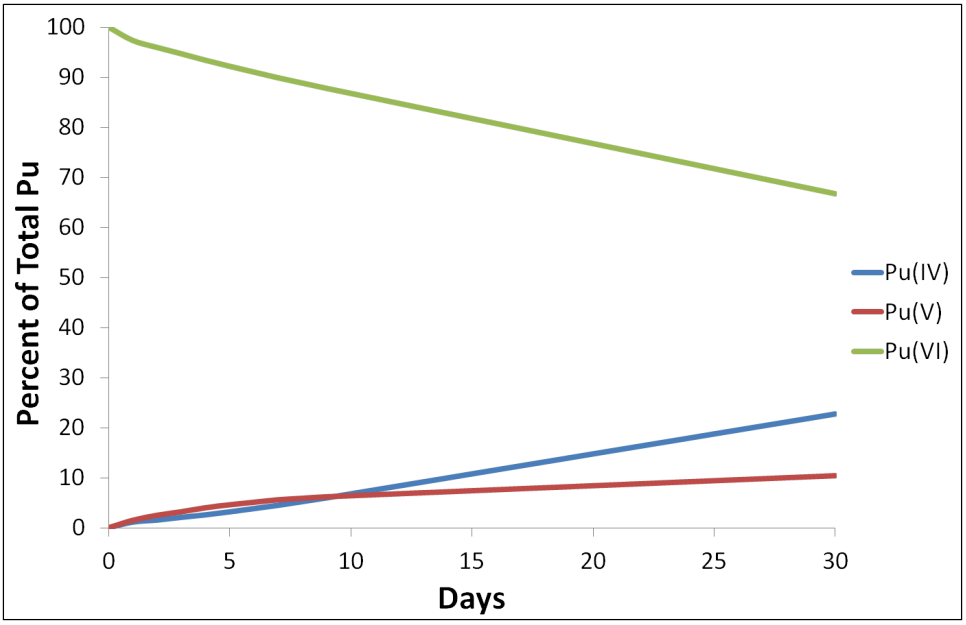


Figure 2.7: Approximate percentages of Pu(IV), Pu(V), and Pu(VI) in solution over time as a result of autoreduction.

2.5 Plutonium Measurement with Liquid Scintillation Counting

All plutonium samples measured in the course of this work were measured using liquid scintillation counting. A brief description of the technique and the instrument is therefore relevant to the discussion of this work.

Liquid scintillation counting (LSC) is a technique that allows for the measurement of the concentration of radioactive elements that decay by beta or alpha emission. While it is possible to measure both alpha and beta decay using other kinds of detectors, LSC offers many advantages. The primary advantage is that because the distance an alpha or beta particle will travel in solution is very short (on the order of millimeters), surrounding the emitter with the scintillant prevents loss and allows for 100 % efficiency for alpha particles. The samples also do not need to be dried to a plate for measurement, high salt content samples are still measurable, and analysis is rapid, with a 300 second count being standard for most samples with counts of at least ten times the background levels.

For measurement with LSC, samples (solid or liquid) are mixed with a scintillation cocktail in a transparent or translucent vial. While the exact contents of scintillation cocktails are proprietary, they all contain the same types of molecules: solvent phosphors (scintillators), and sometimes wavelength shifters (secondary scintillators). The solvent is needed to absorb the energy of the emitted particle, and then pass that energy to the phosphors. Aromatic

solvents, such as toluene, are typical solvents, although most scintillation cocktails now use much less toxic aromatic solvents. The conjugation of the aromatic rings provides good absorption of the particle energy, which is then usually passed between solvent molecules until it is passed to a phosphor. This continual passing of energy allows for high efficiency because it is highly likely that the energy will be passed to a phosphor before it is lost. The scintillators convert the captured energy to light. Often this light has a wavelength of around 400 nm or less where photomultiplier tubes (PMTs) responses are lower, so secondary scintillators are often present to absorb the fluorescence of the primary scintillators and re-emit it at a longer wavelength to better be measured by the PMT. [102]

All scintillators will emit a single photon of a wavelength of light characteristic of that scintillator. However, the energy of an alpha or beta particle will excite more than one solvent molecule. The mean path of the particle is small enough that it will excite solvent molecules in only a very small area, which will excite scintillators in only a very small area, and thus all excitations originating from that alpha or beta particle will be measured with sufficient simultaneity to be read as one pulse of light. This pulse will have a number of photons proportional to the path length of the emitted particle, which is in turn proportional to the energy of that particle. By a short step of logic, the response of the PMT can be related to the energy of the original radiation. Therefore, LSC does produce both a count rate (number of light pulses per unit time) and an easily calibrated spectrum (number of photons in each of those pulses, which relates to energy). LSC instruments can be programmed to report only the counts falling in a certain range of channels or bins so that the decay from a particular element can be separated from the decay of other elements given that those elements' decays are of sufficiently different energies (a beta and an alpha emitter, for example). [102]

The efficiency of this measurement depends on how well the emitted energy is converted to light, a value that changes with the cocktail, the sample solution, and the type and energy of radiation. The lowest efficiency is for low-energy beta particles, where a maximum efficiency in the single digits is to be expected. However, for the much higher energy alpha particles, the efficiency is generally considered to be 100 %. Althought the PMT will not measure all of the photons produced, the energy of the alpha particle is sufficient to create enough photons that the signal will not be lost (as can be the case for low energy betas). It is possible to lower the efficiency if molecules in the solution absorb the energy of the radiation before it is converted to light or the light before it reaches the PMT. This is known as chemical and color quenching, respectively. The reduced number of photons measured at the PMT also lead to a shift in the spectrum. Quenching can be corrected for by using an internal or external standard, or by using the amount the spectrum shifts. [102]

The samples measured for this work were all Pu-239, which emits a 5.15 MeV alpha particle [21]. Due to the high particle energy and the lack of quenchers in solution, the efficiency is considered to be 100 % in all cases. This means that the counts per minute measured by the LSC are equal to the decays per minute of the plutonium and can be easily converted to a plutonium concentration using the half life. All samples were counted for 300 seconds after being shaken for at least 60 seconds to evenly disperse the analyte solution in the cocktail. A blank LSC vial with no activity added, but passed through the same glovebox procedure, was counted with each sample set to determine a background rate to be subtracted. Almost all samples contained an activity of at least ten times this background level. Additionally, it should be noted that samples containing solids were filtered so that

assaying by LSC always measured the amount of plutonium remaining in solution. The amount on the solid is therefore only measured by subtracting the amount of plutonium left in solution from the amount originally added to the solution. This obviously does not differentiate between sorption to the solid and precipitation from solution as both processes would remove plutonium from solution and therefore decrease the amount measured by LSC. To differentiate between sorption and precipitation a technique such as X-ray absorption spectroscopy to determine nearest neighbors is necessary (see Section 5.9.6).

Chapter 3

Surface Chemistry

3.1 Introduction

There is nothing more important in the study of interfacial phenomena than the chemistry that occurs at the surface. This includes both the properties of that surface and the nature of its interactions with species in solution. Therefore, to understand how the plutonium will interact with the mineral surface, the mineral surface must first be understood. The following chapter describes some key definitions and descriptions of relevant chemical properties and techniques for understanding the mineral surface. The common thread that ties these concepts together is the charge. Much of what determines pH dependent sorption behavior and surface complexation is the surface charge of the mineral as it relates to the plutonium speciation (covered in Chapter 2). Surface charge can be understood by the measurement of a point of zero charge, described below. Charge transfer is responsible for the plutonium redox chemistry that can occur upon binding, and is therefore also important enough to warrant an extended discussion.

3.2 Surface Complexation and Point of Zero Charge

Adsorption occurs when a reaction occurs between a chemical substance and a phase boundary. Adsorption can be positive or negative depending on whether there is addition to or depletion of the substance. In the case of a solid-liquid interface, the solid is the absorbent and the species that accumulate on the surface are the adsorbate (although when they are still in solution they are considered the adsorptive). When a surface functional group (adsorbent) reacts with a molecule or ion dissolved in solution (adsorptive) to form a stable complex (adsorbate) this is called surface complexation. There are two kinds of surface complexation: inner-sphere (specific adsorption) and outer-sphere (non-specific adsorption). Inner-sphere complexation occurs when the bound species is bound directly to the surface and there is no water between the complexed species and the surface functional group. If there is at least one water molecule between the surface and the bound species, then the complex is considered to be outer-sphere. Generally inner-sphere complexation is stronger, as it is the result of direct ionic or covalent bonding, whereas outer-sphere complexation tends to be due to electrostatic interactions. The diffuse swarm is one step further away

from the surface and consists of solvated ions that screen a surface or balance surface charge but are not in a surface complex. [143]

Adsorption experiments in the course of this work are all performed by batch experiment, where a solid in solution is contacted with Pu(VI) and allowed to equilibrate for a set amount of time before measurement. Ideally the amount of Pu both on the surface and in solution would be measured, but as the handling of radioactive materials and the measurement of alpha particles on a surface is difficult, only the solution concentrations were measured.

It is well known that the amount of surface complexation is heavily dependent on pH, as either protons or hydroxide anions must be released from the surface for metal cation or anion binding, respectively. [147] The dependence on pH is also a function of the surface charge, as not all surfaces have the same charge characteristics at a particular pH. The net total surface charge is a function of the permanent structural charge (from isomorphic substitutions, cation vacancy defects, etc.), the net proton charge (the difference between the moles of protons and hydroxide ions complexed by the surface), the Stern layer charge (from the charge of adsorbed ions, in either inner-sphere or outer-sphere configurations, which can be split into the charges of the inner- and outer-sphere complexes), and the dissociated charge (from the diffuse swarm ions that balance the surface charges). [142, 143]

These surface charge density definitions can be used to define various points of zero charge. In the simplest terms, the point of zero charge (PZC) is the pH at which there is no net charge on the solid, meaning that the positive charges equal the negative charges, generally including the surface complexes. The point of zero net proton charge (PZNPC) is where the surface concentration of protons equals the surface concentration of hydroxide. This is usually measured by finding the intersection point of two or more potentiometric titrations performed at different ionic strengths, although this may be more accurately described as the point of zero salt effect (PZSE), where there is no change in the net proton charge with a change in ionic strength. The point of zero net charge (PZNC) is the pH where the net charge of the adsorbed ions is zero (the cation exchange capacity equals the anion exchange capacity) and the point of zero charge (PZC) is the point at which the net total charge is equal to zero and no surface charge exists to be neutralized by the diffuse swarm. The PZC can be measured by finding the pH at which a suspension flocculates, or comes out of solution, rapidly. [143]

There are cases where these different points of zero charge are equal to one another. If there is no structural charge, then the PZNC equals the PZNPC, and if the Stern layer charge is zero at the PZNC then the PZC is equal to the PZNC. Additionally, if the Stern layer charge increases (or decreases), then the PZC will also increase (or decrease). [143] If the only contributors to the surface charge are the proton and dissociated charges, then the PZNPC is equal to the isoelectric point (the pH at which the particle carries no electrical charge and does not move in an electric field), and it is termed the pristine point of zero charge. [142, 143]

The point of zero charge measured in this work is the point of zero net proton charge, which can be measured by potentiometric titration [146], mass titration [107], and powder addition [67, 100, 101]. Below this pH, the surface is positively charged, and above this pH the surface is negatively charged. For oxyhydroxide minerals, this means that below the PZC the surface oxygen groups are doubly protonated, at the PZC they are singly protonated, and above the PZC they are deprotonated. A schematic of this is shown in Figure 3.1. Note

that this protonation/deprotonation begins at a pH well away from the PZC, so the surface charge is constantly changing as a function of pH.

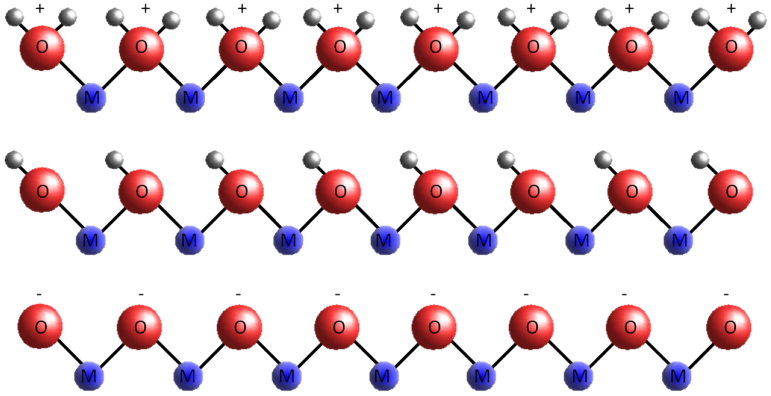


Figure 3.1: Surface charge below (top), at (center), and above (bottom) the point of zero charge.

Brief descriptions of these measurement methods are presented in Section 5.8. For a full description, the reader is referred to references provided.

3.3 Semiconductor Surface Charge Transfer

The plutonium redox chemistry described in Section 5.9.3 is only possible through a surface electron charge transfer from the ferrihydrite to the plutonium. That charge transfer has been shown to be light-induced, and in order for this to occur, the band gap of the ferrihydrite must be of an appropriate energy for the light to excite an electron-hole pair. The excited electron must then travel to the surface of the ferrihydrite particle and be transferred to a plutonium molecule. The following section is intended to provide the knowledge necessary to understand the discussion presented in Section 5.9.3 that details how the process could happen for ferrihydrite.

Ferrihydrite is an intrinsic semiconductor, like many other iron oxide minerals, meaning that an undoped sample has a band gap of less than about 5 eV [166]. The properties of semiconductors are dependent on the particle size, and the differences in properties led to particles under 100 nm to be classified as nanoparticles. Suspended nanoparticles are often referred to as colloids. Within the colloid and nanoparticle category, there are particles that have normal electronic behavior, and those that experience quantum size effects. Quantum size effects will play a role when the Bohr radius of the first exciton of the semiconductor is on the order of the particle size. This Bohr radius depends on the semiconductor material, as it is based on the material's effective mass according to the following equation [48]:

$$r_B = \frac{h^2 \epsilon_0 \epsilon}{c^2 \Pi^* m} \tag{3.1}$$

where r_B is the Bohr radius, ϵ is the dielectric constant for the semiconductor, and ${}^*m$ is the relative effective electron mass for the semiconductor. Although the dielectric constants

for poorly crystalline solids are not easily measured by experiment, Sverjensky and Fukushi (2006) [149] have estimated the value for ferrihydrite based on the surface complexation work of other authors. They calculated two different values, one for 2-line ferrihydrite (32) and one for hydrous ferric oxide (HFO) (1000). The synthesis of the HFO was similar to the synthesis employed here and was treated in $NaClO_4$, but the 2-line ferrihydrite was confirmed by XRD to be 2-line ferrihydrite, so either value could be appropriate. Iwamoto *et al.* (2000) [64] investigated the band gaps of iron oxides encapsulated in mesoporous silica to control the particle size, and found a relative effective mass of 0.27 fit the data sufficiently. Using these values and the equation above, a Bohr radius can be calculated of either 63.9 Å if 32 is used for the dielectric constant, or 1997.5 Å if 1000 is used. Therefore, it is possible that quantum size effects may play a role for the smallest particles of the dried and mesoporous ferrihydrite, and it is almost certain that they play a role for the suspended ferrihydrite (see Section 5.5.

The result of quantum size effects is the widening of the band gap of the material [48, 64]. For confined iron oxides, for example, an increase from 2.14 eV for bulk Fe_2O_3 to 4.2 eV for Fe_2O_3 confined to a 2.13 nm pore was measured [64]. The band gap of 2-line ferrihydrite has only been measured (to the author's knowledge) once by Liu *et al.* (2006) in the form of ferritin to be around 1.5 eV for 3 nm particles and 2.7 eV for 6 nm particles [86]. Although the smaller particle would be expected to have a smaller band gap, there may have been other particle characteristics that caused this difference such as different levels of crystallinity or different interactions with the surrounding ferritin. The band gap of dried and mesoporous ferrihydrite would be expected to be similar, based on the fact that other related but more crystalline iron oxides have band gaps of 1.94-2.10 [80] and 2.3-2.5 eV [130]. Quantum size effects would suggest though that the band gap of suspended ferrihydrite is on the order of 4 eV based on the work of Iwamoto *et al.* and the measured particle sizes. The importance of this difference will become apparent in the discussion in Section 5.9.3.

Lattice defects will also have an effect on the electronic conduction of a semiconductor particle. [48] Oxygen vacancies are common in semiconductor metal oxides, and may be the most prevalent defect at the surface. [109] A missing oxygen from the structure of an ionic oxide, such as a transition metal oxide, results in the trapping of two electrons in the location where the O^{2-} anion would be or the transfer of those electrons to empty d orbitals of the metal [109]. When this vacancy is filled by half of an O_2 molecule, the now filled vacancy acts as an electron donor and n-type conductor [48]. Surface oxygens can also act as donor sites because they retain electron density even while the surface is neutral. They also experience a lower than normal electrostatic attraction from a fewer number of neighboring metal cations than their counterparts in the bulk of the sample [166]. Interstitial metal defects are also donors, making a semiconductor with this type of defect an n-type semiconductor. [48] These are just a few examples of how some common lattice defects will affect the conduction type of the material; it is by no means an exhaustive list, but demonstrates important examples.

Specific defects in semiconductors can also enhance electron-hole recombination by creating energy levels within the band gap, thereby reducing the number of charge carriers available for surface transfer. Additionally, the intrinsic disorder found in amorphous semiconductors adds to the number of the extra energy levels, again lowering the efficiency of the charge carrier transport to the surface. [166] In colloidal semiconductors of very small radius, the energy levels become quantized and charge carriers become spatially confined, increasing

the effective band gap and producing discrete states in the valence and conduction bands. In small enough particles, there is not enough space within the particles for electron-hole pairs produced by excitation to exist together. [48]

When a semiconductor is in contact with an electrolyte or other electroactive species, a space charge layer forms, and band bending occurs to allow for a continuous electric field between the solid and the solution. When electron-hole pairs are produced by illumination of the semiconductor by the appropriate wavelength of light, this electrostatic field present in the space charge, or depletion, layer allows for the separation of these charges. For colloidal semiconductors, band bending is small, so when light is absorbed, electron-hole pairs are formed in a random way along the path of the light rather than along a depletion layer. The electron-hole pairs then either recombine or diffuse to the surface to be involved in chemistry. Diffusion time to the surface is on the order of picoseconds or less. This diffusion does not have to occur in particles that exhibit quantum size effects because the electron (or hole) wavefunction spreads over the entire particle. [48]

The ability for charge carriers to affect surface chemistry is dependent on their ability to migrate to the surface before recombination. The distance the charge carrier can travel is called the diffusion length, and is dependent on the carrier lifetime. [166] For colloidal semiconductors, this lifetime is generally on the order of femto- to picoseconds, but was measured somewhat longer for hematite. [48, 80] Factors such as crystallinity and surface area may change the charge carrier lifetimes, thereby altering surface reactivity [166]. The crystal structure of iron oxides is a large factor in determining the kinetics of electron transfer [80], although the role of particle size is disputed [80, 166].

Chapter 4

Manganese-Substituted Goethite

4.1 Introduction

Previous work has suggested that the presence of manganese may be a key controlling factor in determining the migration of plutonium in the geosphere. However, manganese is rarely found as a pure mineral phase; rather, it is more often associated with other more common mineral phases. Iron oxides, such as goethite (α-FeOOH), are very prevalent in the geosphere, and can become substituted with other cations, including manganese. To further model environmental minerals, we have synthesized and extensively characterized manganese substituted goethite containing 0.5 % to 20 % manganese. The interactions of these model minerals with plutonium may lead to a much greater understanding of plutonium migration, integral to risk assessment analysis for underground geological repositories. Extensive characterization of these minerals is key to understanding their physical properties and their interactions with the surrounding environment.

There has been consistent interest in substituted goethite minerals. Schwertmann and Cornell synthesized minerals with substitutions between 5 % and 15 % [126], Alvarez *et al.* between 3 % and 12 % [2], and Gasser 2.5 % to 12.5 % [44]. However, these previous reports did not describe small percent substitutions on the order of 1 % substitution and less. These very minor substitutions may still be very prevalent in the geosphere and important for the behavior of aqueous plutonium.

The original course of this work was to prepare manganese-substituted goethite samples of varying substitutions and then investigate the role of the manganese percentage on the sorption properties of Pu(VI). The portion of this study undertaken in this work is the synthesis and characterization of the Mn-substituted goethite. For information on some additional characterization as well as the sorption of Pu(VI) to the surface, the reader is referred to the thesis of Yung-Jin Hu [61] and Hu *et al.* (2010) [62]. For the initial studies of Pu(VI) on unsubstituted goethite the reader is referred to the thesis of Richard E. Wilson (2005) [176].

4.2 Synthesis

Mn-substituted goethite (($Fe_{1-x}Mn_x$)OOH) samples were synthesized by a method that was adapted from Vempati *et al.* [165] The mole fraction of Mn, Mn_x, is defined as

$$\frac{nMn}{(nMn + nFe)} \tag{4.1}$$

where nMn is the number of moles of manganese and nFe is the number of moles of iron in the substituted mineral. Percent substitution is obtained by multiplying the mole fraction by a factor of 100. The percent substitution ranged from 0.01 % to 20 %, although it was determined that the minimum characterizable percent substitution was 0.5 %. Thus, the work reported here was performed with 0.5 % substitution and greater only.

For the substituted goethite samples, 100 mL of a 1 M $FeCl_3$ solution was mixed with 100 mL of a $MnCl_2$ solution, whose concentration was dependent on the desired Mn mole fraction, in a 1 L polypropylene beaker. After 5 minutes, 200 mL of 7 M NaOH solution was added slowly. The resulting dark brown precipitate was stirred vigorously. The suspension was allowed to rest for 1 hour at room temperature with intermittent stirring. Excess NaOH was poured off and the remaining suspension was centrifuged at 3000 rpm for 10 minutes. The precipitate was resuspended with 18.2 MΩ (Milli-Q) water and recentrifuged with the same parameters three times. On the third time the supernatant was always somewhat cloudy. Supernatants were poured off and the solid resuspended with 500 mL of 0.3 M NaOH in a 1 L polypropylene beaker. The beaker was covered with a watch glass and incubated at approximately 70 °C in a convection oven for a minimum of 48 hours. Care was taken not to exceed this temperature to prevent the formation of the hematite phase. The solid was rinsed repeatedly with Milli-Q water and suspended in dialysis tubing (SnakeSkin Pleated Dialysis tubing 3500 MWCO) in Milli-Q water exchange solution until the conductivity of the exchange solution was $\leq$ 2.0 μS. The product was then dried in a convection oven at about 60 °C, ground using an agate mortar and pestle, and sieved. The 63-212 μm fraction of the Mn-substituted goethite was used for experiments reported below except where noted otherwise.

4.3 Structure, Size, and Shape

4.3.1 X-ray Diffraction

X-ray diffraction (XRD) uses the diffraction of X-rays with crystalline materials to elucidate the crystal structure. In diffraction an incident X-ray wavefront consisting of multiple in-phase rays, encounters a crystal from an angle θ. The atoms of this crystal are arranged in parallel planes spaced a distance d apart. When the rays interact with the crystal, they will interact with each of these parallel layers. Atoms will scatter X-rays in all directions, and some of these directions will be equal to the angle θ of the incident radiation. When this is the case, the scattered rays will again be traveling in the same direction and in phase, forming a diffracted beam, which is defined as "a beam composed of a large number of scattered rays mutually reinforcing one another." [29] This scattering phenomenon is shown in

Figure 4.1 and described by the Bragg equation:

$$\lambda = 2dsin\theta \tag{4.2}$$

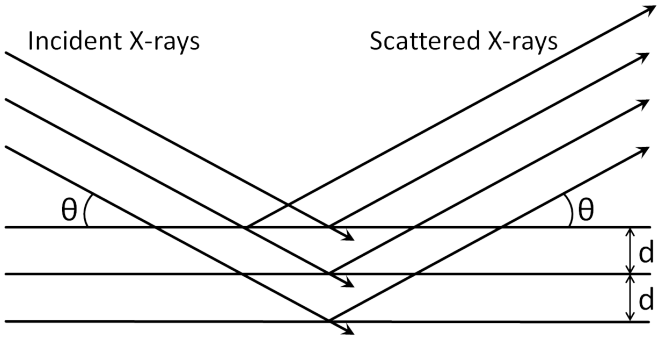


Figure 4.1: Diffraction of X-rays by a crystal.

The angle between the incident and the diffracted beam is always 2θ, so data are displayed as the intensity as a function of degrees 2θ. This diffractogram will show peaks corresponding to the crystal planes of the particular material, which are therefore identifying for that particular material and incident X-ray energy.

The 63-212 μm size fraction was investigated with X-ray diffraction (XRD) for structure. The X-ray diffraction pattern was measured over a 2θ angle from 15 to 100 degrees on a PANalytical X'Pert Pro powder X-ray diffractometer using Co K_α radiation with an Fe filter pressed onto a zero background plate. 9-12 scans of two hours each (using a step size of 0.0042 and 45 seconds per step) were averaged for the final diffractogram.

The X-ray diffractograms (Figure 4.2) matched the structure of goethite with a slight peak shift to lower 2θ at small angles and higher 2θ at large angles with increasing manganese substitution. This shift is due to the change in lattice parameters with the substitution of an ion with a different ionic radius. Specifically, this substitution induces a reduction of the a-, and c-crystallographic parameters and an increase in the b-crystallographic parameter. [133]

4.3.2 Scanning Electron Microscopy

Scanning electron microscopy (SEM) is a technique for imaging solid surfaces at the sub-micron scale. A highly focused electron beam is rastered over a sample, which emits electrons and X-rays that can be detected to make an image. The images can come from low-energy secondary electrons created by beam interactions with the surface or from backscattered beam electrons. Using backscattered electrons will make the images look three dimensional and because the brightness increases with increasing atomic number, the image is indicative of composition. However, good depth of field can still be achieved with secondary electron detection. Samples are mounted on a conductive surface and held under vacuum for measurement. [92] The penetration depth of the electrons is dependent on the electron energy and the elemental composition of the sample, but ranges from less than 100 nm to 10 μM [93].

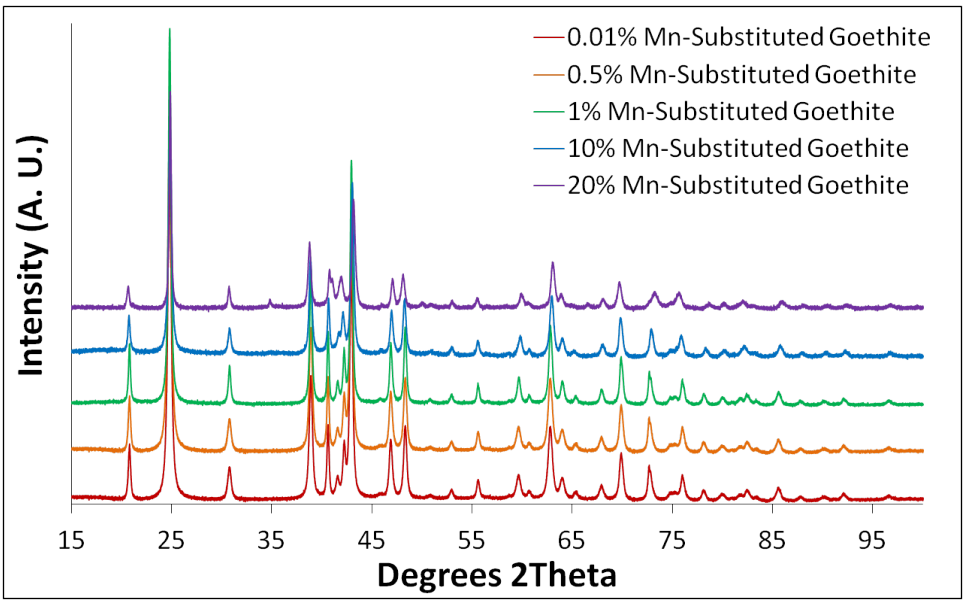


Figure 4.2: X-ray diffractograms of goethite and Mn-substituted goethite showing the shift in 2θ with increasing manganese substitution.

The 63-212 μm size fraction was investigated with scanning electron microscopy for size and shape. The scanning electron micrographs were taken on a JEOL 6340F FESEM at 5 kV and 12 μA and on a LEO Model 440 SEM.

The SEM showed that the grains were mostly in the 63-212 μm size range (Figure 4.3), so sieving is isolating the correct size fraction. At a higher magnification it was clear that the larger grains were made from aggregations of the characteristic goethite crystallite needles approximately 1 to 5 microns in length and a few to 30 nanometers wide, easily visible in Figures 4.5 and 4.6. The crystallites for the manganese-substituted goethite have a greater length-to-width ratio than unsubstituted goethite.

However, there is a difference between samples that were dry mounted for measurement and samples that were dried onto a substrate from solution. The dry-mounted samples generally maintained their size and shape while mounting, with only a few particles obviously breaking apart into a size that should have sieved out if it had been in the original material. However, in the wet-mounted samples there was an abundance of smaller broken-up particles, particles that had aggregated to each other (Figure 4.4), and loose crystallites (Figure 4.6). This suggests that when the goethite particles are resuspended into solution after sieving there is an overall increase in the range of particle sizes, with some aggregation to larger sizes, but likely a greater amount of particle size reduction. This maybe be particularly important with respect to the increase in the number of loose crystallites in solution, as this both greatly increases the surface area and may change the surface and/or electronic properties of the solid.

Goethite and other minerals are often considered as fully solid particles rather than aggregates of micron- and nano-sized crystallites. Considering them instead as aggregates may alter the way we imagine processes such as particle growth, elemental substitution, and surface chemistry.

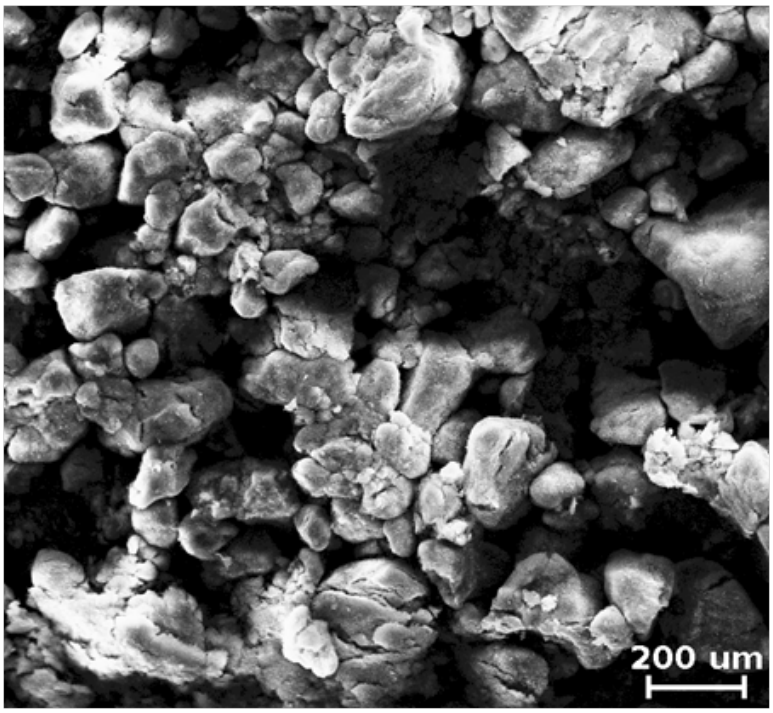


Figure 4.3: Scanning electron micrograph of 1 % Mn-substituted goethite showing the morphology of the goethite particles.

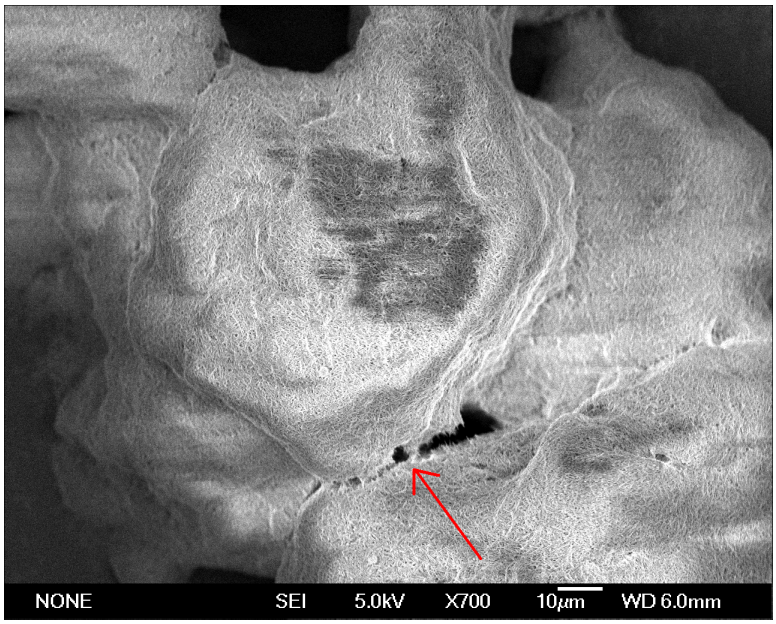


Figure 4.4: Scanning electron micrograph of 1 % Mn-substituted goethite showing the level of surface roughness and a broken joint between two particles that had aggregated during wet-mounting (arrow). Individual needle-shaped crystallites can almost be seen to form the surface.

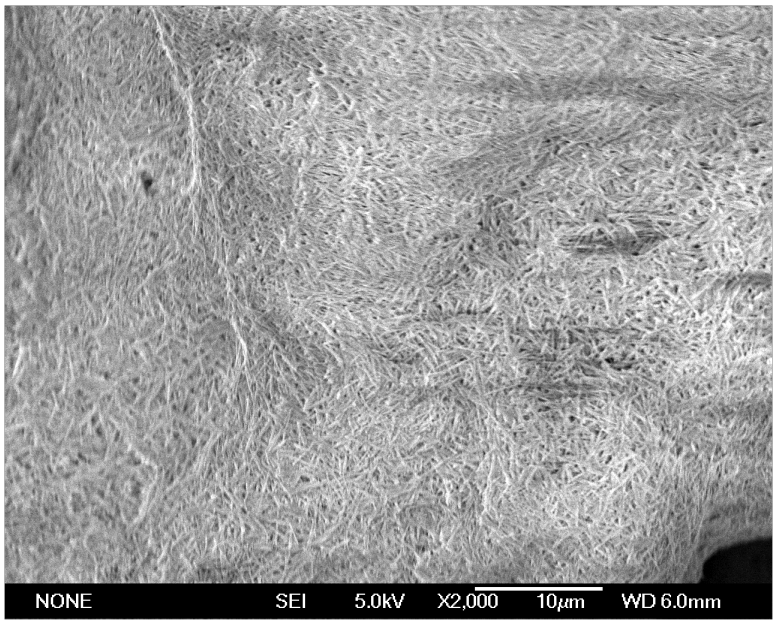


Figure 4.5: Scanning electron micrograph of 1 % Mn-substituted goethite showing the formation of the particle surface by the aggregation of small needle-shaped crystallites.

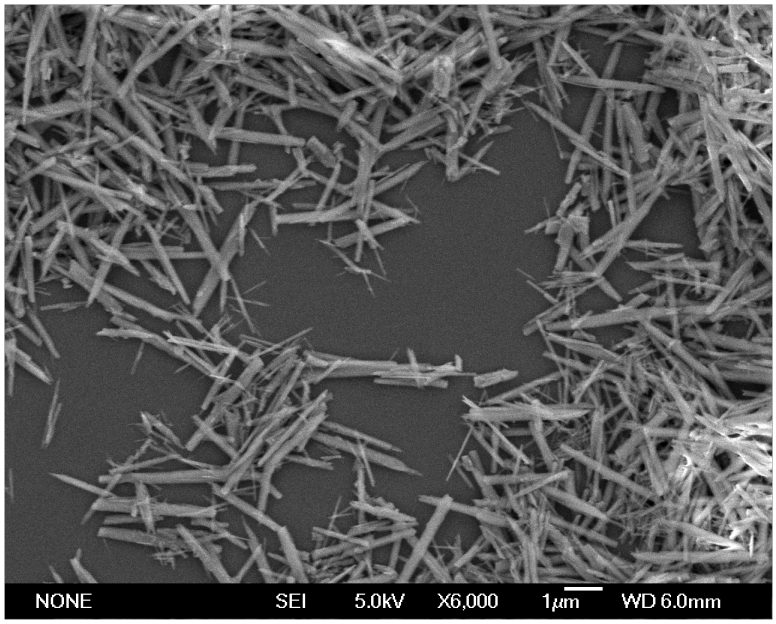


Figure 4.6: Scanning electron micrograph of 0.5 % Mn-substituted goethite showing individual needle-shape crystallites broken off from a larger particle.

4.4 Percent Substitution and Manganese Distribution

The percent substitution was measured by three methods: inductively-coupled plasma-mass spectrometry (ICP-MS) of dissolved particles, and X-ray photoelectron spectroscopy (XPS) and energy dispersive X-ray spectroscopy (EDS) of solid particles.

For a description of ICP-MS, refer to Appendix A. For measurement with ICP-MS, samples were fully dissolved in a solution of 1 M oxalic acid and 0.01 M L-ascorbic acid at room temperature. These solutions were then filtered, properly diluted, and the elemental composition of Mn and Fe measured using a Perkin-Elmer Elan DRC II ICP-MS with a Sc or Ga internal standard. Most samples were measured using the dynamic reaction cell (DRC) with NH_3 reaction gas. The procedures used for sample and standard preparation are presented in Appendix A. Mn and Fe concentrations were calculated by normalizing to the internal standard after application of a 5-point linear calibration. Results of these experiments are shown in Table 4.1.

X-ray photoelectron spectroscopy (XPS) is a surface spectroscopy technique to measure elemental composition, chemical state, and electronic state. A sample under high vacuum is irradiated by a soft X-ray beam while the kinetic energy and number of emitted electrons are measured. Measurement of the electrons gives the electron binding energy of those electrons. Samples need to be held under ultra-high vacuum, but do not need to be conductive. Only the electrons in the top 10-12 nm of the material are detected, so XPS is only a surface analysis technique. [92] XPS measurements were performed by Ravi Kukkudapu using an INCAWave 7060 X-ray photoelectron spectrometer.

In energy-dispersive X-ray spectroscopy (EDS or EDX), the spectrum of X-rays emitted by a sample due to a high energy electron beam, such as that in an SEM, is used to perform elemental analysis. The electron beam removes inner shell electrons from the sample, which causes the emission of characteristic X-rays when higher energy electrons fill the core holes. These X-rays are measured by a Si detector and converted to an energy spectrum that can be used for determining the percent composition of a sample. [160] The penetration depth of the electrons depends on both the accelerating energy and the density of the material. For goethite (density of 4.28 g/cm^3 [119]) under a 20 keV electron beam, this depth is approximately 2 μM [93]. However, the depth at which the electrons have enough energy to generate the characteristic X-rays is somewhat less than this.

For energy dispersive X-ray analysis measurements, samples were either adhered to a conductive carbon tape or dispersed from solution onto a Si wafer and then measured using a JEOL 6340F FESEM equipped with EDAX EDS at 20 kV and 12 μA settings. The spectrum was measured for a sufficient amount of time to measure 10,000 counts in the 6.4 keV bin of the peak of the primary Fe K_α peak (generally 15-25 minutes). This unfortunately meant that the Mn peak bin that does not overlap with Fe had only a few hundred counts, but this is also measured at just one bin in that peak and not the peak integral, so the data is still trustworthy. This is also why multiple measurements were made for averaging. For low percent substitutions, often the regression program was able to calculate an atomic percent for the Mn when no Mn peak was visible above background. Thus, it seems that the limit of detection for Mn in an iron-rich sample is around 0.5 %. Results of these measurements are in Table 4.1.

The percent composition as measured by the three techniques clearly differs quite signif-

Theoretical % Mn	ICP-MS Avg	XPS Avg	EDS Avg
Alfa Aesar 0 %	0.051 (0.007)	Not Measured	0.23* (0.08)
YJH 0 %	0.07 (0.05)	Not Measured	0.49* (0.09)
LKS 0.01 %	0.06 (0.06)	Not Measured	0.55* (0.09)
EC 0.01 %	Not Measured	0.57 (0.12)	0.44* (0.08)
LKS 0.1 %	0.03 (0.07)	1.37	0.49* (0.02)
LKS 0.5 %	0.4 (0.1)	Not Measured	0.95 (0.02)
YJH 0.5 %	0.56 (0.07)	2.01	1.2 (0.3)
LKS 1 %	0.8 (0.2)	Not Measured	1.54 (0.04)
YJH 1 %	1.1 (0.1)	3.26 (0.39)	1.61 (0.07)
LKS 10 %	9 (1)	14.18 (0.05)	10.0 (0.3)
LKS 10 % >600 μm	Not Measured	Not Measured	10.4 (0.1)
LKS 20 %	19 (3)	24.87 (0.09)	18.5 (0.2)

Table 4.1: Percent substitution of Mn-substituted goethite as measured by ICP-MS, XPS, and EDS. When more than one measurement was made, the standard deviation is in parentheses for XPS and EDS. The error in parentheses for ICP-MS represents 1 σ. All measurements are for the 63-212 μm size fraction unless otherwise noted. A * next to an EDS measurement indicates that no peak was visible.

icantly (see Table 4.1). The values from ICP-MS are always lower than those measured by EDS, which are always lower than those measured by XPS. This is also in order of decreasing penetration depth, with ICP-MS measuring the fully dissolved particle, EDS measuring the top few layers of crystallites, and XPS only measuring the top few nanometers of the samples. Because the ICP-MS results are the only ones guaranteed to be representative of the entire particle and are from the technique with the best limit of detection, these concentration values were used for the overall percent composition.

Combining the penetration depth characteristics with the data leads to the suggestion that the manganese is more concentrated on the surface of the particles, with the phenomenon being more pronounced at lower concentrations. This is in partial agreement with the literature where the distribution of manganese was measured by comparing the amount of Fe and Mn over time during particle dissolution. Several authors found a homogeneous manganese distribution by dissolution [1, 83], but further work by Alvarez showed that the Mn tended to be concentrated toward the surface [2, 3]. Furthermore, the distribution became more even as the percent substitution of manganese increased [3], which is also in agreement with the results shown here. An experiment was attempted to measure the amount of Fe and Mn over time during particle dissolution using 5.5 M HCl, but unfortunately the filters held up poorly to the acid (see Appendix D), and the results at low concentration, corresponding to the dissolution of the outermost part of the particles, were unusable. The experiment therefore did not support or contradict either literature result.

Because the particles are made up of small crystallites (see Section 4.3.2), this implies that the particles begin to nucleate from crystallites made entirely of iron and that the Mn-substituted crystallites are not incorporated until later in the nucleation process. This

either implies that Mn-containing crystallites form later and are therefore incorporated more heavily onto the surface of grains that have already begun forming, or there is some property of Mn-containing crystallites that causes them to not nucleate at the center of new particles. EDS measurements of the 10 % substituted goethite at two different size fractions (20-63 and 63-212 μM) gave the same percent composition, implying that the substitution was not a function of particle size, and supporting the latter of the two suggestions. If the Mn-containing crystallites formed later, then different size fractions would be expected to have differing percent compositions.

4.5 Solubility of Mn-Substituted Goethite

The equilibrium solubility of 0.5 % and 1 % Mn-substituted goethite in 0.1 M $NaClO_4$ was determined from pH 3-9. 0.4 g of 63-212 μm size fraction mineral was placed in an acid-washed glass bottle with 100 mL of pH solution. The samples were opened to air and no effort was made to exclude carbonate in order to more closely mimic a natural system. A perchlorate matrix was chosen because perchlorate has previously been shown to play no part in the goethite dissolution reaction [25]. To account for slow kinetics, the samples were allowed to shake on an orbital shaker at 120 rpm for 31 months following a 10-day pH balancing period where the pH was monitored and adjusted using $HClO_4$ and NaOH. The long time period prior to measurement guaranteed that the samples had reached equilibrium. The solutions were also shaken periodically to ensure that a new surface was exposed to the solution. Aliquots were removed, filtered using an Amicon 4 mL regenerated cellulose filter, and analyzed for Mn and Fe content using ICP-MS (see Appendix A). Duplicate samples were taken of each solution and measured for 5 replicates. Fe was measured for both ^{54}Fe and ^{56}Fe, where manganese was only measured for ^{55}Mn. All replicates, duplicates, and isotopes were averaged for each solution, and the results are shown in Figures 4.7 and 4.8.

As expected, the iron solubility quickly drops below the limit of detection (approximately 0.1 ppb) for the ICP-MS. The expected solubility for goethite falls below 0.1 ppb by pH 3.3, which is in accordance with the data presented here. The solubility at pH 3 is slightly higher than expected, but only by about one order of magnitude, which could easily be accounted for if the measured solution pH was measured high by just half a pH unit. It is at least consistent that the solution with the lower measured pH, the 1 % solution, had a higher iron solubility. Alvarez *et al.* (2005) also found that the incorporation of Mn(III) into goethite can significantly destabilize goethite against proton attack [3], so this may also explain the increase in solubility shown here.

The manganese solubility is significantly higher than that of iron, but lower than other manganese oxides, such as pyrolusite and cryptomelane (see Appendix B). This is not surprising given the low percent substitution and the likely incorporation of at least some of the manganese into the particle, leaving it unexposed to the solution. If all of the Mn were to dissolve, then the Mn concentration would be about 12.6 ppm for the 0.5 % solution and 25.3 ppm for the 1 % solution, rather than the 0.5 and 0.7 ppm, respectively, measured. Unfortunately, the solubility of groutite, which is the Mn mineral isomorphous with goethite, was not available for comparison. However, given the solubility of two other manganese oxides, cryptomelane and pyrolusite, are both higher at pH 3 than the 12.6 ppm contained

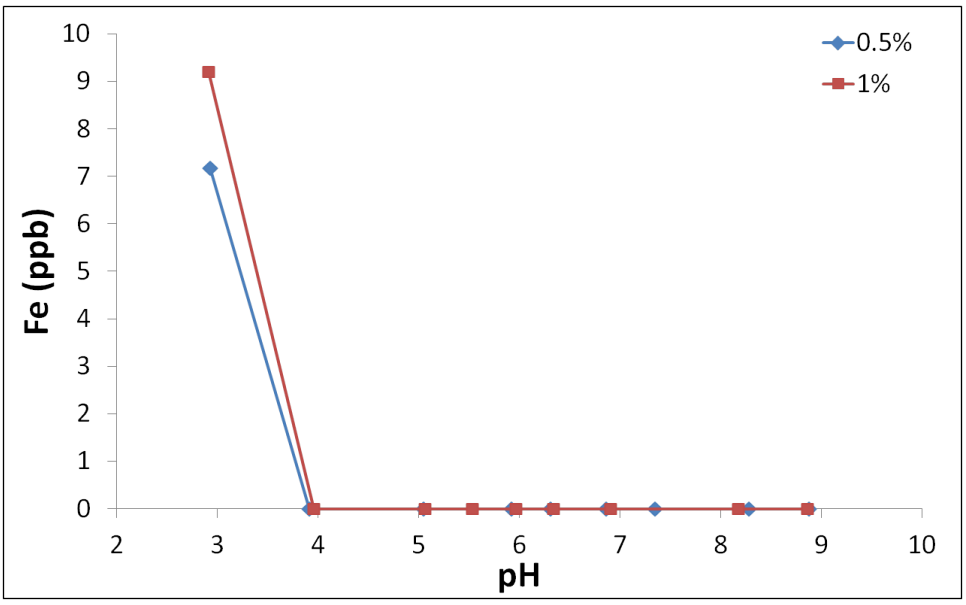


Figure 4.7: Solubility of iron as a function of pH for 0.5 % and 1 % manganese-substituted goethite. Lines are added to guide the eye and vertical error bars of 1 σ are contained within the data points.

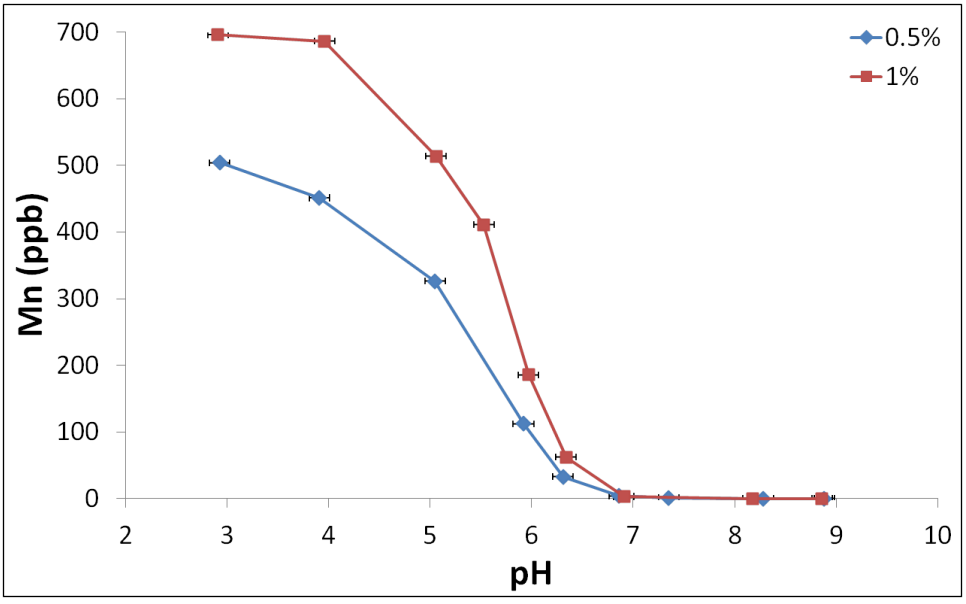


Figure 4.8: Solubility of manganese as a function of pH for 0.5 % and 1 % manganese-substituted goethite. Lines are added to guide the eye and vertical error bars of 1 σ are contained within the data points.

in the 0.5 % sample (Appendix B), presumably if all of the Mn were on the surface, it could have dissolved.

Making an assumption that the amount that did dissolve is equal to or strongly related to the percentage of the total Mn present on the surface, and estimating the total Mn present based on the sample added, a quick calculation can be done to see how well incorporated into the particle the Mn is. This calculation (using the ICP-MS percent substitution listed in Section 4.4 reveals that about 4.0 % of the manganese for the 0.5 % substituted goethite dissolved, and 2.8 % of the manganese for the 1 % substituted goethite dissolved. This suggests that the Mn subsitutes more heavily toward the surface than the center of the particle. For the 63-212 μm size fraction used in this experiment, the surface area to volume ratio ranges from 0.048 to 0.015. If the Mn were evenly distributed, then doubling the amount of Mn should only add between 1.5 and 4.8 % to the dissolved Mn. Because at pH 3 more than 38 % was added by doubling the Mn substitution, this is a clear indication that the Mn is likely not evenly distributed. This is not to say that the solution will not be able to reach several layers below the surface, but with such a low percent subsitution and very low iron solubility, it is highly unlikely that an even distribution throughout the particle is occuring. This assessment is supported by the difference between XPS, EDS, and ICP-MS measurements made on the percent composition (Section 4.4).

Chapter 5

Ferrihydrite

5.1 Introduction

Ferrihydrite is a common mineral phase with variable low crystallinity ranging from poorly crystalline 2-line to more crystalline 6-line ferrihydrite [26]. X-ray diffraction (XRD) patterns of two-line ferrihydrite are characterized by two broad reflections (Figure 5.9), while for six-line ferrihydrite six reflections are visible. This variety of crystallinity is associated with a poorly defined stoichiometry and an atomic structure that is not well established. The exact structure is difficult to determine due to the high water content, but is most recently determined to be $Fe_{10}O_{14}(OH)_2$ [95]. It has been proposed that the surface Fe^{3+} ions are octahedrally coordinated within a hexagonal unit cell, whereas the Fe^{3+} ions located in the center of the particle (about 20 %) have a tetrahedral coordination [95, 183].

Ferrihydrite is often found and formed as a suspended colloidal species in natural waterways [65, 169]. This type of synthesis leads to 2-6 nm particles with little to no aggregation. However, when the suspended material is dried, these particles aggregate into larger, irregular particles with much greater surface roughness and small micropores formed between particles. This change in structure is permanent; the particles do not redisperse when the dried material is put back into aqueous solution. These structural changes may also impart changes in surface chemistry. [46]

Ferrihydrite is also the precursor to the other common more crystalline mineral phases goethite and hematite, and ages to them during the span of several weeks to several months depending on the conditions. [26, 39] It has been shown previously that the presence of silica in the structure can stabilize the ferrihydrite against aging. [14, 164]

Due to the high surface area, hydroxyl surface groups, and high natural sorption capacity of ferrihydrite, ferrihydrite may prove to be an excellent material for the detection and separation of the lanthanides and actinides. However, its properties may change as the material undergoes aggregation. [46] Nanoparticulate ferrihydrite as both a suspended and a dried material have been synthesized; the synthesis is described in Section 5.3.1. 3D cubic ordered mesoporous 2-line ferrihydrite (denoted as mesoporous ferrihydrite) was also prepared; the synthesis can be found in Section 5.3.2. All three of these materials were characterized for size, shape, crystallinity, percent composition, surface area, and point of zero charge (Sections 5.5 through 5.8). They were also investigated with respect to plutonium sorption,

both as a function of pH (Sections 5.9 and 5.9.4) and light exposure (Section 5.9.3). All three materials were found to be excellent sorbents for Pu(VI), although the nanoparticulate appeared to sorb more strongly. X-ray absorption spectroscopy measurements at various pH conditions were also performed to determine the plutonium oxidation state following sorption (Section 5.9.6).

5.2 Structure

The ideal ferrihydrite structure is described as central FeO_4 tetrahedra surrounded by FeO_6 octahedra (Figure 5.1) [95]. This means that the ferrihydrite surface should be composed of octahedral Fe(III). Assuming octahedral iron, there are several possibilities for surface binding sites for sorbed metals. Gilbert *et al.* [46] show several potential metal ion sorption sites based on extended X-ray absorption fine structure (EXAFS) measurements of Cu(II) bound to ferrihydrite nanoparticles, shown in Figure 5.2. Pu(VI) is a plutonyl cation (see Figure 2.1), but this diagram will still include the possible sorption sites. The axial oxygens may prevent some of these sorption sites from being viable.

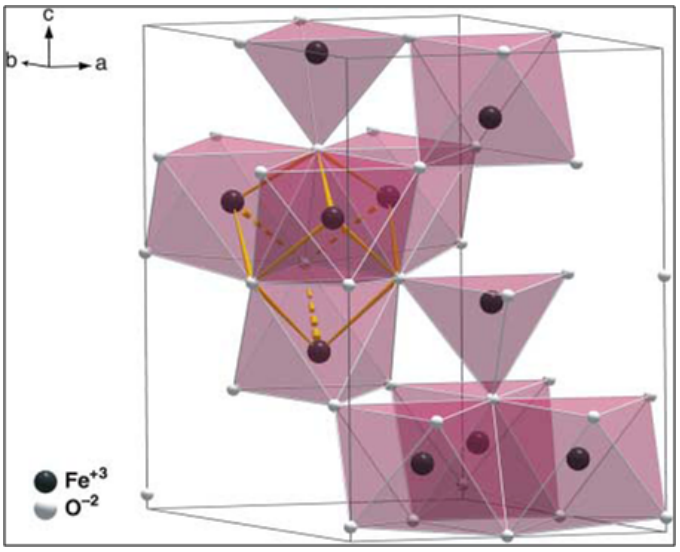


Figure 5.1: Hexagonal unit cell model for ferrihydrite. From Michel *et al.* (2007) [95].

Although many iron oxides form plate-like particles, ferrihydrite forms 1-10 nm spheres [39], as shown in Figure 5.3, which aggregate into larger particles at higher pH, higher ionic strength, and upon drying [46]. At low pH the particles repulse each other due to the high surface charge. An increase of the pH will reduce the surface charge, allowing for aggregation. Similarly, an increase in ionic strength will shield the surface charge, allowing for aggregation. Overall, however, particles that remain in solution tend to aggregate into only very open structures with little to no pore structure that do not greatly reduce the effective solution surface area. Drying, on the other hand, will reduce the surface area and significantly change the structure of the aggregates to a much tighter structure with internal nano- and micropores. The regularity and connectivity of the pores may be dependent on

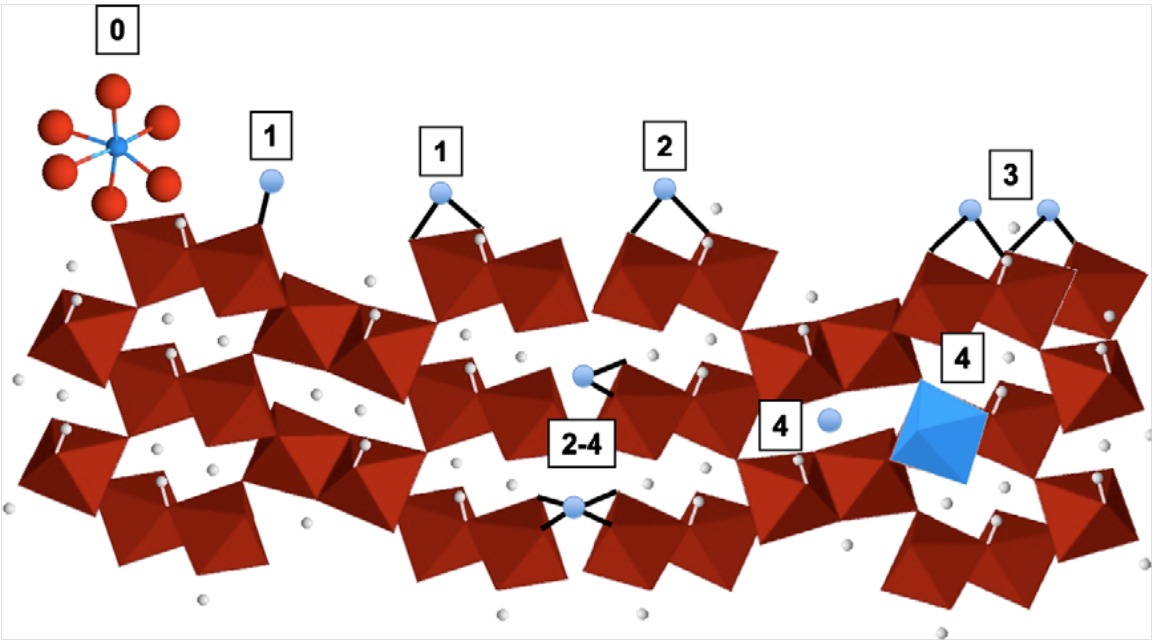


Figure 5.2: Possible sorption sites on ferrihydrite. Coordinating oxygens around the metal cations (blue) are generally not shown for simplicity. The boxed numbers indicate the number of possible second neighbors visible in EXAFS data. From Gilbert *et al.* (2009) [46].

drying temperature, with 50 °C being the most regular and most connected. However, lower temperatures do not seem to greatly decrease the connectivity of the pores. [46]

5.3 Synthesis

5.3.1 Nanoparticulate Ferrihydrite

The synthesis of nanoparticulate ferrihydrite has previously been described in the literature [26]. Ten grams of $Fe(NO_3)_3 \cdot {}_9H_2O$ (99.99 %, Aldrich) is added to 125 mL Milli-Q doubly-distilled water. While stirring, approximately 110 mL of 1 M NaOH is added slowly (over 30-60 minutes) until the solution pH reaches a stable value between pH 7 and pH 8 [39]. Care should be taken to avoid overshooting, as this can cause greater particle aggregation [46]. The solution is then centrifuged, the supernatant removed, and the solid resuspended with Milli-Q water. This process is repeated at least once before transferring the solid to 3500 MWCO SnakeSkin pleated dialysis tubing (Thermo Scientific), which is left in dialysis against Milli-Q water until the solution conductivity reaches a steady number below 10 μS. The solid is then removed and either left open to air to dry in a hood for the dried ferrihydrite or suspended in water and equilibrated to a pH near 4.5 using $HClO_4$ for the suspended ferrihydrite. The dried material is ground with a mortar and pestle before use, as it dries into a very solid chunk. A portion of the suspended ferrihydrite can be both dried and weighed or dissolved and analyzed using ICP-MS to determine the particle concentration. A suspended "ferri-goethite" was made by allowing a ferrihydrite suspension to age to be

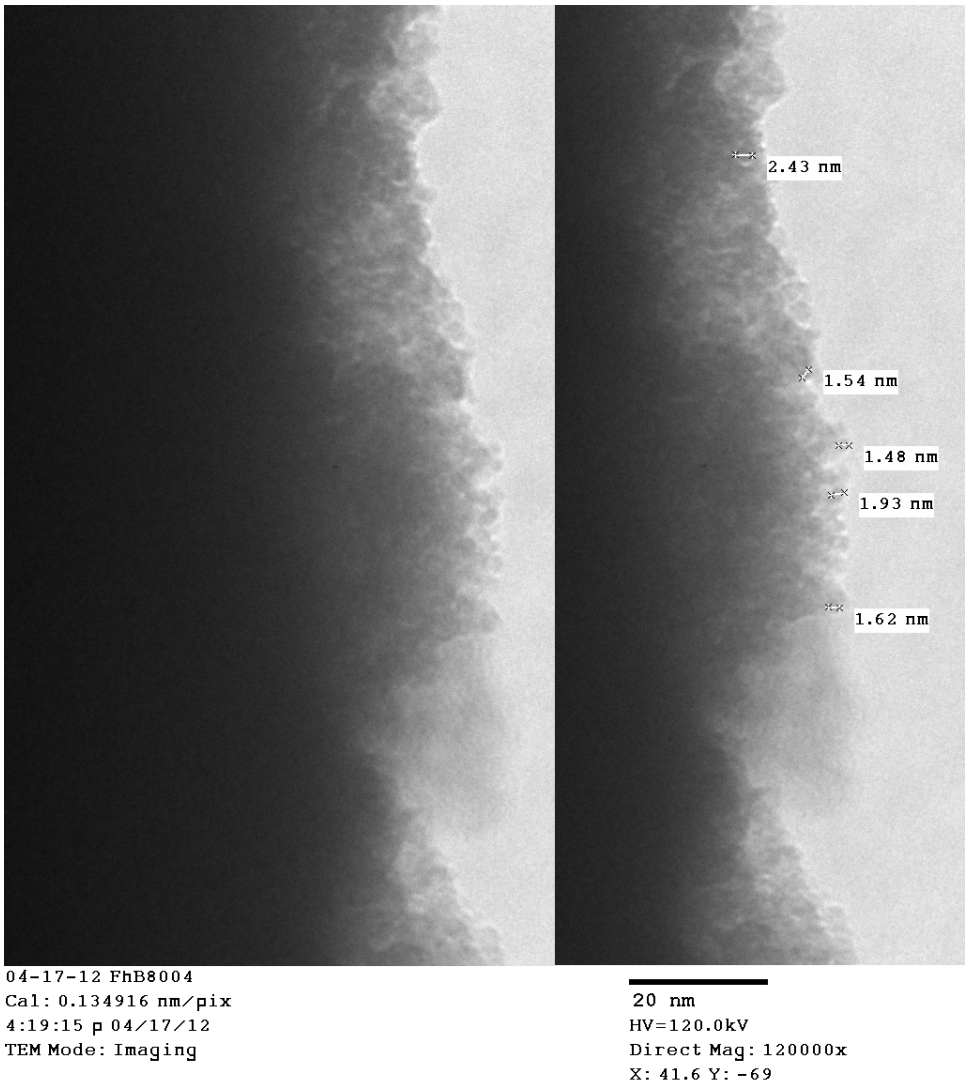


Figure 5.3: Transmission electron micrograph (TEM) of suspended ferrihydrite dried to a carbon grid. Right image shows approximate particle size measurements of particles visible in the left image. Diameters were measured using the software ruler feature.

primarily goethite with some ferrihydrite contribution.

The mechanism involved in this aqueous synthesis by hydrolysis and precipitation can be described by the following reactions. It is well known that the aquo complex of Fe(III), $Fe(H_2O)_6^{3+}$, decomposes readily into several species by the deprotonation of water molecules, such as is shown in Reaction I below. This reaction can be promoted by heating or the addition of base or an oxidant (proton acceptor). Following this, there are two possible methods of condensation or polymerization of the aquo iron complexes: olation (Reactions II and III) and oxolation (Reaction IV). In olation hydroxide bridges form between iron atoms, and in oxolation, oxide bridges form. Upon the increase of pH or temperature, further hydrolysis and condensation occurs, causing the formation of colloidal inorganic polymers. In the case of iron nitrate, as is the case for the synthesis employed here, the initial form of these polymers may be $Fe_4O_3(OH)_4(NO_3)_2 \cdot 1.5H_2O$. With continued addition of base, the formation of ferrihydrite occurs and a solid phase precipitates. [38, 39, 71]

Reaction I: $[Fe(OH_2)_6]^{3+} + H_2O \rightarrow [Fe(OH)(OH_2)_5]^{2+} + H_3O^+$

Reaction II: $[Fe(OH)(OH_2)_5]^{2+} + [Fe(OH_2)_6]^{3+} \leftrightarrow [(H_2O)_5Fe(OH)Fe(OH_2)_5]^{5+} + H_2O$

Reaction III: $2[Fe(OH)(OH_2)_5]^{2+} \leftrightarrow [(H_2O)_4Fe(OH)_2Fe(OH_2)_4]^{4+} + 2H_2O$

Reaction IV: $2[Fe(OH)(OH_2)_5]^{2+} \leftrightarrow [(H_2O)_5FeOFe(OH_2)_5]^{4+} + H_2O$

5.3.2 Mesoporous Ferrihydrite

To the author's knowledge, only four other groups have synthesized mesoporous 2-line ferrihydrite [82, 91, 139, 177], although syntheses are reported for 6-line ferrihydrite [23, 24] and other mesoporous iron oxides formed from ferrihydrite [71]. Mathew *et al.* at Toyota were interested in the removal of ozone and organic contaminants from air [90, 91], while Xia *et al.* were interested in low-cost cathodes for rechargeable batteries [177]. The Mathew synthesis was a surfactant-assisted precipitation in 1-propanol, and yielded a material with a disordered mesoporous structure of intraparticle pores between particles formed by nanoparticle aggregation that was lacking in long-range structural order and had a surface area less than 200 m^2/g. The Xia synthesis involved using layered double oxides and hydroxides as pseudo-templates and the formation of ferrihydrite by treating them with dilute nitric acid. This synthesis yielded a material that was claimed to have a more homogeneous pore size distribution than dried nanoparticulate ferrihydrite with surface areas up to 450 m^2/g [177], although the corresponding surface area and pore analysis data were not displayed. The material created by Li *et al.* by precipitation under sparging air [82] was cited to have 3.8 nm pores. While there are definitely irregular pores in the solid, as they are visible in the transmission electron micrograph, the pore size distribution analysis was performed on the desorption branch, and thus it is likely that the large narrow peak at 3.8 nm is due to the tensile strength effect (TSE) and not real pores, although this cannot be confirmed without investigation of the adsorption branch pore size distribution [50]. Smith *et al.* used a solvent

deficient synthesis with iron nitrate and ammonium bicarbonate ground together to make ferrihydrite with 3.4 nm pores. The authors unfortunately do not describe their pore analysis method, and thus their work is in the same category of Li *et al.* where pores are visible in TEM images but the pore size distribution cannot be confirmed.

The synthesis presented here is adapted from H. Tüysüz, and prepares 2-line ferrihydrite with a regular, ordered network of pores. The quantities listed are for 1 g of KIT-6 (Korea Advanced Institute of Science and Technology [73]) starting material. It follows a nanocasting approach to create the mesoporous structure and uses the thermal decomposition of iron nitrate to produce the ferrihydrite. [164]

The precursor consists of 30 mL of 0.8 M $Fe(NO_3)_3 \cdot 9\,H_2O$ (MW 404 g/mole) in ethanol. 12 mL of this solution is added to 1 g of KIT-6 in a glass large-bottomed vial (large enough to make a thin layer, but no so large that there is empty space), and stirred for 1-2 hours. The magnet is removed and the sample placed into the oven overnight at 50-60 °C to completely evaporate the ethanol. The material dries to a homogeneous yellow color similar to that of goethite. Once the ethanol is evaporated, the solid is mixed and calcined at a higher temperature (dependent on the oven; see discussion below) for 4-6 hours. The process of addition, stirring, evaporating, and calcining is repeated two more times (although a good product can still be made with only one repetition). The silica template can be removed by dispersing the solid in 25 mL of 2 M NaOH in a plastic container. The solution is shaken end over end (or stirred, but shaking is better) at room temperature for 1-2 hours, then put into the oven at 50-60 °C for overnight, up to 24 hours, while shaking the bottle every few hours. The liquid can easily be decanted after centrifuging, and a fresh 25 mL of 2 M NaOH added. The shaking/stirring is repeated for 1-2 hours and then the material is placed into the warm oven for 8-10 hours. The solid is then filtered and washed with Milli-Q water until neutral (or the solid can be run through dialysis until the conductivity is low, generally below 2 μS). The powder is dried at 50-80 °C and gently crushed into a powder. The final product should not need grinding. It should also be noted that the KIT-6 template leaves behind 1-2 % Si in the ferrihydrite structure, although this can be completely removed using HF instead of NaOH to remove the template. However, it is this small percentage of Si that stabilizes the mesoporous ferrihydrite from aging [14, 164]. If the sample is not agitated sufficiently during the removal of the silica template the removal can be quite uneven, and and lead to non-uniform pore sizes and/or blocked pores.

The calcining temperature is one of the most important and sensitive parts of the synthesis. The temperature needs to be high enough to decompose the iron nitrate, but not so high that hematite (Fe_2O_3) forms instead of ferrihydrite. This temperature can actually be quite a small working range depending on the conditions and equipment in the laboratory. The temperature necessary to decompose the iron nitrate is dependent on two main factors: heating rate and air flow. In general, increasing the rate of heating to the final temperature lowers the temperature of decomposition [40, 70]. Additionally, the flow of nitrogen or air also lowers the temperature of decomposition [40]. The effect seems to be greater for air flow, but both help to carry away the gas products produced by the decomposition, which include H_2O, NO_2, N_2O, NO, and O_2 [28, 159]. These general trends are supported by the results of several authors [70, 108, 128, 144, 174], which can be used to determine the most appropriate calcining temperature for a particular oven setup. These results and the corresponding conditions are shown in Table 5.1.

°C per Min.	Flow	Decomposition Temp.	Ref.
3	None	Peak at ~155.8 °C, over by 160 °C	[174]
5	None	Starts at 60 °C	[28]
5	None	250-300 °C	[144]
5-6	None	200-250 °C; 150-200 °C when slower	[70]
6	N_2, 5 L/h	H_2O: 170 °C; NO_2, NO: 185 °C	[28]
10	N_2, 100 mL/min	Fe_2O_3 formation begins at 210 °C	[108]
10	Air, 30 mL/min	Peak at 110 °C, Fe_2O_3 forms at 190 °C	[128]
2-3	Air, top vent	160 °C	This Work

Table 5.1: Experimental parameters relating to the calcining temperature necessary for successful mesoporous ferrihydrite synthesis.

The oven type used for the syntheses labeled as LKSB is a simple top-vented non-programmable oven (HT batches were synthesized in an unknown set-up by H. Tüysüz). With the vent half way open to allow for the escape of NO_x gases, the heating rate is approximately 3 °C per minute (up to 6 °C per minute at lower temperatures and down to 1-2 °C at higher temperatures). Because the vent does allow air exchange, but not significant air flow, the conditions appear to be closest to those from Wieczorek-Ciurowa and Kozak (1999) [174], and thus the ideal temperature for calcining is 160 °C assuming that the sample has been in the oven during the entire heating process. This temperature may be higher if the sample is placed in the oven after heating to the correct temperature as the heating rate of the sample would presumably be significantly increased. However, as this heating rate would be much more difficult to accurately measure, it is prudent to leave the sample in the oven where the heating rate can be measured and adjusted appropriately to maintain a constant rate.

To ensure proper temperature choice, the decomposition reaction can easily be monitored. The sample begins as a warm yellow color, and will begin to change to a reddish-brown at the start of the decomposition reaction (around 120 °C in the oven used here). NO_x gases will not be concentrated enough to be visible, but can be smelled when opening the oven or inspecting the sample vial. At the appropriate temperature, the sample will turn the dull reddish-brown of ferrihydrite. If the temperature is too high, the solid will become redder to attain the blood red-brown color of hematite. Unfortunately, once the appropriate temperature has been surpassed, there is no method to reattain ferrihydrite, with the exception of starting over.

5.4 Percent Composition

Ferrihydrite was analyzed for elemental purity and the Fe:O:Si ratios for each material using energy dispersive X-ray spectroscopy (EDS). Results are shown in Table 5.2. Samples were either adhered to a conductive carbon tape or dispersed from solution onto a Si wafer and then measured using a JEOL 6340F FESEM equipped with EDAX EDS at 20 kV and

12 μA settings. The spectrum was measured for a sufficient amount of time to obtain 10,000 counts in the 6.4 keV bin, which corresponds to the primary Fe K_α peak (generally 15-25 minutes). Each sample was measured at a minimum of three different points and the compositions of the different locations averaged. The standard deviation between the points was taken as the error in the measurement.

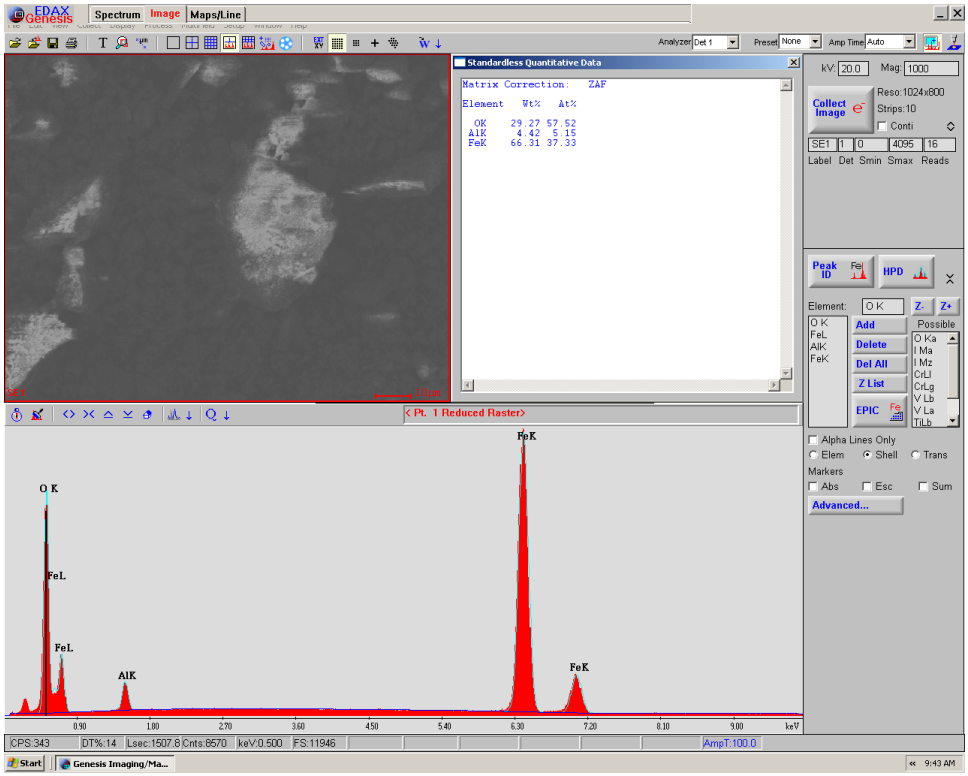


Figure 5.4: Example EDS measurement of nanoparticulate ferrihydrite batch 8.

Because there are sometimes other elements measured, the Fe:O ratio is a more consistent way of looking at how well the ferrihydrite matches the expected formula. However, there is evidence to suggest that dehydration occurs over the course of measurement (the samples are under vacuum and will be heated by the electron beam), which could easily change the Fe:O ratio. Therefore, these data should be considered with this in mind. Overall, the nanoparticulate ferrihydrite matches relatively well with the expected Fe:O ratio of 0.625, but seems to increase to near 1 for some measurements, which may be a function of the measurement conditions. Unfortunately, EDS measurements were not made on all batches when they were fresh, and due to low count rates, some samples had to be measured for extended periods of time to obtain good counting statistics.

The mesoporous ferrihydrite showed a large variability in the amount of silica remaining on the surface of the pores following etching away of the KIT-6 template with NaOH (as described in Section 5.3.2). Most measurements were around 2 %, but they ranged up to 17 %. These data show the uneven removal of the template for some sections of sample. Additionally, it should be noted that the silicon is in the form of silica (SiO_2), and is present only on the surface of the pores. Therefore, the surface concentration of the silica is greater

Material	Fe:O	Avg. Si	Impurities (%)	Age
Batch 2 (4)	0.7 (0.3)	0.16 (0.04)	-	27 Months
Batch 3 (4)	0.6 (0.1)	0.17 (0.08)	-	20 Months
Batch 5 (3)	0.70 (0.04)	0.12 (0.03)	-	15 Months
Batch 6 (3)	0.71 (0.07)	0.12 (0.03)	-	13 Months
Batch 7 (1)	0.4 (-)	0.16 (0.0)	-	9 Weeks
Batch 7 (3)	1.5 (0.4)	0.07 (0.04)	Na (0.02)	9 Months
Batch 8 (2)	0.655 (0.009)	0.0 (0.0)	-	6 Weeks
Batch 8 (3)	1.3 (0.3)	0.07 (0.02)	Na (0.04)	4 Months
Batch 8 (4)	0.6 (0.2)	-	-	6 Months
Mesoporous HT2 (7)	1.2 (0.8)	4 (6)	Na (1.6)	3, 6, 10 Months

Table 5.2: Atomic percent ratios and standard deviations of Fe, O, and Si in ferrihydrite batches as measured by SEM-EDAX. For all reported numbers the standard deviation is in parentheses following the value. The standard deviations of secondary elements are not reported, and Al, C, and Cu were not reported as they were from the measurement substrate.

than the percentage when averaged over the mass of the entire particle.

Only a few samples showed the presence of sodium, which would indicate insufficient washing or dialysis. The sodium content only seemed to be significant for the mesoporous ferrihydrite, which was the only material not to undergo dialysis. However, even this was not a significantly large enough amount to suggest that the Na would greatly affect the material, particularly because $NaClO_4$ is used as a background electrolyte in all solution-based experiments. Other than sodium and silicon, no elemental impurities were measured for any of the materials, at least to the detection limits of the EDAX system.

5.5 Particle Size and Morphology

The size of particles can be determined by SEM and transmission electron microscopy (TEM). SEM was described in Section 4.3.2. TEM is an imaging technique that can achieve Å resolution. It functions similar to an optical microscope, but uses an electron beam. The beam is focused and then passes through the sample. Dense materials scatter the electrons, but less dense materials will allow the electrons to pass through to a phosphor screen that registers a shadow image indicative of density. [92] Samples must be very thin, and are then mounted on a conductive grid and measured under vacuum.

For TEM measurements of suspended ferrihydrite, a drop of dilute suspension in at pH 4.5 at low ionic strength was placed onto the TEM grid and allowed to dry. The suspension was kept dilute to attempt to reduce the amount of aggregation possible upon drying and to increase the chances of finding isolated particles. For SEM measurements samples were resuspended in Milli-Q water and allowed to dry to a conductive Si wafer.

SEM and TEM images of ferrihydrite show a wide range of particle sizes with some surface roughness. Representative SEM and TEM images are shown in Figures 5.5 and 5.3. At the

smallest, suspended ferrihydrite particles appear to be just under 2 nm in size, increasing to around 5 nm for the aged "ferri-goethite" (not shown). Note that these measurements were made using the ruler feature in the software marked by eye, and thus are not exact measurements. Once dried, the majority of particles seem to fall within two size ranges: 10-50 μm and 20-1000 nm. The largest aggregated particles are shown by SEM to be up to 100 μm, and are of irregular shape with a non-uniform surface (Figure 5.6). This is consistent with past work [39].

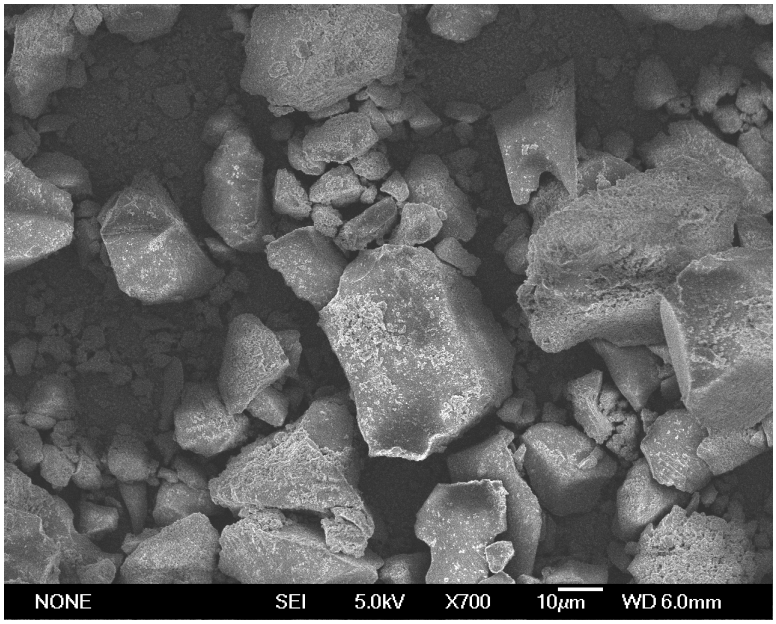


Figure 5.5: SEM image of dried ferrihydrite batch 8 showing the wide range of particle sizes.

SEM images of mesoporous ferrihydrite also show a wide distribution of particle sizes, ranging from 100 nm to 200 μm, with most particles being between 1 and 10 μm (Figure 5.7). High resolution TEM images (Figure 5.8) show the distinctive lattice fringes that suggest a more crystalline structure. However, these fringes were also seen for 2-line ferrihydrite particles by Smith *et al.* (2012) [139], so they are not unexpected.

5.6 X-ray Diffraction

The X-ray diffractograms of both nanoparticulate (Figure 5.9) and mesoporous (Figure 5.10) ferrihydrite were measured with a PANalytical X-Pert Pro powder X-ray diffractometer using Co Kα radiation passed through an iron filter. Samples were pressed onto a zero background plate and measured over 2θ angles of 15 to 100 degrees. 12 scans of two hours each (using a step size of 0.0042 and 45 seconds per step) were averaged for the final diffractogram. For a description of XRD, see Section 4.3.1.

Both diffractograms show the characteristic two broad reflections for 2-line ferrihydrite [26]. As the nanoparticulate ferrihydrite ages, it begins to show the peaks of both goethite and hematite (more so hematite from heating, dry conditions, or neutral pH conditions and

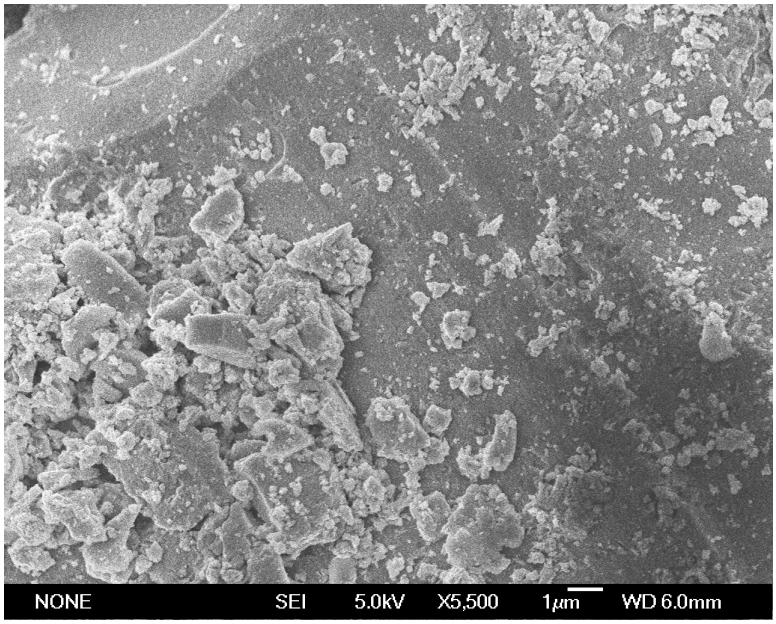


Figure 5.6: SEM image of dried ferrihydrite batch 8 showing the surface roughness of particles.

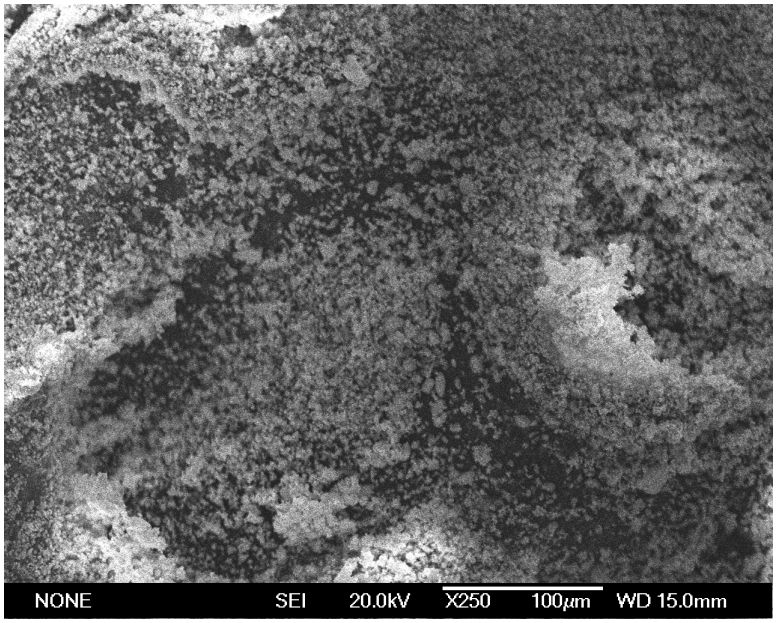


Figure 5.7: SEM image of mesoporous ferrihydrite showing the range of particle sizes.

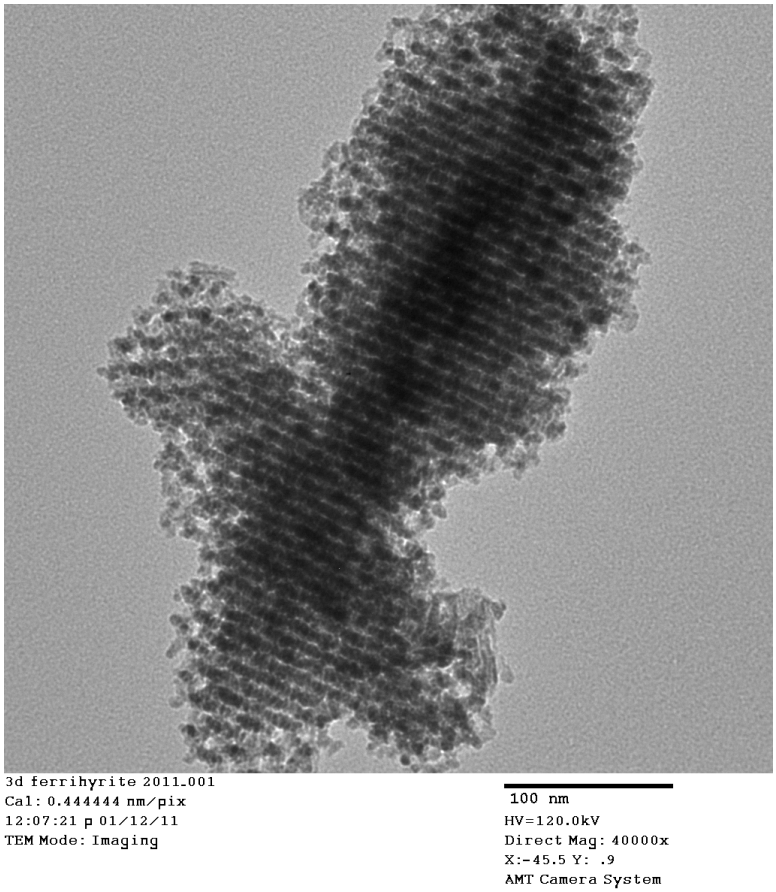


Figure 5.8: HR-TEM image of mesoporous ferrihydrite showing the mesoporous nature of the material. From H. Tüysüz.

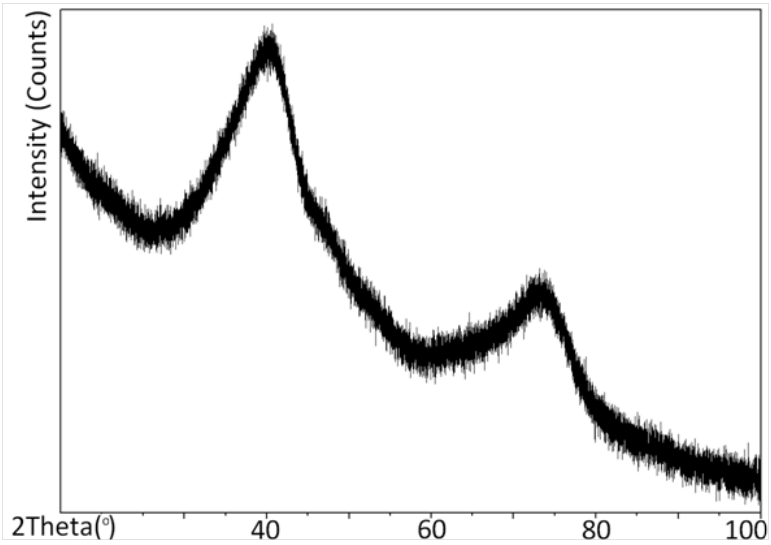


Figure 5.9: X-ray diffractogram for 2-line ferrihydrite showing only two broad reflections.

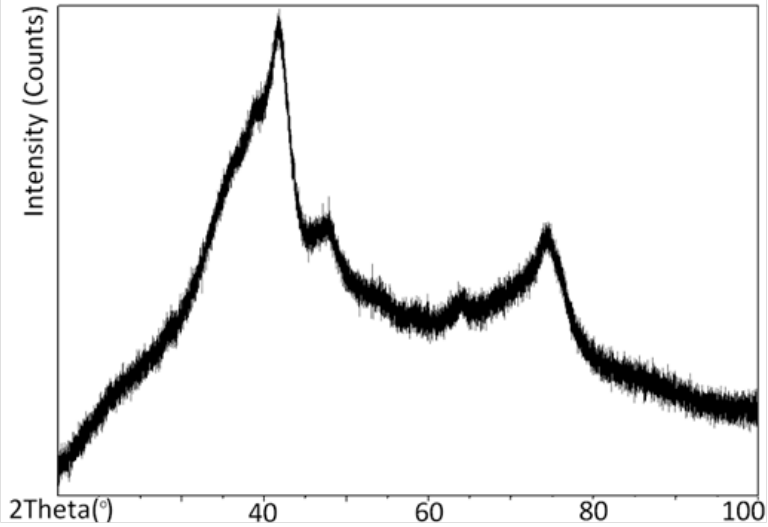


Figure 5.10: X-ray diffractogram for 3D mesoporous 2-line ferrihydrite showing two broad reflections and the starts of some more crystalline peaks corresponding to hematite or 6-line ferrihydrite.

goethite in suspensions, particularly at high or low pH [127, 161]), as shown in Figure 5.12. The speed of this aging is cited to be on the order of weeks [39, 126], but the synthesis outlined in this work produced ferrihydrite that was stable for at least 5.5 months when dried (Figure 5.11). The suspensions all aged to have a large goethite contribution ("ferrigoethite") (not shown). The mesoporous ferrihydrite begins to show these hematite peaks, which also correspond to the peaks found in 6-line ferrihydrite, much more readily in a normal synthesis because it is so difficult to reach exactly the temperature and heating conditions necessary for pure ferrihydrite (see Section 5.3.2). However, in the material used for these experiments, the contribution from this more crystalline phase was small, as shown in Figure 5.10.

5.7 Surface Area Measurements

5.7.1 Introduction

There are several ways to measure the surface area of solids, many of which involve the measurement of the amount of a particular molecule adsorbed to the particle surface, but none of which provide the absolute value of the surface area [74]. The current primary method of measurement is the Brunauer-Emmett-Teller (BET) nitrogen adsorption method [11]. This method measures the surface area based on the amount of nitrogen gas adsorbed to the surface at 77 K and the area taken up by a N_2 molecule when adsorbed to the surface. However, N_2 is not the only molecule used for surface area measurements. The BET method can also be performed with other gases, such as argon, water, carbon monoxide, benzene, and ammonia [35]. Other methods use the reversible sorption of metal cations [39] or ethylene glycol monoether (EGME) [178]. The surface area can also be measured in solution by the

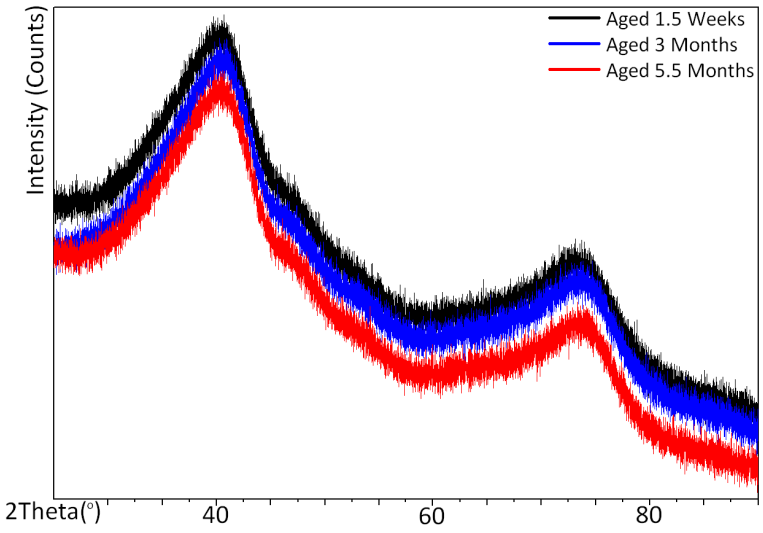


Figure 5.11: X-ray diffractogram for batch 8 showing stability as 2-line ferrihydrite for up to 5.5 months with no visible more crystalline peaks.

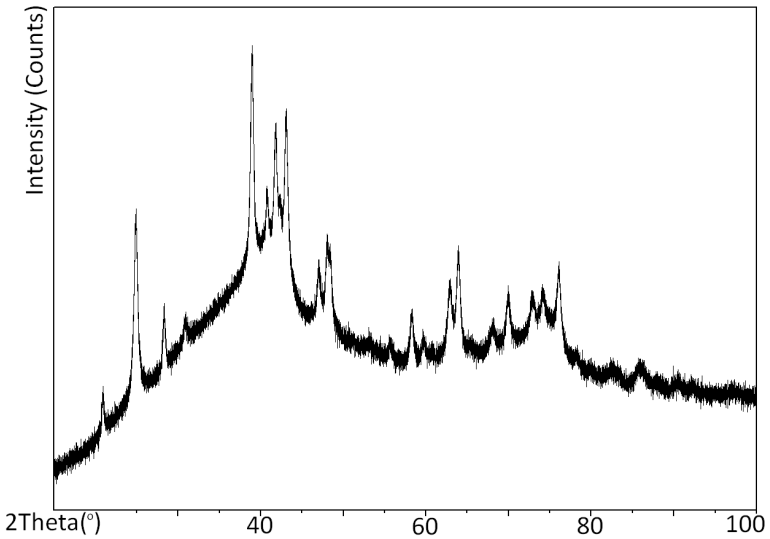


Figure 5.12: X-ray diffractogram for 2-line ferrihydrite showing two broad reflections as well as the more crystalline peaks of goethite and hematite.

adsorption of dyes, such as methylene blue [54, 55, 68, 72, 179]. Ideally, the method chosen assesses the surface area under conditions most similar to the application of the material [74], but this is not always possible.

Two techniques were used for the measurement of the surface area of ferrihydrite: N_2 adsorption and methylene blue adsorption. However, the particle sizes were discovered to be too small for methylene blue adsorption, as discussed in Section 5.7.7, so only N_2 adsorption data was usable. BET surface area data are presented in Section 5.7.4.

5.7.2 BET Surface Area Measurements

Nitrogen adsorption is conducted on dry powders, which are first outgassed to remove any physisorbed species and clear the pores for nitrogen adsorption. During outgassing the sample is put under high vacuum and heated to the maximum temperature achievable before surface or structural transformations occur. 120-150 °C is common for many oxides, but Weidler (1997) [172] showed that excess humidity around a ferrihydrite sample can cause structural transformation between 120 and 130 °C, so outgassing at 120 °C could potentially cause transformations. All of the outgassing on nanoparticulate ferrihydrite was performed at 110 °C in case there was some residual humidity during outgassing. The mass obtained for the sample after outgassing was taken as the measurement sample mass. Care was also taken to expose the sample to as little atmosphere as possible between outgassing and measurement to prevent re-adsorption of any species to the surface. Additionally, acetone is commonly used to dry ferrihydrite from solution. However, Weidler [172] demonstrates that acetone can block ferrihydrite pores, drastically reducing the surface area. Most of the acetone can be removed by heating at 50 °C, but much higher temperatures are necessary to remove all of it, and these higher temperatures may cause structural changes. It is therefore recommended that acetone not be used to dry ferrihydrite.

The theory behind the measurement of surface area by BET requires some discussion of the material itself. The fine particles of powders, known as primary particles, will naturally tend to aggregate to form secondary particles. In many cases this is mere particle adhesion, but can also occur through adsorbed water, forming much stronger aggregates sometimes called agglomerates. [49, 74] This is the case for ferrihydrite, other ferric oxides, and other xerogels. The surface area then reflects the particle aggregation, with the surface area of the aggregates being less than the non-aggregated particles by the area contained within the junction points between particles. The aggregation also causes pore channels to form between particles, giving the solid a measurable pore volume, as well as the differentiation between internal and external surface area. The size of these pores are related to the original particle size and shape. [49] As mentioned in Section 5.2, ferrihydrite forms spherical particles, so pores will be expected to resemble those shown in Figure 5.13. Pores with an average width less than 20 Å are classified as micropores, while pores 20-500 Å are mesopores, and greater than 500 Å are macropores. [49, 74]

When a solid powder is exposed to gas with a measurable pressure in a closed container, the solid will begin to adsorb the gas to the surface. The amount of gas adsorbed can be measured by the reduction in the pressure of the gas (or the increase in the mass of the sample, although this is more difficult) provided the volume of both the sample and the container are known. The adsorption of the gas to the surface is caused by physisorption

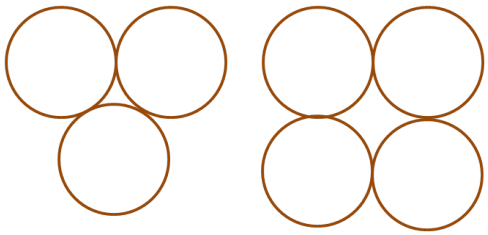


Figure 5.13: Example pore shapes caused by the aggregation of same-sized spheres.

(involving only weak intermolecular forces such as van der Waals interactions or hydrogen bonding) or chemisorption (chemical adsorption where there is an actual chemical bond between the interacting species). [49, 74] The Brunauer-Emmett-Teller, or BET, method of surface area measurement with N_2 is based on van der Waals attraction mechanisms. When chemisorption is involved then the Langmuir equation is more appropriate. [35] Van der Waals forces are attractive forces caused by polarization of molecules, molecules that already possess dipoles, and non-polar dispersion forces. In general, the BET equation applies when neutral atoms or molecules interact with surfaces when electrons are not shared or exchanged, and is an extension of the monolayer Langmuir equation to multilayer sorption. [35] The BET equation is:

$$V = \frac{V_m C P}{(P_0 - P)[1 + (C-1)P/P_0]} \tag{5.1}$$

where P is the pressure, P_0 is the saturation pressure of the adsorbate, V is the volume of the adsorbate, V_m is the volume of adsorbate corresponding to one monolayer, and C is a constant given by

$$C = e^{(E_1 - E_L)/RT} \tag{5.2}$$

where E_1 is the average heat of adsorption in the first monolayer, E_L is the heat of liquefaction, R is the gas constant, and T is the temperature. [11, 35] This equation is valid between P/P_0 values of 0.05-0.35. [35] Above this level capillary condensation, or the presence of a condensate separated from the gas phase in the pore space, takes effect. [74]

Plotting $1/(V((P/P_0) - 1))$ versus P/P_0 should give a straight line whose slope is $(C - 1)/V_m C$ and whose intercept is $1/V_m C$ [11]. Solving for C and V_m gives the relations $C = 1 + (Slope/Intercept)$ and $V_m = 1/(Slope + Intercept)$. For a valid determination of surface area, C should have a value greater than 20 [74, 135]. V_m can then be used to solve for the surface area using the equation

$$SA_{BET} = a n_m N = a(V_m/22414)N \tag{5.3}$$

where a is the surface coverage of one adsorbate molecule, n_m is the molar monolayer capacity, 22414 cm^3/mole is the molar volume of an ideal gas, and N is Avogadro's number. [66] Although numbers ranging from 13.5 to 16.8 $Å^2$ are used, the generally accepted surface coverage of one N_2 molecule is 16.2 $Å^2$. The specific surface area is then calculated by dividing the total surface area by the mass of the sample. These calculations can also be made specific before carrying out the BET equation, as is done by the Autosorb-1 software

used for this work. In that case the volume is replaced with the specific weight of nitrogen, W, meaning that the volume of nitrogen added is divided by 22414 cm^3/mole, multiplied by the molecular weight of N_2 of 28.0134 g/mole, and then divided by the mass of the sample. Either of these two calculation routes yields the same answer, so which is employed is simply a matter of personal preference.

The relationship between amount of a given gas adsorbed onto a given solid and the pressure at a fixed temperature is known as an adsorption isotherm [49]. There are six common types or shapes of isotherms, shown in Figure 5.14, some of which are characterized by hysteresis loops where the adsorption and desorption curves do not coincide [74]. It should be noted, however, that these are generalized curves, and measured isotherms may differ somewhat from these exact shapes. For example, it is common for there to be a final upward turn at high pressures nearing the saturation pressure, or for isotherms to have characteristics belonging to more than one isotherm type [49]. A full description of the types of isotherms will not be presented here other than to mention that Type I isotherms tend to be for microporous solids and Type IV isotherms tend to be for mesoporous solids. There are also four different types of hysteresis, shown in Figure 5.15. Type H1 loops are often associated with porous materials formed from agglomerates with narrow pore size distributions, Type H4 loops are often associated with narrow slit-like pores or microporosity if a Type I isotherm. Type H2 loops are difficult to interpret but suggest an ill-defined pore size distribution and pore shape, while Type H3 loops indicate aggregates of plate-like particles. [135]

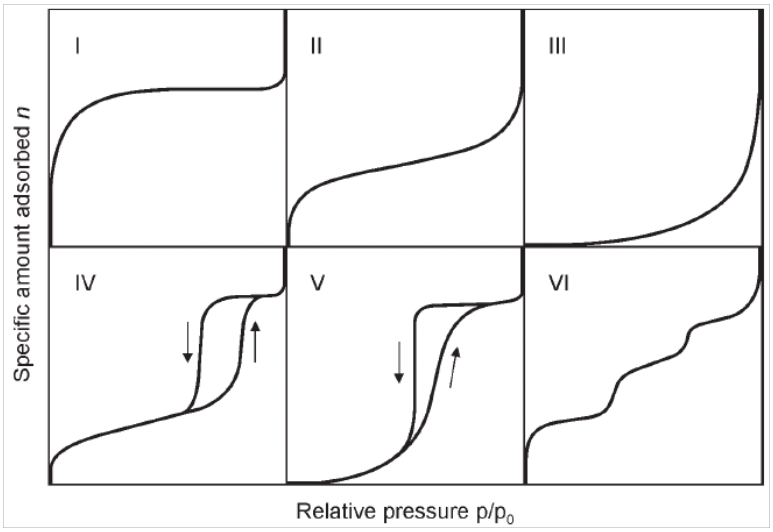


Figure 5.14: Shapes of the six common types of adsorption isotherms. From Klobes *et al.* (2006) [74].

The aim of the BET method is to find the point at which the slope of the isotherm reduces drastically at a relatively sharp corner, indicating the sorption of a monolayer of adsorbate. Once the volume of this adsorbate is known, it can be converted to surface area if the area and orientation of the adsorbate molecule are known. For N_2 this area is generally taken to be 16.2 $Å^2$, which is the area in liquid nitrogen because measurements are usually

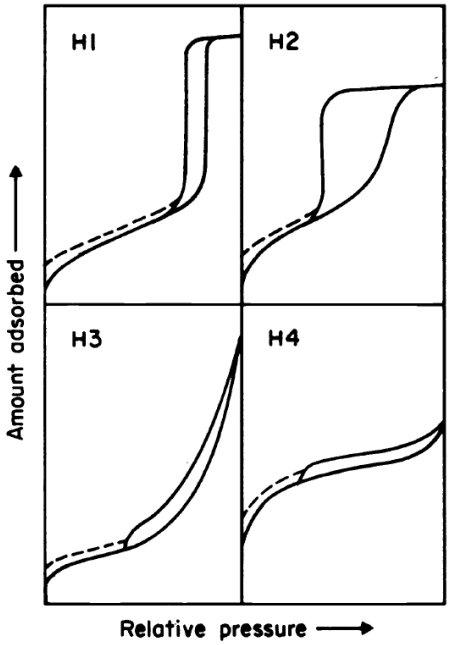


Figure 5.15: Shapes of the four common types of hysteresis found in adsorption isotherms. From Sing *et al.* (1985) [135].

performed at 77 K. However, this value may change as a function of the surface. [35]

The external surface area is generally taken to include any surface features that protrude from the surface as well as any depressions that are wider than they are deep. The internal surface area then consists of the area of any cavities, cracks, or pores that are deeper than they are wide. The measurable internal surface area is limited by the size of the adsorbate; the adsorbate must be able to reach the surface in question for its area to be measured, so closed pores and pores smaller than the adsorbate size are not measurable. For nitrogen, the minimum pore size able to be investigated is approximately 4 Å.[74]

The nitrogen adsorption data taken using the BET method can also be analyzed using several other techniques for comparison. These techniques include the Langmuir equation, the t-method of de Boer, the Barrett-Joyner-Halenda (BJH) method, and the Dollimore-Heal (DH) method. There are times when the pores of the solid are so small, such as is the case for ferrihydrite, that the normal BET plot may not give correct results. In these cases, use of the t-method is useful. A t-plot will not cross through the origin. Instead taking the slope of the line drawn between the first data point and the origin will give a lower bound for the surface area. [36]

For the t-method of determining surface area the specific surface area S is calculated from the statistical thickness t of the adsorbed layer of nitrogen and the specific volume of nitrogen V adsorbed according to the relationship

$$S = 15.47V/t \tag{5.4}$$

for the region of the plot that is linear. t can be calculated from the relative pressure using

the empirical equation

$$log(p/p_0) = 0.034 - 13.99/t^2. \tag{5.5}$$

Once the experimental curve of V versus t deviates from a straight line, this indicates that more nitrogen is being taken up than one would expect from simple multimolecular adsorption. This is the point at which capillary condensation inside the pores of the solid takes place. Once a new straight line with a different slope is established, this indicates that the pores are filled and multimolecular adsorption is again dominating. The slope of this new region will give the external surface area of the solid. The internal surface area can be calculated by subtracting the external surface area from the total specific surface area calculated from the initial slope. [36, 84, 85]

5.7.3 Problems with BET Measurements

The BET method has several requirements that tend to cause the underestimation of surface area in many materials. [168, 179] The solid must be put under high vacuum, which can collapse sheet-like or micropore structures, causing the measurement to be external surface area only and thereby decreasing the effective surface area. The solid must also be dried, which, in the case of small particles and colloids, can cause particle aggregation and thus a decrease in the surface area. This is most certainly the case for ferrihydrite and prevents the measurement of the suspended ferrihydrite. The BET method also puts the solid through drastic temperature changes, which can alter the surface properties of the solid. [46] Additionally, very cold temperatures can cause extremely slow diffusion into pores for microporous solids, limiting the nitrogen that reaches the inner pore surfaces during the course of the measurement. The surface area measurement can also change depending on the surface affinity for N_2 and the pore size in comparison with N_2. Hydrated metal cations may not fit into the same pores as N_2 would [55]. Finally, BET is a gas phase, not a solution phase, measurement, and therefore is not an accurate representation of the surface area in solution. Despite these problems, BET nitrogen adsorption is the most reliable method to at least get an estimate of the surface area for ferrihydrite, and the data presented in Section 5.7.4 must be considered with these limitations in mind.

There are also problems associated with the analysis. While BET measurements are widely used, it is also widely accepted that the analysis methods are semi-empirical and often very large simplifications of complex processes. The greater the difference between the ideal solid assumed and the actual solid, the further off the calculations will be. For example, pore volume and pore size distributions are calculated using BET surface area under the assumption that pores are somewhat uniform. The presence of micropores and surface roughness will greatly increase the surface area without greatly changing the pore volume. This can be corrected for, but it requires careful use of standard reference materials. [88] It should be made clear that none of the measurements presented in this chapter were made against a standard reference material. While the surface areas calculated seem to be what was expected based on knowledge of the properties the materials should have, they cannot be confirmed as entirely correct based on comparison to a standard. However, this lack of standard is not expected to affect the specific surface area values greatly, but may

Material	BET Surface Area	Age
Batch 1	258.8	21 Months
Batch 3	301.0	10 Months
Batch 5	308.5	10 Months
Batch 6	332.1	61 Days
Batch 7	353.4	57 Days
Batch 8	325.2	6 Months
Mesoporous HT2	190.5	n/a
Mesoporous LKSB1	215.1	n/a
Mesoporous LKSB4	138.3	n/a

Table 5.3: Surface area values for ferrihydrite batches using nitrogen adsorption data using the BET method.

affect the pore characteristics considerably. The pore characteristics should therefore be taken with a healthy dose of uncertainty.

5.7.4 BET Surface Area Data

Many previous measurements of the surface area of ferrihydrite have been made using several techniques, the most common of which is BET nitrogen adsorption. Dzombak and Morel and Cornell and Schwertmann [26, 39] list a series of these measurements, with the caveat that the reproducibility of BET measurements with porous solids like ferrihydrite is generally low and that most experimental errors will cause the underestimation of the surface area. The average of these measurements was 318 m^2/g with a standard deviation of 150 for all methods and 245 m^2/g with a standard deviation of 57 for nitrogen BET measurements. However, it is unclear if all measurements are for 2-line ferrihydrite, but the large standard deviations show the great variability in measured surface area. This is not surprising considering the limitations of the various methods as well as preparation and measurement differences such as precipitation pH, presence of acetone for drying, method of drying (freeze- or air-drying), grinding technique, and outgassing temperature.

The materials used during the course of this work were measured by BET nitrogen adsorption using an Quantachrome Autosorb-1. The calculated surface area values are given in Table 5.3. These data show a clear dependence of the surface area on the age of the dried ferrihydrite. This is not surprising given that the ferrihydrite will continue to aggregate and crystallize over time, reducing the surface area [94]. Based on this knowledge, a surface area of 350 is the most accurate because it reflects the measurement made closest to the synthesis of the batch. However, it is reasonable to assume that the actual surface area of the dried ferrihydrite is between 300 and 450 m^2/g based on the measured values, the variability between ferrihydrite batches, and the knowledge that this is likely an underestimate of the actual surface area due to the high level of microporosity that is not able to be measured. These values are in good agreement with the literature [46].

Davis (1977) (in [39]) calculated the ferrihydrite surface area to be 840 m^2/g assuming

spherical particles 2 nm in diameter and a density of 3.57 g/cm^3. As shown in Section 5.5, 2 nm is a good particle size estimate for the ferrihydrite used in this work. Although the density was not measured, it is reasonable to expect that the surface area of the suspended ferrihydrite is near 800 m^2/g assuming some loss of surface area due to minor aggregation.

The surface area of the mesoporous ferrihydrite was only measured with BET nitrogen adsorption as the mesostructure was not expected to collapse due to BET measurement conditions. Tüysüz *et al.* measured the surface area to be 222 m^2/g [164]. The measurements of the materials used in the course of this work were less, with a range of 170 to 211 m^2/g, with an average of 191 m^2/g (see Table 5.3). While these values may seem low for a mesoporous material, it must be remembered that the values are reported per gram. Many common mesoporous materials, such as mesoporous silica or carbon, are much lighter and therefore have a larger surface area per gram than the heavier iron oxide presented here.

5.7.5 Pore Size and Volume Measurements

Because dried ferrihydrite is made up of aggregated nanoparticles, it is by nature microporous [26]. Ideally Ar would be used for micropore analysis because nitrogen will more strongly interact with the pore surface causing micropore filling at lower P/P_0 values [50], but nitrogen will suffice and is better for mesopore analysis. The isotherms vary by batch but resemble mostly Type I isotherms, sometimes with hysteresis loops (see Figures 5.16 and 5.17. This is consistent with a microporous solid [74] as the relatively flat shape over a wide range of pressures indicates a small amount of multilayer adsorption onto a small external surface area [134]. Additionally, inspection of the hysteresis shows primarily Type H4 loops, which are consistent with a microporous solid [135]. Cornell and Schwertmann [26] suggest that ferrihydrite will form a mesoporous material exhibiting a Type IV isotherm, but this transformation was not observed in the course of this work. The pore volume calculated for dried ferrihydrite averaged around 0.2 cm^3/g, and the average pore size distribution was centered just above 2 nm.

Mesoporous ferrihydrite should exhibit a type IV isotherm. Figure 5.18 shows that this is indeed the case. The hysteresis is of Type H3, suggesting slit-shape pores, although TEM images (see Figure 5.8) suggest otherwise. The original authors found a pore volume of 0.54 cm^3/g with the peak of the pore size distribution centered at 5.1 nm [164]. The measurements made here found an average pore volume of 0.40 cm^3/g with a bimodal pore size distribution with peaks around 2.9 nm and 9.5 nm.

Calculations can be made for the pore volume and pore size distribution using several different methods. These include the BJH method, t-method for micropore volume, Horvath-Kawazoe (HK) method for slit-shaped pores, Dubinin-Radushkevich (DR) method, and the Saito-Foley (SF) method for cylindrical pores. The pore size distribution is generally calculated using methods based on the Kelvin equation in the form

$$\frac{1}{r_1} + \frac{1}{r_2} = -\frac{RT}{v\sigma} ln(\frac{P}{P_0}) \tag{5.6}$$

where r_1 and r_2 are the principle radii of curvature of the liquid meniscus in the pore, σ is the surface tension of the liquid (8.85 erg/cm^2 for N_2), v is the molar volume (34.67 mL/mole for N_2), and R and T have their usual meanings. Rearranging the Kelvin equation and replacing

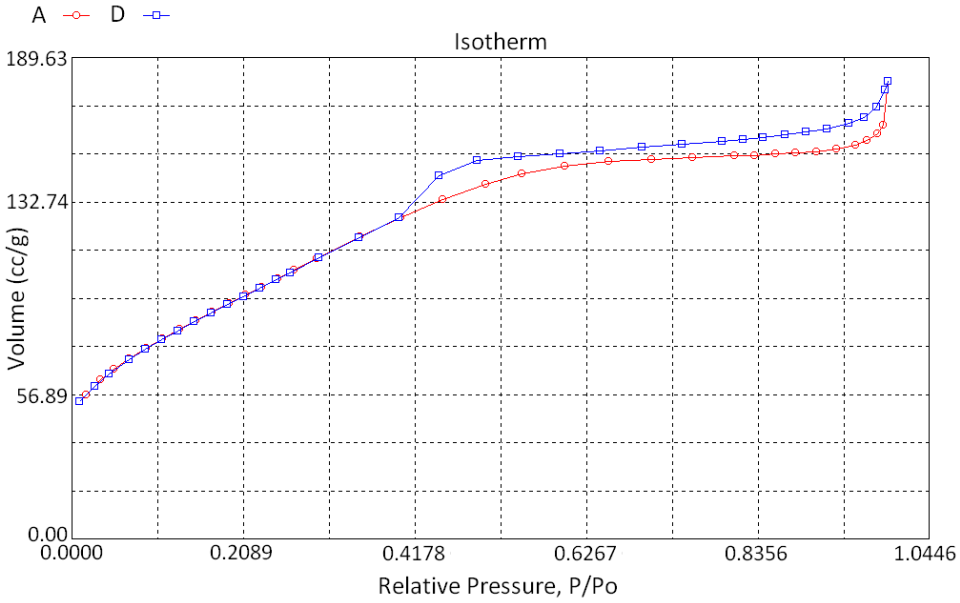


Figure 5.16: Representative dried ferrihydrite isotherm for those samples with hysteresis.

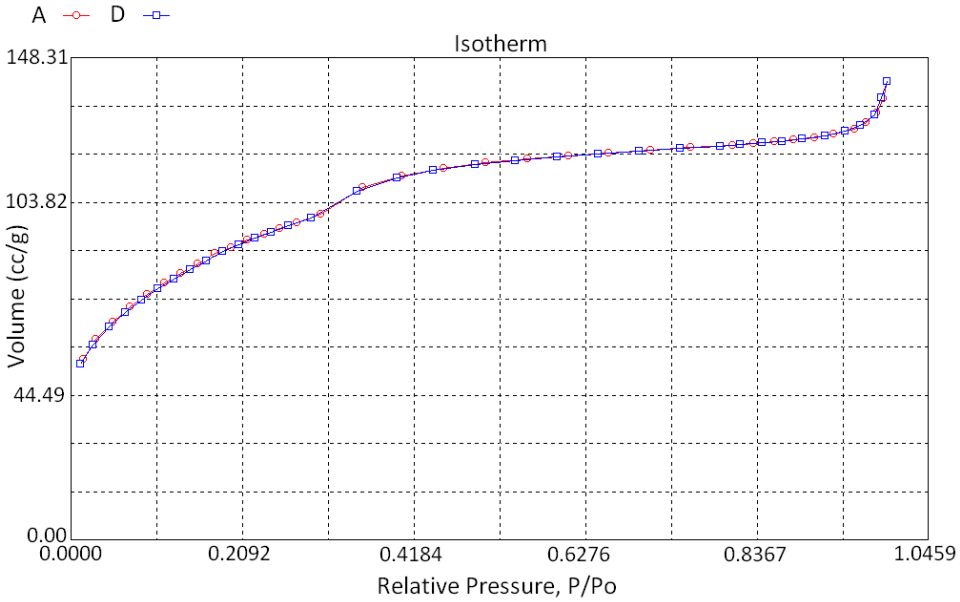


Figure 5.17: Representative dried ferrihydrite isotherm for those samples without hysteresis.

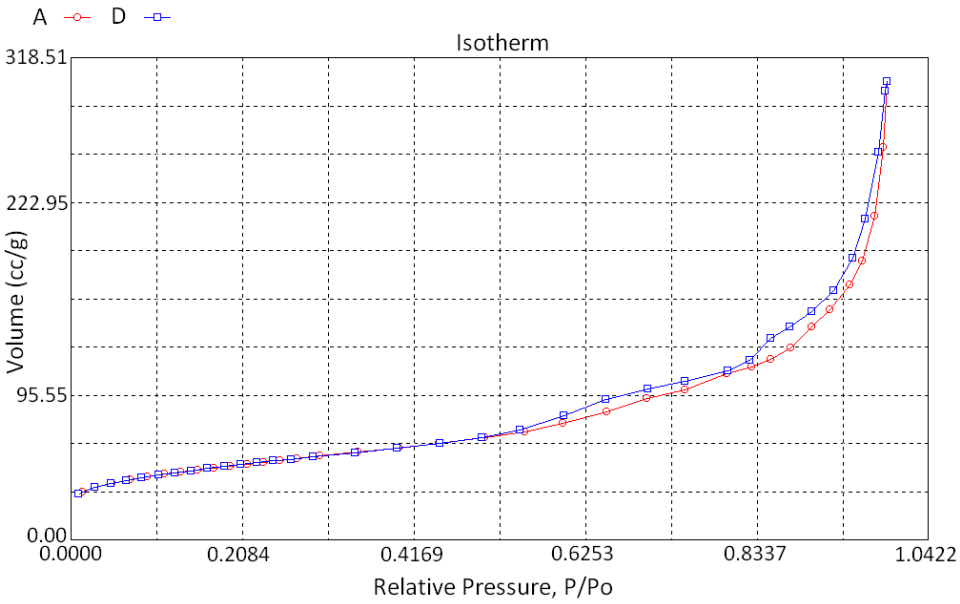


Figure 5.18: Representative mesoporous ferrihydrite isotherm.

$\frac{1}{r_1} + \frac{1}{r_2}$ with $\frac{2}{r_K}$ where r_K is the Kelvin radius (the radius of the inner pore cylinder filled by capillary condensation) gives

$$r_K = -\frac{2v\sigma}{RTln(\frac{P}{P_0})} \tag{5.7}$$

Because the pore shape is not known, it is generally assumed to be either cylindrical or slit-shaped. [135] This assumption may be completely invalid but must be made without exact knowledge of the pore shape and the introduction of an overly complex model. If the pores are assumed to by cylindrical, then the radius r_P must be corrected for the thickness of the layer already adsorbed to the pore wall before capillary condensation occurred, which is the thickness t discussed above. r_P is then equal to $r_K + t$. For a slit-shaped pore the width d_P of the shorter dimension is considered rather than the radius, and because there are now two sides in consideration, d_P is equal to $r_K + 2t$. [135]

The total pore volume is calculated from the amount of nitrogen adsorbed near the saturation pressure, assuming that all of the pores are filled by this point [135].

The question sometimes arises as to whether pore size distribution calculations should be performed on the adsorption or the desorption branch of the isotherm. Groen *et al.* (2003) [50] explains that for systems with an interconnected pore system, particularly with pores of varying size, the adsorption branch is greatly preferred. The desorption branch will experience forced closure of the hysteresis loop at around $P/P_0 = 0.45$ for nitrogen isotherms due to tensile strength effects (TSE), such as is seen in Figure 5.16. The sudden drop in the volume contained in the pores that causes this closure is due to an instability in the spherical meniscus during desorption from pores approximately 4 nm in diameter. This effect can be increased when larger interconnected pores must empty through smaller pores, and will result in the desorption branch showing a shift to lower pore size. Additionally,

Groen *et al.* [50] warns of a false peak in the desorption pore size distribution plot at around 4 nm caused by the TSE phenomenon. This peak should only be taken as a real pore size measurement if it appears in both the adsorption and desorption branches. It is therefore wise to compare both branches, but look to the adsorption branch for a more reliable pore distribution. However, comparison of the two can lead to a better understanding of the size, shape, and interconnectedness of the pores of the material.

5.7.6 Problems with Pore Analysis Calculations

Despite its wide use, the classical BJH model significantly underestimates the pore size because it fails to take into account the effect of the curvature of the pore walls on the adsorbed layer thickness [50, 88]. A more correct although much less widely used method is the Broekhoff and de Boer method that takes this curvature into account, particularly when the Frenkel-Halsey-Hill version of the isotherm is employed [88]. Because the aim of this work relies much more heavily on the value obtained for the surface area than it does on the pore volume or pore size distribution, the simple BJH calculations presented here were found to be sufficient as they give at least a rough idea of the pore size range to inform the understanding of the surface structure. The surface area is extremely pertinent for sorption experiments, and because the synthesis of ferrihydrite was not intended to produce a particular pore size, it is not pertinent that the exact pore size be known. Although the mesoporous ferrihydrite synthesis was intended to create a particular pore size, the pores should be cylindrical in nature, increasing the applicability of simpler models. Additionally, the pore structure is still not of great importance for understanding plutonium sorption as long as diffusion is not an issue (which it is not; see Section 5.9.2).

5.7.7 Methylene Blue Surface Area Measurements

The methylene blue test has been widely used for clays and clayey soils for measuring specific surface area, cation exchange capacity, swell potential, and other properties. [68, 179] Several authors have determined that methylene blue has the greatest tendency of all dyes to adsorb, and that only a single layer of methylene blue adsorbs to the surface (listed in Darr and Ludwig 1973 [32]). The latter point was disputed by Harris and Knobbe (1996) [55], but most authors agree on monolayer coverage. There is, however, a change in the methylene blue adsorption based on certain parameters, such as the pH of the solution [68], the particular material used (in [32]), dispersion [68], and others. Thus, this technique still does not give the total surface area under all conditions. It does, however, give the effective active surface area for particular solution conditions (pH, ionic strength, temperature, etc.) without submitting the solid to vacuum, drying, or extreme temperatures. These factors make this technique ideal for clayey soils, finely-structured materials, and solids in suspension.

The methylene blue dye is a cationic molecule (see Figure 5.19) shaped like a rectangular plate that is 17.0 × 7.6 × 3.25 Å[54], which gives a projected area of 135 Å, 132 Å, or 130 Å [32, 179]. It was found for both non-graphitized carbon black and positively charged mercury surfaces that it covers 2.44 m^2/mg [32]. Drying the dye at 105 °C to constant weight will achieve the anhydrous state to accurately add the dye by mass [179].

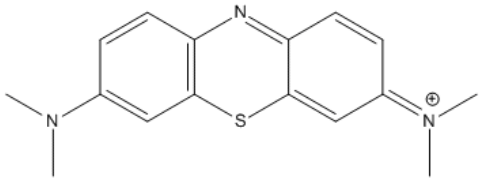


Figure 5.19: Structure of the methylene blue molecule.

Methylene blue adsorbs to the surface through cation replacement or chemisorption to a negative surface. The cation exchange efficiency unfortunately differs as a function of the cation. Full replacement is generally reported for only Li^+ and Na^+ exchanged soil surfaces. However, for measurements of surface area, Yukselen and Kaya (2008) [179] observed no difference between natural and Na-exchanged soils. No prior special treatment should be required before contact with methylene blue for accurate measurements.

There are several ways to measure the methylene blue concentration in solution. The most straightforward is to measure it photometrically using the maximum absorption peak of 665 nm, 666 nm [52], or 625 nm [55] with a UV-visible spectrophotometer. A calibration curve of solutions with a known concentration of methylene blue is made, and then used to calculate the concentration in the sample solutions. Solutions at the desired pH, ionic strength, temperature, and amount of solid are prepared, and increasing amounts of methylene blue are added. These solutions are mixed on a rocker or shaker until equilibrium has been reached (24 hours according to Wall *et al.* 2010 [168], 1 hour according to Gurses *et al.* 2006 [52], 2 hours according to Ma *et al.* 2004 [89]). The solutions are then allowed to settle or are centrifuged to remove the solid, and the solution methylene blue concentration is measured. [8, 179] If the solutions are in the appropriate range for Beer's law, then the amount D of dye adsorbed is given by

$$D = \frac{A_0 - A_1}{\epsilon} \cdot \frac{v}{g}(mol/g) \tag{5.8}$$

where A_0 and A_1 are the initial and final absorbance of the solution, respectively, ϵ is the molar absorptivity, and v is the volume of the solution in liters in equilibrium with the mass g of the solid in grams. [8] A plot of the adsorbed dye versus the amount of dye added will show an initial increase that eventually plateaus. Although Wall *et al.* (2010) [168], Gurses *et al.* (2006) [52], and Harris and Knobbe (1996) [55] all cited that the plateau indicated the amount of methylene blue to determine the surface area, other authors [179] list the point at which the curve deviates from the initial 45° line as the end point. When the curve begins to deviate, this indicates that the added methylene blue can no longer be adsorbed completely, meaning that the surface has been fully covered. The plateau of this plot is generally referred to as the cation exchange capacity (CEC), and may represent more than a monolayer of binding. Gurses *et al.* (2006) [52] also reported that the initial concentration of the dye affects the overall adsorption capacity of the solid, with an increase in dye concentration leading to an increase in adsorption capacity. This result matches the sorption plot of other authors, with the maximum adsorption taken as the plateau of the dye adsorbed versus dye added plot. They added that at high loading of the dye on the surface, agglomerates of dye molecules are expected to be predominant, suggesting that the plateau

is not the appropriate value to use for surface area, but instead for cation exchange capacity.

Unfortunately, there were some significant difficulties with respect to measuring ferrihydrite using methylene blue adsorption. Ferrihydrite is not a clayey soil, and has no exchange cations to exchange with the dye. The surface therefore needed to be negatively charged for the cationic dye to bind. This involved a careful choice of buffer solutions, because simply bringing the solid to equilibrium at high pH and then adding the methylene blue was not successful. The dye appeared, actually, to also be a buffer at around pH 6. Additionally, most pH 10 buffers are phosphate based, and phosphate will bind to the surface of ferrihydrite [112, 124, 175]. Methylene blue added to these solutions had to compete with the phosphate to bind to the surface. Only buffers made exclusively with carbonate were at all successful, despite the fact that carbonate will also bind to the ferrihydrite surface [4, 56, 171]. More importantly though, because methylene blue is a dye, the molecule is quite large. As noted in Section 5.5, the suspended ferrihydrite is rather small, and as noted in Section 5.7.5, the pores of the dried and mesoporous ferrihydrite are rather small as well. Thus, while the overall concept of being able to measure the surface area in solution without changing the nature of the solid, particularly for the suspended ferrihydrite, is quite exciting, it is not feasible for these materials. Tests with the dried ferrihydrite showed that although the larger particles would turn blue, indicating sorption of the dye, there was a clear cutoff in particle size when the samples were centrifuged, below which the particles remained the reddish brown of ferrihydrite. It would be interesting to determine what this size cutoff is, but this was beyond the scope of this work as it would never result in a value for the surface area. These difficulties were deemed insurmountable for the purposes of obtaining the surface area of ferrihydrite (particularly suspended ferrihydrite, for which it was the most important to measure in solution), and the measurements with methylene blue were abandoned. It is nonetheless a valuable technique for many other solids where nitrogen adsorption is not a good or viable option.

5.8 Point of Zero Charge of Ferrihydrite

For a description of the theory of point of zero charge, refer to Section 3.2. Many authors have measured the point of zero charge of ferrihydrite, although it is not clear in all cases if the material is 2-line or 6-line ferrihydrite, or if the measurement was made in the presence of CO_2. Four authors confirmed both CO_2-free and 2-line ferrihydrite, and found PZNPC values from titration of 7.8 [30], 7.8 [15], and 5.6-10.3 [113]. Hsi and Langmuir (1985) [60] found a PZC of 7.9 $\pm$ 0.2 from potentiometric and salt titrations. Dardenne (2001) also measured the isoelectric point as 8.7 [30], and Tipping (1981) [158] found an IEP of 8.1-8.2 depending on age. For several authors the use of 2-line ferrihydrite was certain, but the presence of carbonate was not. They measured the PZNPC to be 7.96 [9], 8.0 [137], and 7.6 $\pm$ 0.5 [161]. Pierce and Moore used salt titrations to find a PZC of 8.00 [114]. Five other authors measured the PZC under CO_2-free conditions, but it was unclear if they were using 2-line or 6-line ferrihydrite. Their measured values were 8.2 for the quiescent pH [141]; pH 7, 7.9, and 8.1 for the PZNPC [33, 34, 124, 138], and 5.5 for the isoelectric point [78]. Two other authors have listed PZC values of 8.11 [4] and 7.91 $\pm$ 0.1 [162], but not specified any of the conditions. There are other authors who have measured the PZC of ferrihydrite by

some means, but their work was not accessible to this author.

All of these averaged suggest a CO_2-free PZC for ferrihydrite of around pH 8, which is close to that of goethite (7.4-9.4, average 8.6) and hematite (6.3-10, average 8.1) [27, 75, 76, 77]. This is to be expected based on their structural similarities and the aging properties of ferrihydrite. However, the experiments presented below showed a very different result, with the PZC for dried ferrihydrite being much lower than expected and the PZC for mesoporous ferrihydrite being higher than expected.

5.8.1 Methods of Measurement of the PZC

There are many methods to determine the point of zero charge of a mineral. The three methods employed with ferrihydrite are powder addition (PA), mass titration (MT), and potentiometric titration (PT). All three methods were performed under CO_2-free conditions using ultra high purity argon gas as an inert atmosphere and using CO_2-free solutions prepared by boiling Milli-Q water for at least 20 minutes while bubbling with Ar. CO_2-free NaOH was prepared by dilution using the aforementioned water of base removed carefully from the middle of a saturated solution.

The powder addition method is performed by adding the same amount of the mineral to a set of carbonate-free solutions of varied pH and the same ionic strength. Adding this solid will change the pH of the solution based on the PZC of the mineral; solutions with an initial pH below the PZC will experience an increase in pH as the surface sorbs protons, and the reverse is true of solutions with an initial pH above the PZC. The PZC can be determined by plotting the final minus initial pH values versus the initial pH and determining where final minus initial pH is equal to zero. This procedure was outlined by Cristiano *et al.* and Mustafa *et al.* [27, 101]. The details of these samples are outlined in Section 5.8.2.

Mass titration was developed by Noh and Schwarz (1989) [107] for simple oxides, and further described in Cristiano *et al.* (2011) [27]. It is based on the idea that as the amount of pure amphoteric oxide added to pure water is increased, the solution pH will approach $1/2(pK_1 + pK_2)$, which is equal to the point of zero charge. If only H^+ and OH^- ions are involved on the surface, then it will also equal the isoelectric point. The dry oxide must be pure and uncharged, and the condition equivalent to infinite solid added must be reached by an oxide:solid ratio of 20 % or less to be measured properly by a pH electrode. The technique eliminates the possible surface interactions of electrolytes by using pure water, but this also necessitates the use of CO_2-free conditions to keep the water pure. Results of this technique for ferrihydrite can be found in Section 5.8.3.

Potentiometric titration is a very common method to measure the point of zero charge, and is described well by Parks and de Bruyn (1962) [111] and Cristiano *et al.* (2011) [27], among others. The mineral in question acts as a weak diprotic acid or base that can be titrated by a strong base or acid in solution with a background electrolyte. Just as in mass titration, the PZC can be estimated from the average between pK_1 and pK_2, and is usually computed from the common intersection point of titration curves performed at least three different ionic strengths. The same titration is performed on both the sample and a blank solution of the background electrolyte, which is subtracted from the sample curve. This common intersection point is the point of zero salt effect (PZSE), meaning that the mineral surface is not influence by ionic strength at that point. This will be equal to the PZC when

the mineral is pure, no inner-sphere adsorption occurs, and there is no contribution from either outer-sphere or diffuse swarm ions. For good measurements, the mineral must be pure and have a large surface area, and the system must be kept CO_2-free. Details and results of titration experiments are in Section 5.8.4.

5.8.2 PZC Determination by Powder Addition

Powder addition was chosen as the primary method to determine the PZC of ferrihydrite, as it is fast, requires little material, and seemed to work the best. However, it is by no means a technique without fault. It was difficult to maintain the CO_2-free atmosphere and the original liquid to solid ratio after multiple measurements, the results were not the most consistent with each other, and the measured values tended to drift heavily over time. This drift was suspected to be due to carbonate contamination, as the low PZC materials drifted upward and the high PZC materials drifted downward, but this was never confirmed. The literature descriptions of the technique [27, 101] indicated that measurement at 24 hours was sufficient and that the samples did not drift for months afterward. It seemed that ferrihydrite needed much longer to come to equilibrium, and then drifted heavily. This suggests that the inherent variability, significant surface roughness, and rapid aging of ferrihydrite were at fault for the mixed results. However, the mesoporous ferrihydrite, which does not age, also drifted, suggesting again that the problem is carbonate contamination. This uncertainty was never resolved, and the values listed below as the suggested value were chosen based on whether the sample appeared to have come to equilibrium but not yet begun to drift, how old the sample was when it was measured, and the results of the plutonium sorption curves (Section 5.9.2).

Not all batches of dried ferrihydrite were measured with powder addition, but the primary batches used for plutonium experiments were all measured at least once (batches 2, 3, 5, 7, and 8). For all measurements, 3 mg of ferrihydrite was added to 3 mL of CO_2-free 0.1 M $NaClO_4$ solution that had been pH adjusted to whole pH units between pH 4 and pH 10 using CO_2-free $HClO_4$ and NaOH. Samples were then placed on a rocker. The specifics of each experiment will not be listed here. The pH of all solutions was measured at minimum 24 hours and again at a time greater than or equal to 48 hours later. Many samples were monitored for weeks to months following, but not at regular intervals. A representative plot used for the determination of the PZC is shown in Figure 5.20 and the results of all experiments are shown in Table 5.4.

In general it seemed that the samples loaded into solutions with initial pH values of near 10 had a more difficult time reaching equilibrium, likely due to the fact that the PZC was so much lower than pH 10. Adding ferrihydrite to pH 10 solution may also cause further particle aggregation [46], changing the surface in a measurable way. In many cases removing the pH 10 point improved the agreement of the data between consecutive measurement times and between samples of the same batch, supporting the possibility that the surface chemistry had been changed. To ensure that the data used were for ferrihydrite with the same surface chemistry, often the pH 10 point was removed.

After comparing the data from multiple batches and the sorption behavior of plutonium, the best estimate for the dried nanoparticulate ferrihydrite PZC is around pH 5.5. Although this value could be anywhere between about pH 5.0 and pH 6.5, it is suspected to be near

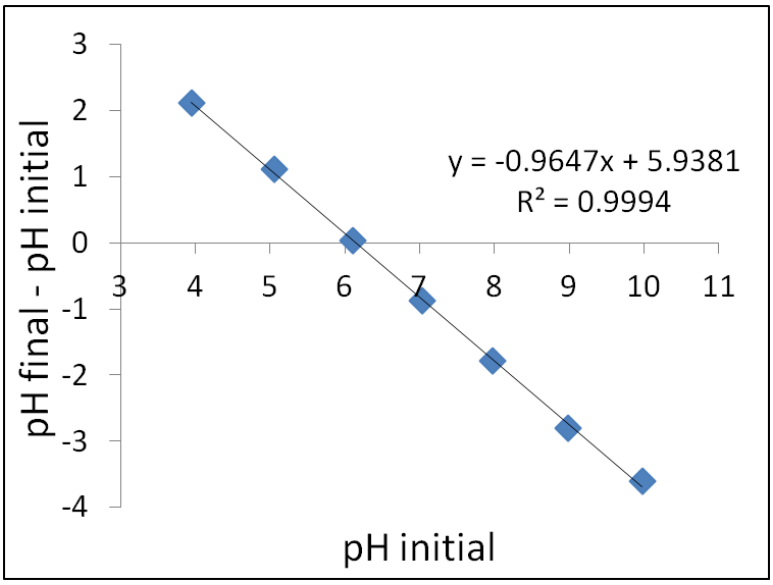


Figure 5.20: Representative plot of the type used for the determination of the point of zero charge of dried nanoparticulate ferrihydrite by the powder addition method. No error bars are calculated. The best fit line is a simple linear fit of the data.

Batch	**Avg. 24 h PZC**	**Est. Equil. PZC**	**≈ Equil. Hrs.**	**Runs**	**≈ Age**
2	5.9 (0.4)	6.36 (0.07)	286	1	7 Mo
3	5.52 (0.06)	6.3 (0.4)*	286	1	6 Wk
5	4.8 (0.1)	4.86 (0.09)*	192	1	5.5 Mo
7	5.96 (0.04)	6.32 (0.06)	150	3	2, 4, 4 Mo
8	4.6 (0.1)	4.9 (0.1)*	48	2	5 Wk, 4 Mo

Table 5.4: Powder addition point of zero charge data for dried nanoparticulate ferrihydrite. Error from the best fit line is listed in parentheses. A * in the "Estimated Equilibrium PZC" column indicates poor or non-existent equilibrium.

the lower range. The samples that showed a powder addition PZC of around 6.3 (batches 2, 3, and 7) all had small amounts of aging at the time as measured by XRD, whereas the samples that registered lower PZC values had less aging (batches 5 and 8). Therefore, it is reasonable to assume that pure ferrihydrite has a PZC near 5.5, which is raised somewhat to about 6.3 by the introduction of small amounts of goethite or hematite into the structure. This increase is logical because the PZC values of goethite and hematite are both significantly higher than that measured here for ferrihydrite.

It is not straightforward why the PZC of the ferrihydrite used here has such a lower PZC than the majority of the values found in the literature. Only Kreller (2002) [78] and Pechenyuk (2000) [113] have measured values close to this, despite many other authors using a very similar synthesis to the synthesis employed here. However, the sorption behavior of plutonium(VI) matches this PZC and not the higher literature PZC of about 8. Perhaps the fact that none of the previous authors used the powder addition method is at fault. The use of other methods to measure the PZC of this ferrihydrite would be useful in determining if this is the case, but those experiments were not successful (see Sections 5.8.3 and 5.8.4).

No method was used to determine the point of zero charge of suspended ferrihydrite, but it is assumed to be nearly the same as the dried ferrihydrite, an assumption strongly supported by the behavior with plutonium(VI) during batch studies (see Section 5.9.2). Because the shape and pH location of the sorption curve was almost identical to the dried ferrihydrite, with the exception of any light-induced chemistry (Section 5.9.3), there is strong evidence that the point of zero charge is nearly identical as well.

The measurement conditions for mesoporous ferrihydrite were basically identical to those for dried ferrihydrite. A representative plot is shown in Figure 5.21. The first batch made by H. Tüysüz was measured only once, but this batch was not used for any of the final plutonium sorption experiments. It had a PZC of 9.46 $\pm$ 0.06 after 20 hours, but after that the PZC just drifted downward. Batch 2 was measured twice, and both runs were in good agreement. The PZC after 24 hours was 8.8 $\pm$ 0.1. The PZC then again drifted downward over time. These drifts were not at regular rates, and suggest variable carbonate contaminations from each measurement, as aging should not be an issue. The carbonate problem from opening the vials during measurement could be greater than for the dried ferrihydrite because the solution pH is so much higher, making the carbonate dissolution easier. Because the mesoporous ferrihydrite has a more regular pore structure, the time to reach equilibrium should be shorter than for the dried ferrihydrite, so the PZC at 24 hours should be the most accurate. Additionally, Batch 2 was used for the majority of experiments and showed an XRD pattern closest to 2-line ferrihydrite, so the best estimate of the PZC from powder addition for mesoporous ferrihydrite is 8.8 $\pm$ 0.1. However, the Pu(VI) sorption data (Section 5.9.2) supports a slightly higher point of zero charge of greater than pH 9, as the sorption of the negative carbonate species of plutonium does not drop off until past pH 9. Thus, the average of both batches may make a better estimate, which is 9.13 $\pm$ 0.06.

This value is also clearly off from the expected value, particularly because surface silica should bring the PZC down lower than that of the nanoparticulate ferrihydrite. The thermal decomposition is expected to give a structure closer to hematite, but the PZC is still on the high end for hematite. Clearly the mesoporous ferrihydrite has a very different surface structure than the nanoparticulate ferrihydrite that causes such different surface charge behavior. The PZC is nonetheless believable due to the Pu sorption characteristics, which

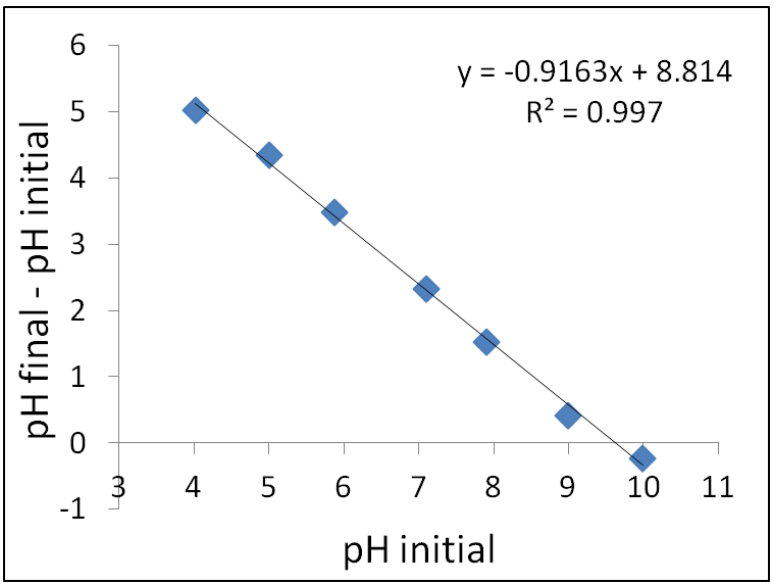


Figure 5.21: Representative plot of the type used for the determination of the point of zero charge of 3D mesoporous ferrihydrite by the powder addition method. No error bars are calculated. The best fit line is a simple linear fit of the data.

do not support a lower PZC.

5.8.3 PZC Determination by Mass Titration

Only dried ferrihydrite batch 7 was used for a mass titration experiment, as the experiment was not deemed particularly successful, and the technique requires a very large amount of material. Ferrihydrite sufficient to achieve oxide:water ratios of 0.01, 0.1, 1, 5, 10, and 20 % were added to 3 mL of CO_2-free Milli-Q water under argon, and the samples were placed on a rocker. The pH of the solutions was measured under argon 24 hours later, as well as several times afterward. The plot of the data obtained at the 24 hour measurement is shown in Figure 5.22. As is clearly visible, the points do not form the correct curve shape (as shown in [27]), and do not appear to come to a final pH level. However, if the assumption is made that the 20 % oxide to water ratio is the most likely to represent the point of zero charge, then the PZC at 24 hours was 5.13. This pH drifted both up then down over the course of measurement (5.89, then 5.77, then 5.88, then 5.98 by almost 2000 hours). These values are also relatively close to the average pH of all measured samples. This would suggest a value of around 5.83 as an equilibrium value, but it is not a particularly strong suggestion due to the poor establishment of equilibrium. It is at least relatively close to the value obtained by powder addition (Section 5.8.2), which is encouraging.

5.8.4 PZC Determination by Potentiometric Titration

These measurements are performed using an automatic titrator (751 GPD Titrino by Metrohm), and it is notoriously difficult to achieve titrations that are free of carbonate.

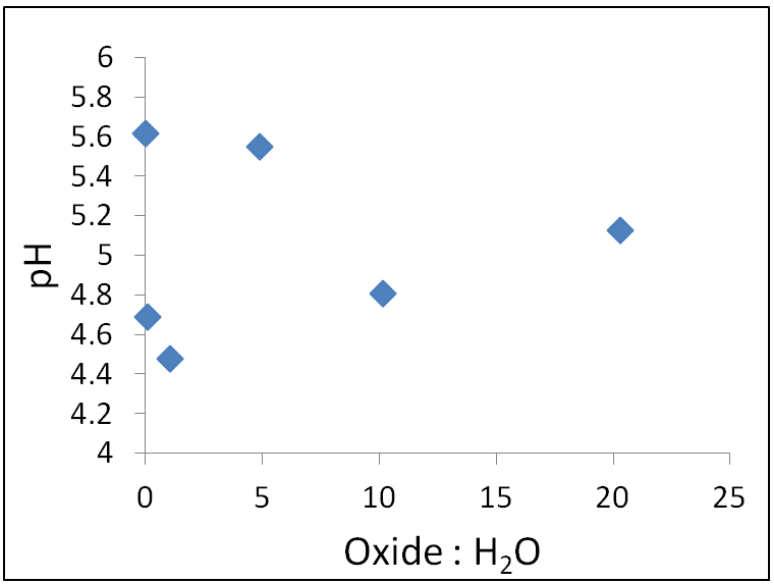


Figure 5.22: Plot of measured pH as a function of oxide:water ratio after 24 hours for dried ferrihydrite. No error bars are calculated.

Very few titrations were performed with dried ferrihydrite, and carbonate was never successfully excluded. Additionally, no common intersection point was found for the three ionic strengths measured (0.001, 0.01, and 0.1 M $NaClO_4$). Extensive efforts were made to remove carbonate, and all were unsuccessful. Due to the greater success and simplicity of the powder addition method and the overly time-consuming nature of the potentiometric titrations, the potentiometric titrations were abandoned.

5.9 Plutonium Sorption onto Ferrihydrite

5.9.1 Introduction

McBain proposed the term sorption in 1909 to include both adsorption (condensation or binding to the surface) and absorption (penetration into the mass of the solid) [49]. Because the mechanism and configuration involved in the removal of plutonium from solution by the solid are not known, the binding of plutonium will be referred to as sorption.

The sorption on ferrihydrite of species such as arsenate [170], chromate [180], lutetium [30, 31], americium [148], neptunium [47], and uranium [42, 43, 53, 56, 60, 98, 112, 120, 122, 167, 171] have all been studied. However, no literature was found concerning plutonyl sorption onto ferrihydrite with the exception of one study on natural iron oxide colloids with many elemental impurities [69] and another calculating the interaction [79]. While the chemistry between uranyl and plutonyl species should be similar, and thus the research on uranyl is very important, it is not exactly the same. Therefore, an investigation of the interactions between plutonium and the iron oxyhydroxide ferrihydrite is warranted.

The following sections detail batch sorption studies of Pu(VI) on ferrihydrite as well as X-ray absorption spectroscopy data on the formed complexes. These studies have been

performed at varying Pu(VI) concentrations, varying pH conditions, and varying exposure to light to elucidate the sorption envelope (or sorption curve), the capacity, and the role of light exposure on uptake. The data are presented in approximately chronological order so that the reader may understand the logic that led to the conclusions reached at the end. They are then compared to relevant U(VI) data.

5.9.2 Batch Studies

The same general procedure was followed for most batch sorption studies, and exceptions will be noted when appropriate. 8 mg of ferrihydrite was added to 8 mL of 0.1 M $NaClO_4$ to give a concentration of 1 g/L, and the pH was balanced to whole pH values between pH 4 and pH 10 (pH 9 for some sets). Plutonium stocks were created by removing and diluting an aliquot from a concentrated stock recently boiled in concentrated $HClO_4$, verifying them to be Pu(VI) by UV-visible spectroscopy (see Chapter 2), and assaying them using LSC to determine the concentration. Sufficient Pu was then added to the samples to reach the desired concentration, which was 16 μM Pu(VI) in most cases. Samples were brought back to the desired pH using small amounts of NaOH and $HClO_4$, shaken well, and left on a rocker to reach equilibrium. The final volume and time of the Pu addition were noted. Samples were opened to air and no effort was made to exclude carbonate. After known time intervals, the samples were allowed to settle, the pH was measured, and a 40 μL aliquot removed for filtration using a 30,000 MWCO regenerated cellulose filter (Microcon or Vivacon) centrifuged at an RCF of around 3000 x g for 15 minutes. Two 10 μL aliquots were removed from the filtrate and measured using LSC to determine the amount of Pu remaining in solution. Because the amount of Pu added was a known quantity, simple subtraction indicated the amount of Pu bound to the surface.

The concentration determination does, however, involve some amount of error because the determination of the final volume relies on the volume markings on the Falcon vials, which is only marked in half milliliter increments. Estimation can generally be made to the tenth of a milliliter, and this was accounted for in the error calculations. However, some low pH samples where essentially no Pu had bound were measured to have concentrations exceeding the calculated Pu concentration, meaning that the sample volume prior to assaying had been overestimated. In these cases the maximum recorded Pu concentration from assays was used as the initial Pu concentration, and the other data points adjusted accordingly. This adjustment never changed the reported concentrations by more than a few percent, but did greatly increase the error associated with the values. All vertical error bars reported here were calculated to the 1 σ level using the error in the counting statistics, the standard error to reflect the agreement between assays, and the error in all other volume and mass measurements. Error in the pH measurements is estimated for all samples to be approximately 0.25 pH units. The possibility of either sorption of Pu to the filters or concentration of Pu during the filtering process was also investigated to ensure that the data were an accurate representation of the solution. Only at neutral pH conditions and low Pu concentrations were the filters found to remove some Pu from solution. The effect on the data was small enough to not be a concern. A discussion of these tests can be found in Appendix D.

Both the mesoporous and the dried ferrihydrite are powders, and were easily weighed to determine the amount added. The suspended ferrihydrite is not as straightforward, and

two methods were employed to determine the amount of suspension to be added to each sample. Aliquots were removed and either dissolved to be measured for Fe content using ICP-MS or added to a tared vessel to dry to determine the mass. For ICP-MS calculations, the formula of Michel *et al.* (2007) [95], which is $Fe_{10}O_{14}(OH)_2$. However, the mass recorded following drying was greater than that calculated from this formula, suggesting that there is additional water in the ferrihydrite structure not taken into account in the above formula. Therefore, while efforts were made to keep the amount of suspended ferrihydrite added as close to 8 mg as possible, some samples may have up to 10.7 mg rather than the desired 8 mg. However, the amount added for each experimental set was the same for each sample within that set, and thus the trends reported below are just as valid. The only value affected is the overall capacity, and as shown in Section 5.9.4, the capacity was not reached with these experiments, nor was it reached for the dried ferrihydrite. Because the suspended is expected to have an overall higher sorption capacity due to a higher expected surface area, it is a safe assumption that the uncertainty in the amount of suspended ferrihydrite added is not a factor that prevented the determination of the capacity.

The first set of sorption curves was measured under normal ambient laboratory conditions with a relatively recently boiled Pu(VI) stock estimated to have less than 10 % Pu(V), and were measured approximately every 24 hours for one week. The curves are shown in Figures 5.23, 5.24, and 5.30. Recall from Section 5.8 that the point of zero charge of the nanoparticulate ferrihydrite is around pH 5.5 and the PZC of mesoporous ferrihydrite is just over pH 9. Below these PZC values, the surfaces will be positively charged, and above these PZC values, the surfaces will be negatively charged. Combining this information with the Pu(VI) speciation diagram (Figure 2.4) allows for a good understanding of why the sorption curves look the way they do. This is shown for the suspended ferrihydrite in Figure 5.25. At low pH, where both the Pu and the surface are positively charged, there is little to no sorption due to electrostatic repulsion. For the nanoparticulate ferrihydrite, the increase in sorption corresponds to positive and neutral Pu species binding to an increasingly negative surface, and the sorption drops off again once the negatively charged Pu carbonate species begin to form above pH 8. The rise in sorption occurs at a higher pH for the mesoporous ferrihydrite due to the higher PZC. Thus, the shape and location of the sorption curve is easily explained. The exception to this is the sorption beyond the first day for the dried ferrihydrite, which will be discussed momentarily. The other point of interest is that the sorption for the suspended and mesoporous ferrihydrite does not greatly increase with each day, indicating that the kinetics of the sorption reaction is fast enough that all sorption occurs within the first 24 hours.

As mentioned above, the increasing sorption with each day is highly unexpected. At pH 4, the surface and the Pu species are both positively charged, and electrostatics would indicate that no sorption should occur. To confirm that the sorption was not an experimental mistake, the experiment was repeated at 16 μM Pu. However, the stock was significantly older in this case. The sorption curve for this experiment is shown in Figure 5.27. It should be noted that the pH 9 sample did not reach the appropriate pH, and the data was dropped.

This sorption curve clearly shows the same behavior, but with a significantly more pronounced initial sorption at low pH. This confirms that the behavior was not a random event, and also confirmed the hypothesis that there must another factor involved that causes the sorption at low pH.

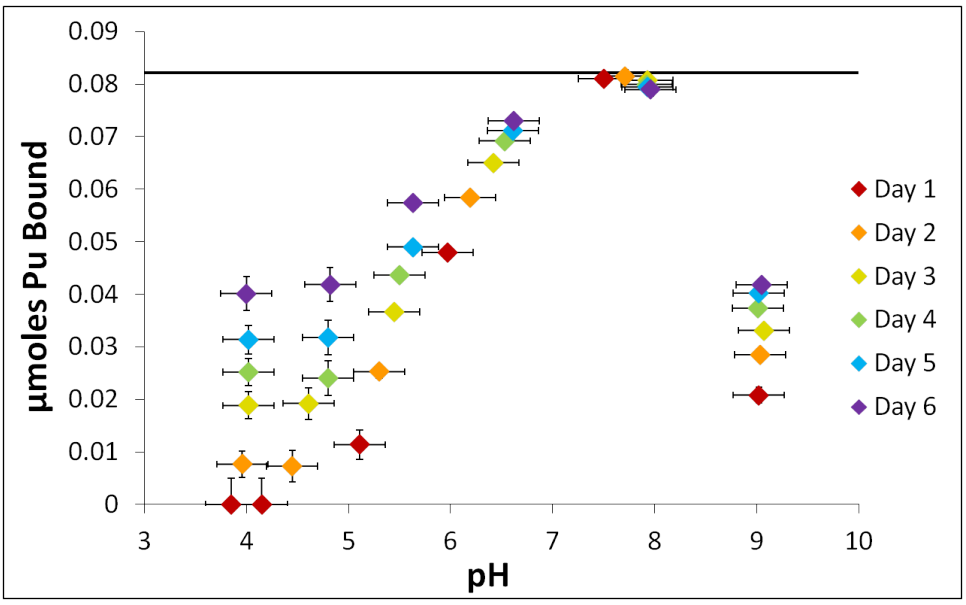


Figure 5.23: Sorption curve for dried nanoparticulate ferrihydrite with 10 μM Pu(VI) in the light. The horizontal line indicates the μmoles of Pu originally added to the solution.

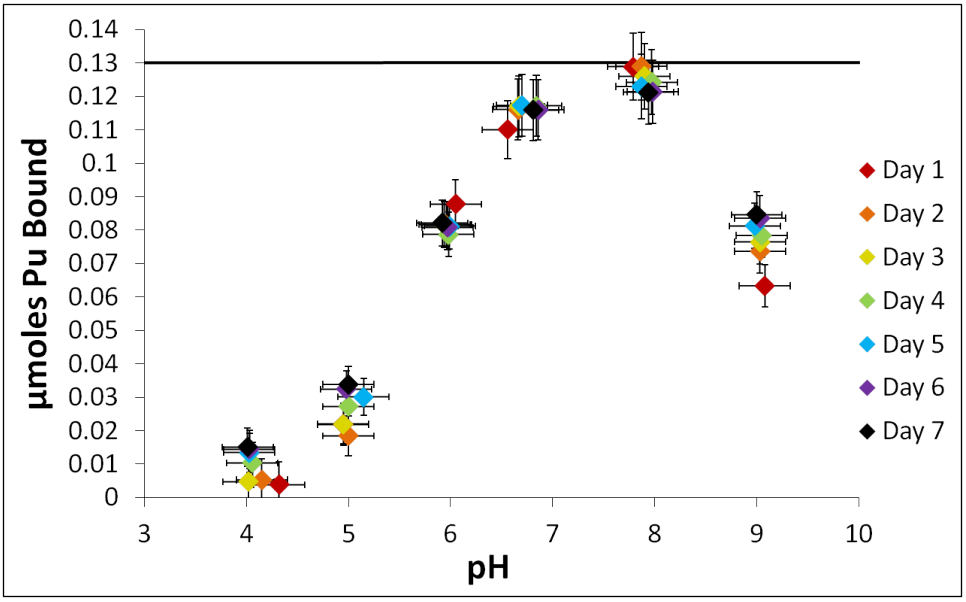


Figure 5.24: Sorption curve for suspended nanoparticulate ferrihydrite with 16 μM Pu(VI). The horizontal line indicates the μmoles of Pu originally added to the solution.

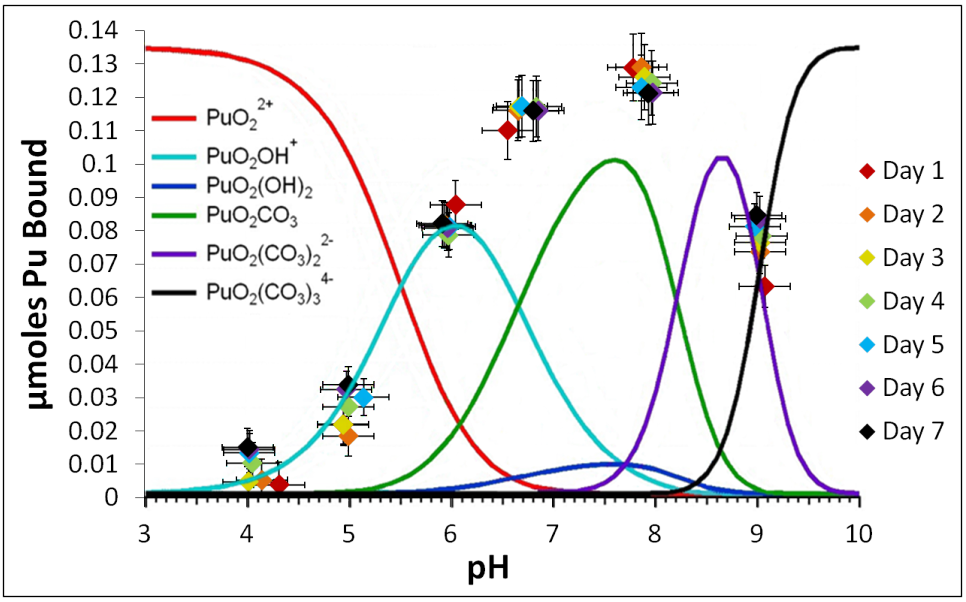


Figure 5.25: Sorption curve for suspended nanoparticulate ferrihydrite with 16 μM Pu(VI) compared to a Pu(VI) speciation diagram. The error bars on the speciation diagram have been removed for clarity.

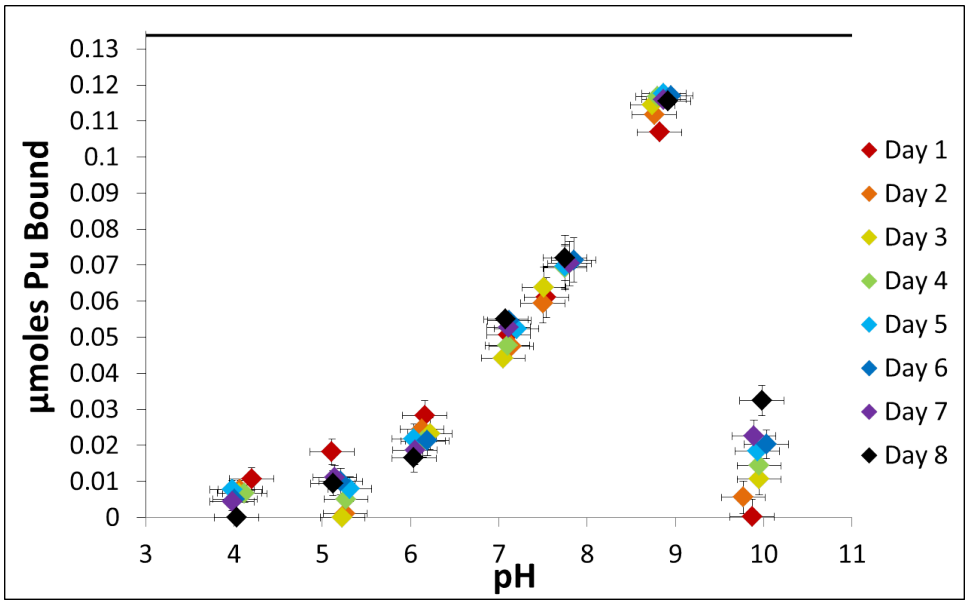


Figure 5.26: Sorption curve for mesoporous ferrihydrite with 16 μM Pu(VI). The horizontal line indicates the μmoles of Pu originally added to the solution.

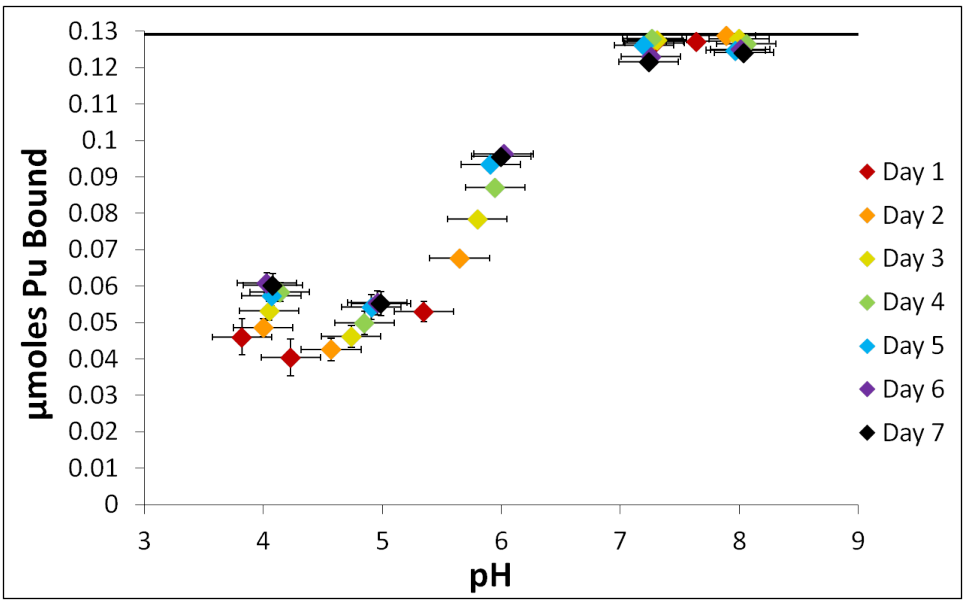


Figure 5.27: Sorption curve for dried nanoparticulate ferrihydrite with 16 μM Pu(VI) in the light. The horizontal line indicates the μmoles of Pu originally added to the solution.

While Pu(VI) will not bind at such a low pH, Pu(IV), would. Pu(IV) is not soluble at pH 4 at these concentrations (see Figure 2.3), and would therefore either bind to the surface or precipitate on it. Because ferrihydrite has such high surface reactivity, Pu(IV) may be more likely to bind than to precipitate. This was a logical conclusion, but both a mechanism for the reduction and more evidence was necessary to fully suggest reduction to Pu(IV) as the cause for the sorption on dried ferrihydrite at low pH.

The first step was to determine the possible causes, of which there are three primary options. The first and most obvious is the autoreduction of Pu(VI) (Section 2.4). Autoreduction is the likely cause of the difference between the sorption shown in Figure 5.23 and Figure 5.27, because an older stock would have been more reduced when added to the sample, and thus the initial sorption would be increased by the amount that had reduced. However, autoreduction is not fast enough to account for the increase seen each day in the sorption at pH 4; it is in fact about 20 times too slow. Therefore, while autoreduction is certainly occurring in all of these samples, it is highly unlikely to be primary cause of the reduction.

The second option is the presence of Fe(II), which could certainly cause the reduction of Pu(IV). While there may be small amounts of Fe(II) present, this is also unlikely to be the primary cause of the reduction. The dried ferrihydrite was made from 99.99 % pure iron nitrate. Additionally, the suspended ferrihydrite has the same elemental composition as the dried, and no reduction was seen for the suspended samples. Finally, the mesoporous ferrihydrite was made from a much lower purity iron nitrate which would have even more Fe(II), and no reduction was seen with the mesoporous ferrihydrite either. Thus, Fe(II) is unlikely to be the culprit.

The third and final option is light-induced photochemistry. Ferrihydrite is a semiconductor with a band gap between 1.5 and 2.7 eV [86], which corresponds very well with two of the primary peaks of the glovebox fluorescent lighting at 550 nm (2.25 eV) and 610 nm

(2.03 eV) (Figure 5.42). There may also be more energetic light emission in the UV range from mercury [118]. Exposure to light was seen to cause the reduction of Pu(V) to Pu(IV) at low solution concentration (10^{-8} M) when sorbed to goethite and hematite [115], so it is very reasonable to assume that ferrihydrite could do the same. The following section (Section 5.9.3) details the experiments that resulted from this discovery that further indicate that ferrihydrite is a photocatalyst for the reduction of Pu(VI) to Pu(IV) under even general laboratory lighting.

After determining that light exposure was a factor, particularly for the dried ferrihydrite, new sorption curve data were collected with the samples in the dark. Final sorption curves that include the reasonably acceptable data from all pH dependent experiments are shown in Figures 5.28, 5.29, and 5.30. These data indicate that all three materials sorb Pu(VI) according to what would be expected based on their respective PZC values and the Pu(VI) speciation in solution when no light exposure is allowed.

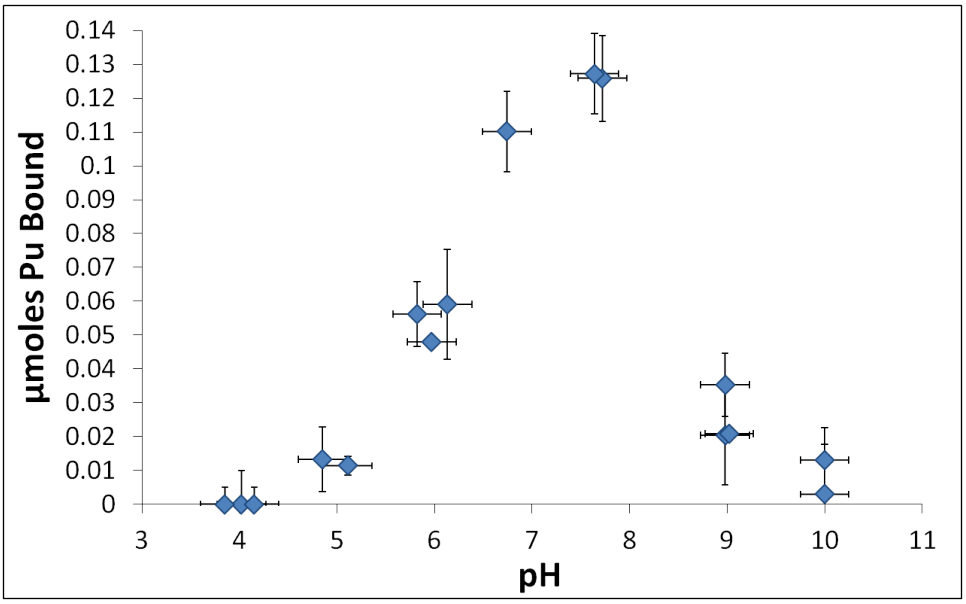


Figure 5.28: Sorption curve for dried nanoparticulate ferrihydrite with 16 μM Pu(VI) without light-induced chemistry. The horizontal line indicates the μmoles of Pu originally added to the solution.

As stated in the introduction, no previous studies reported the sorption of plutonium onto pure ferrihydrite, but several have investigated uranium. A comparison of these studies and the present work is instructive for understanding the similarities and differences between the chemistry of Pu(VI) and U(VI). The sorption curve for U(VI) from Wazne *et al.* (2003) [171] in the presence of carbonate, but in 0.01 M NaCl, are quite similar to those for the nanoparticulate ferrihydrite with Pu(VI). These data are shown in Figure 5.31. However, it is clear that due to the differences in U(VI) speciation (comparing Figure 5.32 to Figure 2.4), the sorption envelope is shifted to lower pH for U(VI) than it is for Pu(VI). In particular, the neutral carbonate species begins to appear around pH 3.5-4 for U(VI), but does not appear until pH 4.5-5 for Pu(VI). More substantial shifts to lower pH are seen for the U(VI) negative hydroxide and carbonate species, with the first negative carbonate species appearing between

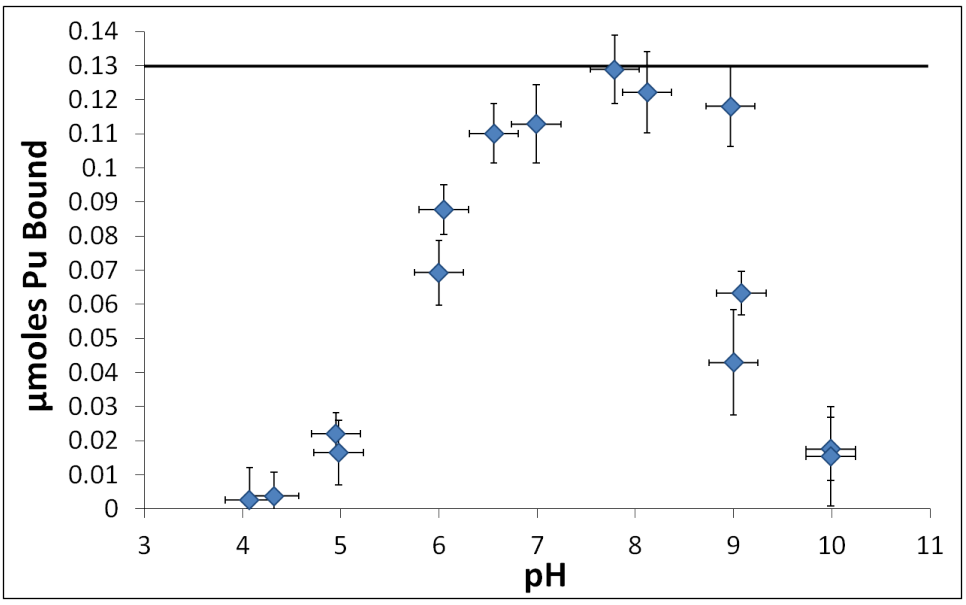


Figure 5.29: Sorption curve for suspended nanoparticulate ferrihydrite with 16 μM Pu(VI) without light-induced chemistry. The horizontal line indicates the μmoles of Pu originally added to the solution.

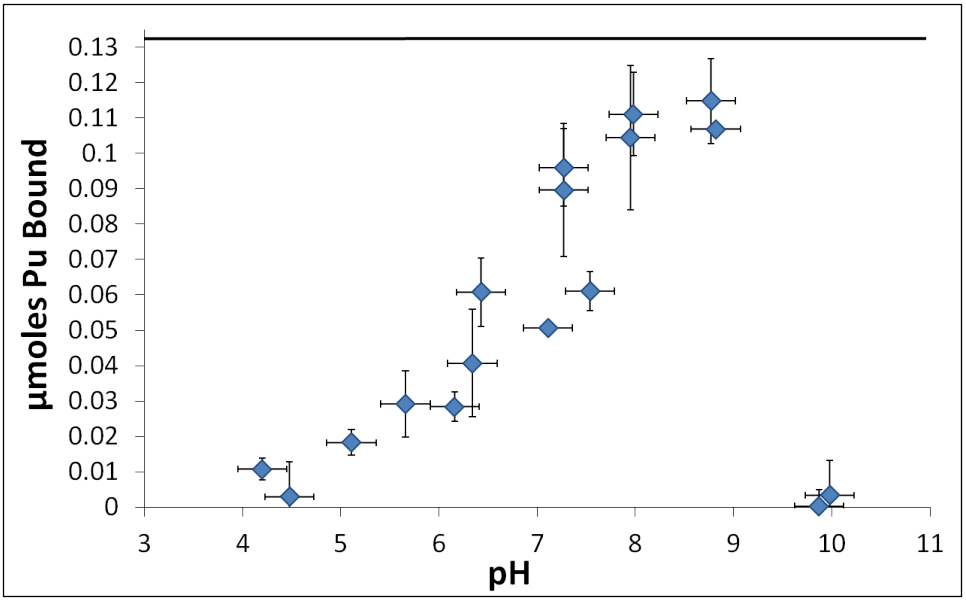


Figure 5.30: Sorption curve for mesoporous ferrihydrite with 16 μM Pu(VI) without light-induced chemistry. The horizontal line indicates the μmoles of Pu originally added to the solution.

pH 5 and 6 for U(VI) but not until pH 7 to 8 for Pu(VI). These are the types of differences that are incredibly important to elucidate, rather than just trusting that U(VI) is a good enough model for Pu(VI).

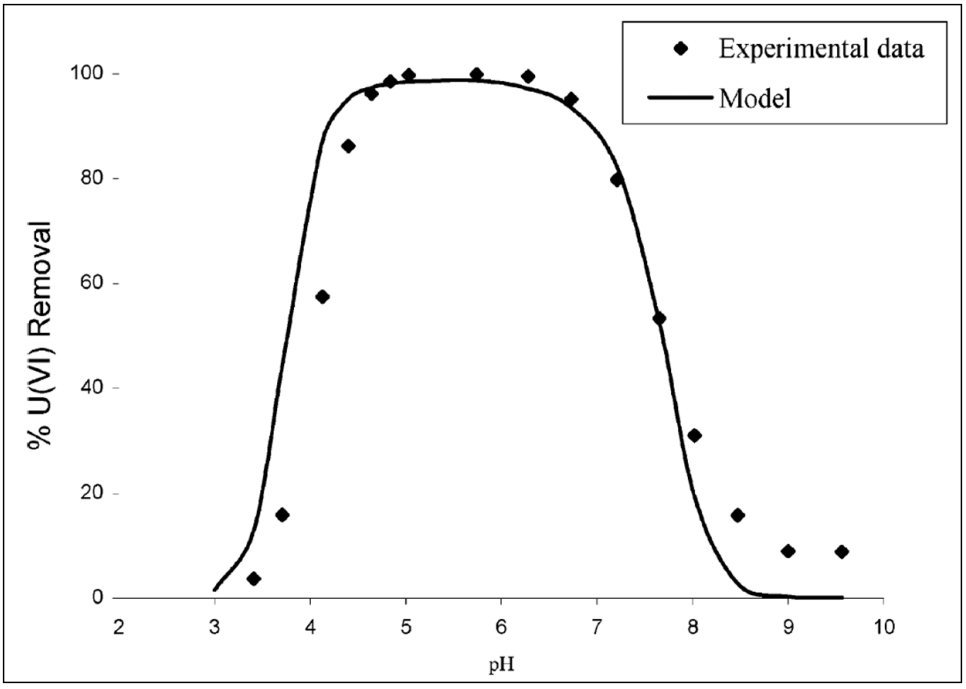


Figure 5.31: Experimental data and model fit for sorption of 4.2 μM U(VI) to ferrihydrite in 0.01 M NaCl solution containing 0.01 M carbonate. From Wazne *et al.* (2003) [171].

5.9.3 Light-Induced Chemistry

Data

The sorption at low pH for dried ferrihydrite described in Section 5.9.2 was further investigated with respect to the light-induced chemistry. Because pH 4 is a pH at which the Pu(VI) will not bind but light-reduced Pu(IV) will, it was an obvious choice for using batch studies to elucidate the light-induced redox behavior of plutonium on ferrihydrite.

Two dried ferrihydrite samples were loaded initially as a further proof of concept experiment: one exposed continuously to fluorescent glovebox and laboratory lights, and the other wrapped in aluminum foil to exclude light and measured with the laboratory lights on but the glovebox lights off. Samples of this type will be referred to simply as the light and dark samples, respectively. 8 mg of dried batch 7 was added to 8 mL of 0.1 $NaClO_4$ at pH 4 before adding 16 $\pm$ 1 μM Pu(VI). Samples were maintained at pH 4, with a maximum pH of 4.25, and assayed on days 1, 2, 3, 5, 16, 23, 26, 31, and 37. The sample wrapped in foil was exposed to light starting after the day 23 assay to ensure that that sample would exhibit the same sorption behavior upon exposure to light. The results of this experiment are shown in Figure 5.33, and clearly show a significant difference between the sorption with the exposure of light. The dark sample also exhibits the same plutonium uptake upon exposure to light.

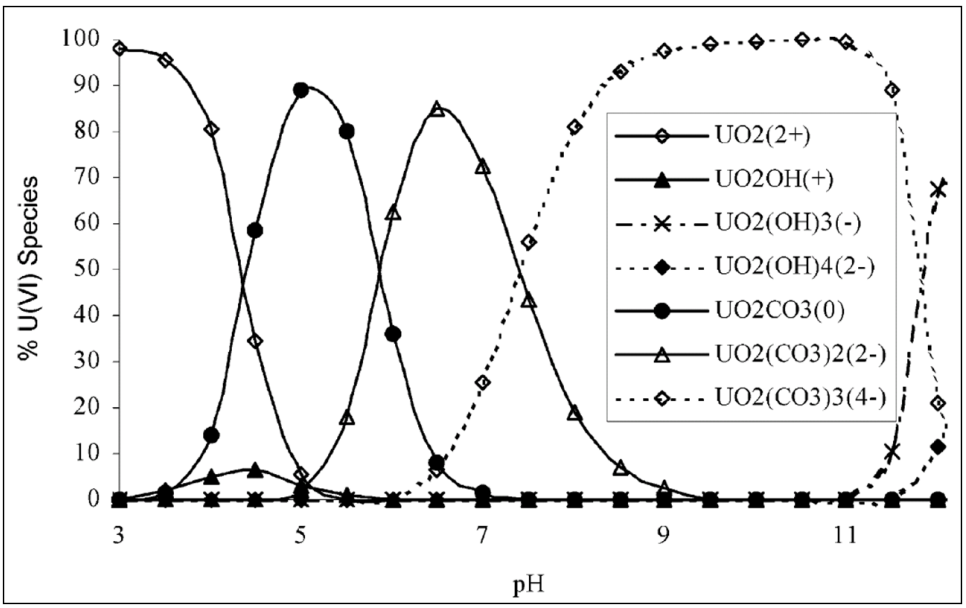


Figure 5.32: Speciation of 4.2 μM U(VI) in 0.01 M NaCl solution containing 0.01 M carbonate. From Wazne *et al.* (2003) [171].

There is still more sorption than expected on the dark sample for days 0 to 23; however, this may be due to ambient light exposure during measurement because this was the first experiment of this type performed.

Following this proof of concept experiment, repeat experiments were performed in duplicate with dried batches 7 and 8 (Figures 5.34 and 5.35), suspended batch 8 (Figures 5.36 and 5.37), and mesoporous ferrihydrite (Figures 5.38 and 5.39). These results show a clear trend in light-induced reactivity, with the dried ferrihydrite showing far greater reactivity than the suspended ferrihydrite, which showed more reactivity than the mesoporous ferrihydrite.

It is noteworthy that the dried ferrihydrite results shown in Figures 5.34 and 5.35 differ from the results in Figure 5.33 in the magnitude of the plutonium sorption. After several days of measurement, the dried ferrihydrite came out of solution and sat on the surface of the liquid in a film, a behavior that was not observed for the proof of concept experiment. There are several possible explanations for this behavior. If gas bubbles were produced, they could become trapped at the particle surface and in the micropores, causing the particles to float. The surface could also have somehow become hydrophobic. Either way, this behavior did not seem to be light-induced, as the dark samples exhibited the same trend. It appears to be pH dependent, as some lower pH samples from the sorption curves displayed in Section 5.9.2 also showed this behavior. Whatever the cause, the floating behavior greatly reduced the amount of solution that the ferrihydrite particles came into contact with, severely limiting the amount of plutonium that would interact with the surface. This led to a decreased overall sorption amount for these samples. However, even with this decrease in sorption there is a significant difference between the dark and light samples.

To further understand how particle size and crystallinity play a role in these light-induced reactions, samples of the suspended "ferri-goethite" created by allowing a suspension of ferrihydrite to age to primarily goethite were also measured and the results are shown in

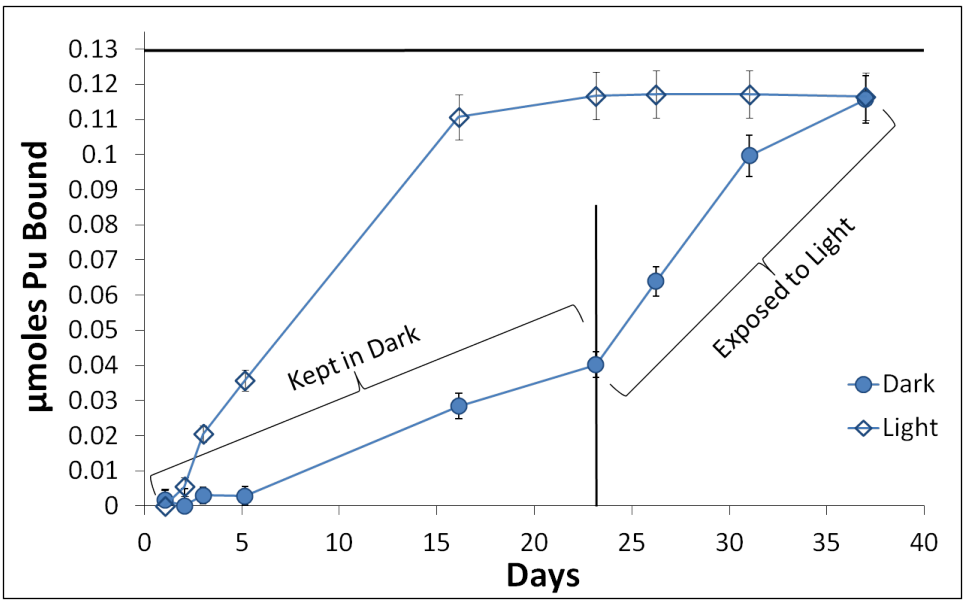


Figure 5.33: Sorption of 16 μM Pu on dried ferrihydrite as a function of light exposure. The vertical line indicates the deliberate exposure of the dark sample to light following the assay on day 23. The horizontal line indicates the μmoles of Pu originally added to the solution.

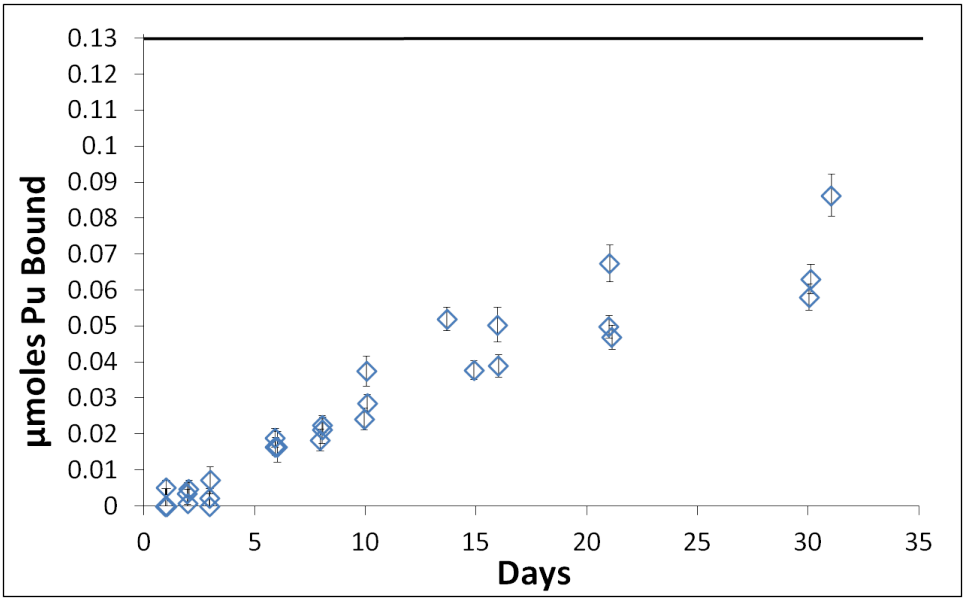


Figure 5.34: Sorption of 16 μM Pu on dried ferrihydrite when exposed to glovebox and laboratory lights. The horizontal line indicates the μmoles of Pu originally added to the solution.

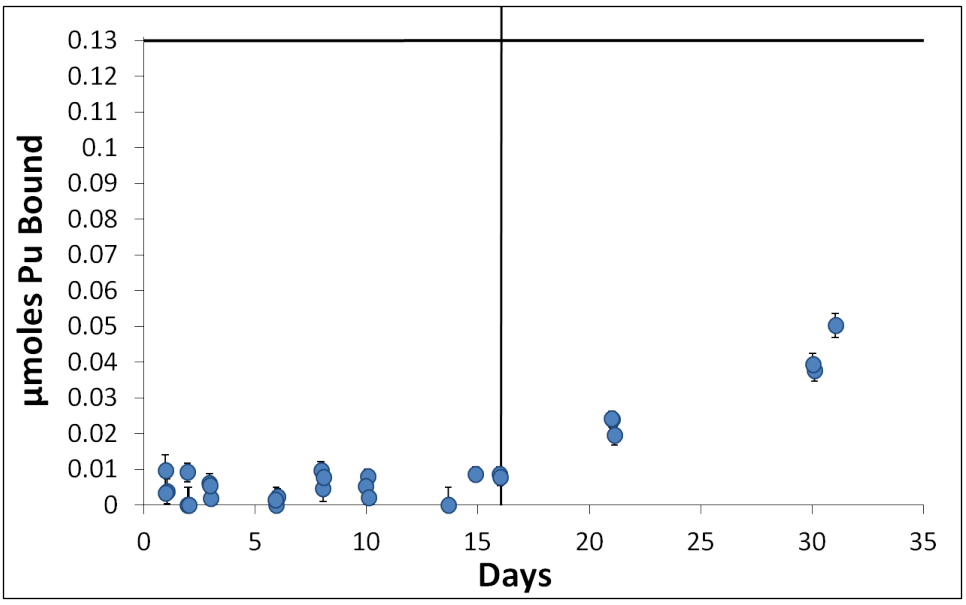


Figure 5.35: Sorption of 16 μM Pu on dried ferrihydrite shielded from glovebox and laboratory lights. The vertical line indicates the deliberate exposure of the sample to light. The horizontal line indicates the μmoles of Pu originally added to the solution.

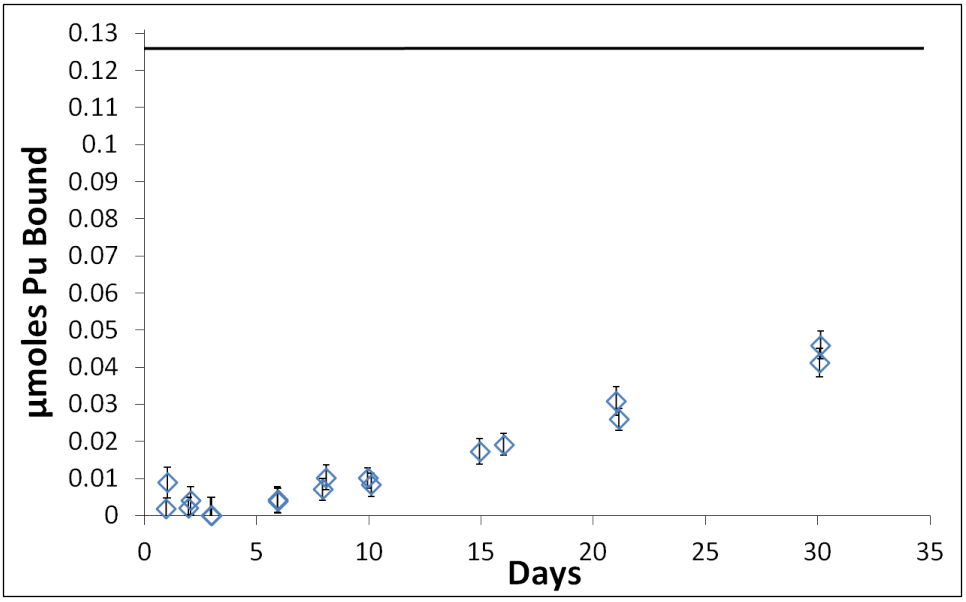


Figure 5.36: Sorption of 16 μM Pu on suspended ferrihydrite when exposed to glovebox and laboratory lights. The horizontal line indicates the μmoles of Pu originally added to the solution.

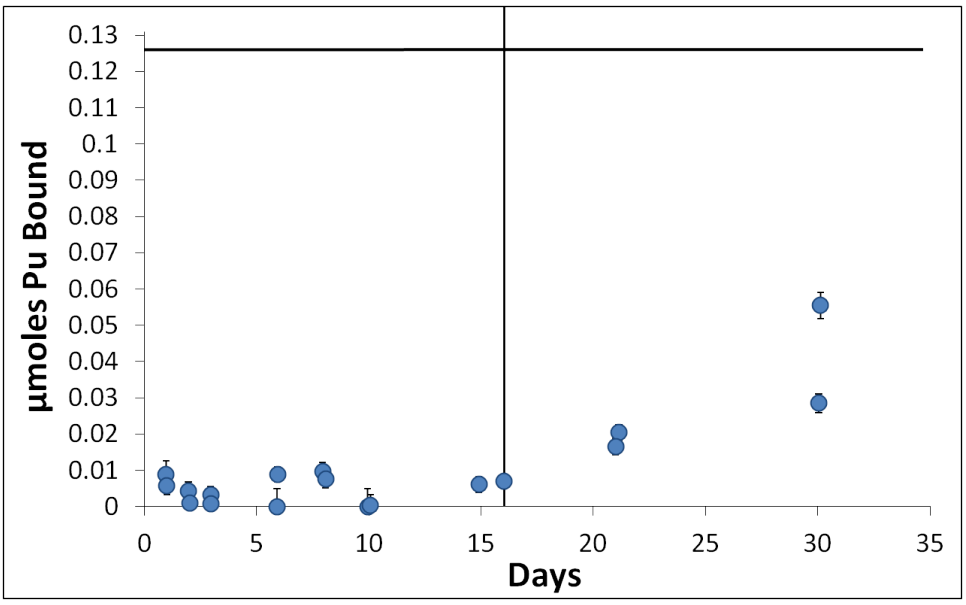


Figure 5.37: Sorption of 16 μM Pu on suspended ferrihydrite shielded from glovebox and laboratory lights. The vertical line indicates the deliberate exposure of the sample to light. The horizontal line indicates the μmoles of Pu originally added to the solution.

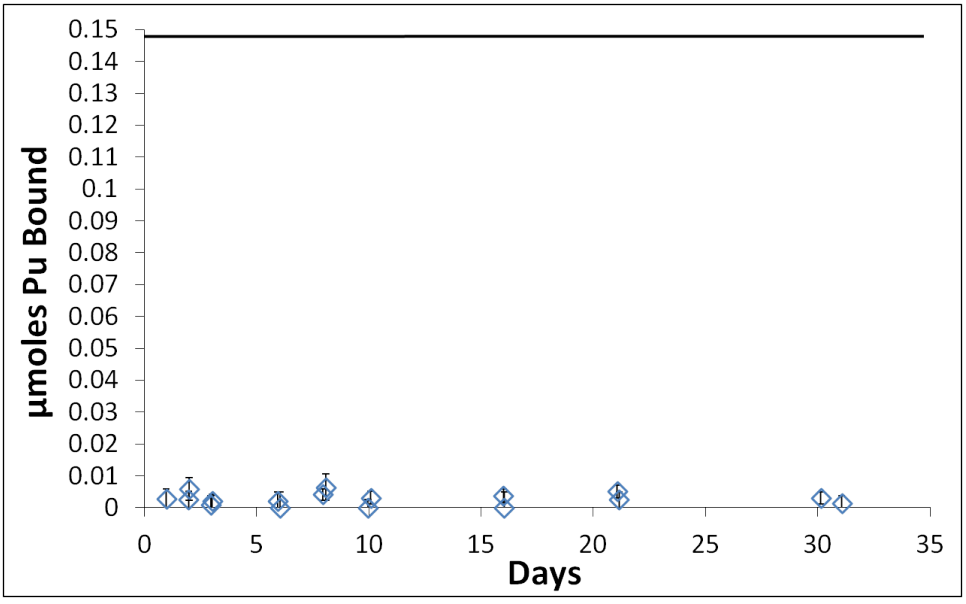


Figure 5.38: Sorption of 16 μM Pu on mesoporous ferrihydrite when exposed to glovebox and laboratory lights. The horizontal line indicates the μmoles of Pu originally added to the solution.

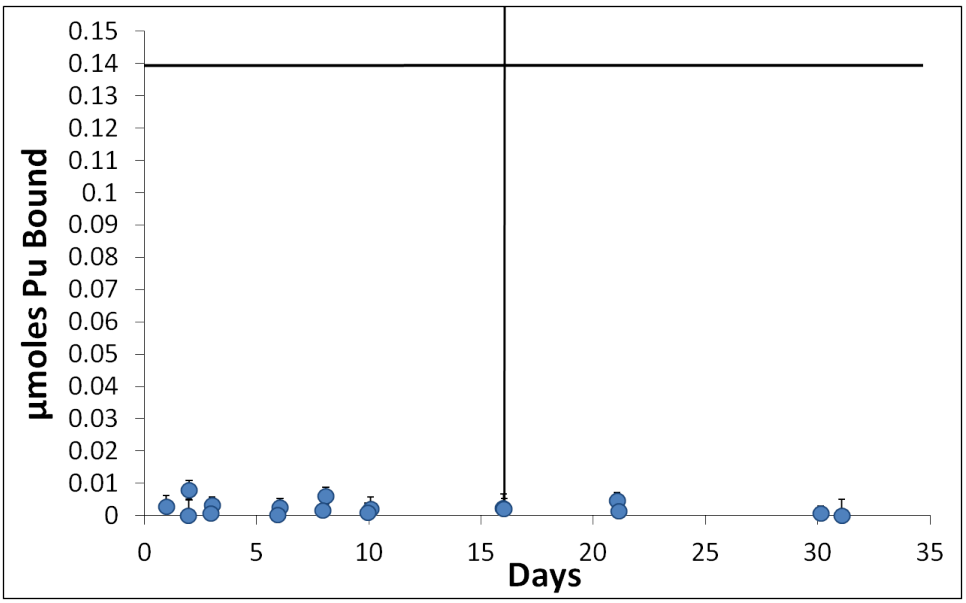


Figure 5.39: Sorption of 16 μM Pu on mesoporous ferrihydrite shielded from glovebox and laboratory lights. The vertical line indicates the deliberate exposure of the sample to light. The horizontal line indicates the μmoles of Pu originally added to the solution.

Figures 5.40 and 5.41. In a similar manner as the dried ferrihydrite, the suspended "ferrigoethite" also showed strong photocatalytic activity. TEM measurements of these particles showed that they were slightly larger than suspended ferrihydrite, measuring at around 5-6 nm instead of 2-3 nm.

Discussion

In order for the Pu(VI) to be reduced to Pu(IV), two electrons must be transferred from the ferrihydrite to the plutonium. For this electron transfer to occur, an electron-hole pair must be formed by the excitation of an electron from the valence band to the conduction band, and that electron must travel to the surface of the particle and interact with a plutonyl molecule. The concepts necessary to understand how this process can occur are described in Section 3.3. The specifics of how these concepts relate to the system at hand are described here, first relating to the formation of the electron-hole pair, followed by the diffusion of that electron to the surface, and concluding with the actual charge transfer to the plutonium. These concepts will first be described for the dried ferrihydrite before presenting possible explanations for the differences between the materials.

Semiconductors will absorb light of a wavelength below a particular threshold wavelength that corresponds to the energy of the band gap of the material. For ferrihydrite, that wavelength is 459-827 nm based on the measured band gap energies of Liu *et al.* [86], which is in the visible range of light and within the range of emission for the glovebox lamp.

The emission spectra of the lighting used in the laboratory is shown in Figure 5.42. The primary spectrum of concern is that for the glovebox lights, as the room lights provide only diffuse light to the samples. However, the laboratory light spectrum is what the dark samples

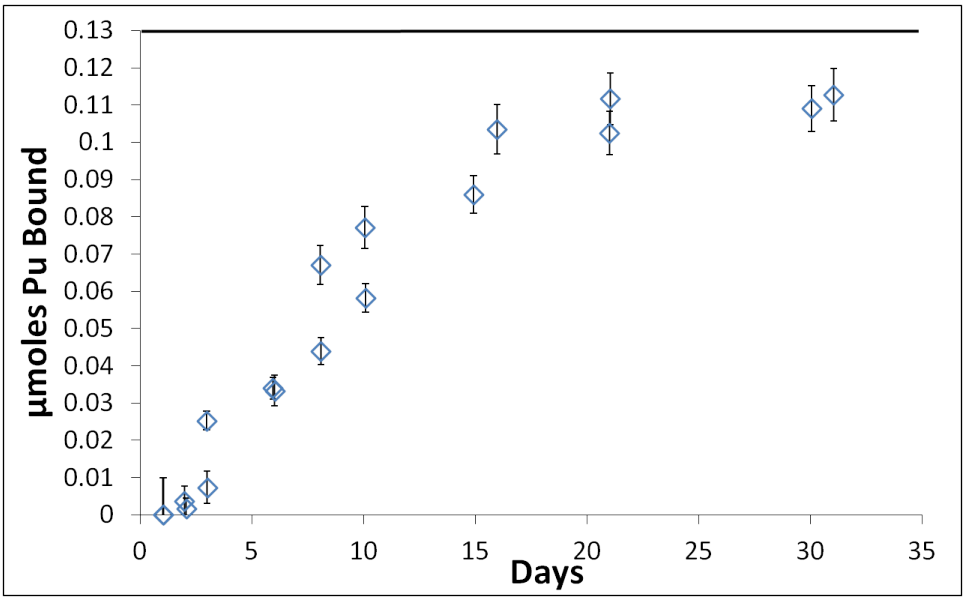


Figure 5.40: Sorption of 16 μM Pu on suspended "ferri-goethite" when exposed to glovebox and laboratory lights. The horizontal line indicates the μmoles of Pu originally added to the solution.

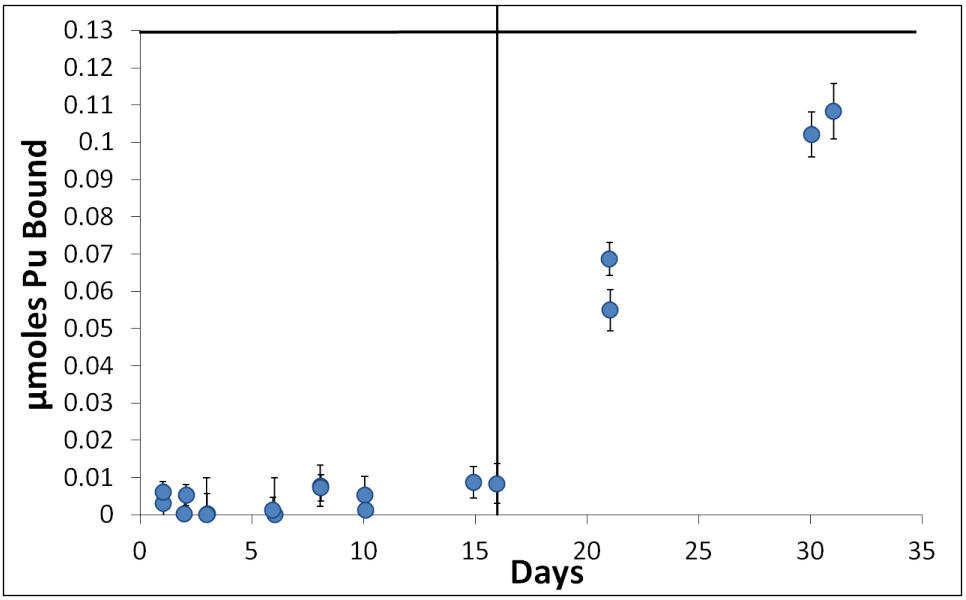


Figure 5.41: Sorption of 16 μM Pu on suspended "ferri-goethite" shielded from glovebox and laboratory lights. The vertical line indicates the deliberate exposure of the sample to light. The horizontal line indicates the μmoles of Pu originally added to the solution.

can be exposed to during measurement, although the light is very dim. The laboratory light spectrum matches that of a typical "cool white" fluorescent lamp with a rare earth phosphor, and the glovebox light is a Sylvania 30 W halophosphate phosphor lamp. Both spectra show the strong mercury peaks at 435.833 and 546.074 nm [118], but the laboratory light has a primary peak at 611 nm from the Eu^{3+} in Y_2O_3 whereas the glovebox light shows the broadband halophosphate emission from around 450 to 675 nm. There are also higher energy mercury lines, but the absorption cross section is likely quite low as absorption of light at those energies would be an indirect transition [48].

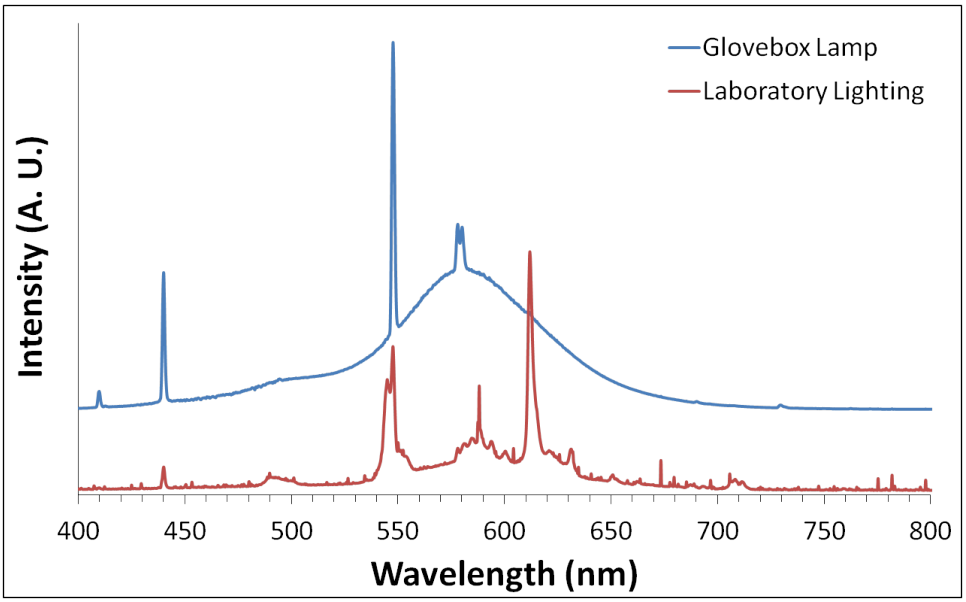


Figure 5.42: Emission spectrum of the fluorescent light bulbs used in the glovebox and for the general laboratory lighting for plutonium sorption experiments as measured by an Ocean Optics USB2000 spectrometer from 400 to 800 nm. The spectrum has not been energy or intensity calibrated. Comparison of the mercury line at 546.074 nm [118] to the spectrum suggests that the measured wavelengths are red shifted by about 1.5 nm.

The broadband halophosphate emission of the glovebox lamps coincides nicely with the band gap energy range for ferrihydrite, easily explaining the production of electron-hole pairs in dried ferrihydrite.

Hematite is an n-type semiconductor (electron donor) [116], and it is reasonable to assume that ferrihydrite is as well because the structures are so similar, although it has not been measured. This means that electrons migrate across the depletion layer at the ferrihydrite-electrolyte interface to react with holes from the electrolyte or an electroactive species in solution. Once the electrons and holes recombine, the n-type particle will have positively charged ions remaining, and the electroactive species in solution will have gained electrons, having acted as a counter electrode [166]. This is a simple mechanism by which Pu(VI) could be reduced by a ferrihydrite surface. Plutonium redox potentials are on the order of 1 V [21]. Many semiconductors have a conduction band above this, so the electron transfer is potentially thermodynamically possible [48, 166]. Unfortunately, the band edge position of ferrihydrite is not recorded in the literature, but its ability to reduce Pu(VI) gives an upper

bound for the ferrihydrite band edge. A second possibility is that Fe(II) is produced at the surface of ferrihydrite, which then interacts in solution with the Pu(VI) (and then Pu(V)) to reduce to Pu(V) (and then Pu(IV)) and recreate Fe(III). This is the more likely mechanism at low pH where the plutonium(VI) will not readily interact with a positively-charged surface.

The interesting topic then becomes why only the dried form of the ferrihydrite shows any significant photocatalytic activity at pH 4. As mentioned in Section 3.3, quantum size effects likely play a role for the suspended ferrihydrite, widening the band gap to an estimated energy of around 4 eV. This decreases the wavelength necessary to excite an electron to the conduction band to around 310 nm, which is below the primary fluorescent lamp spectrum and would only be excited by the remaining mercury peaks in the UV region. However, the mercury lines between 300 and 350 nm are not very intense, and thus there would be a much smaller intensity of light incident on the sample capable of exciting an electron in the suspended ferrihydrite, greatly decreasing the overall electron yield. Additionally, because ferrihydrite is relatively amorphous, the overall charge carrier transport efficiency is likely to be low, and this efficiency is certain to be lower prior to drying. Because goethite is much more crystalline, the efficiency of charge carrier transport would increase, which may suggest an explanation for the high photocatalytic activity of the suspended "ferri-goethite." The suspended "ferri-goethite" is also not likely to experience quantum size effects, so the band gap is likely to remain in the energy excited by visible light. Although the value for the effective relative electron mass for colloidal goethite is not recorded, using the same value of 0.27 used for ferrihydrite and a relative effective mass of 15 [149] gives a Bohr radius of 29.9 Å, which is smaller than the suspended "ferri-goethite" particles (≈5 nm). It is also known that nanoparticle photocatalysis will increase with increasing particle size [16].

Oxygen vacancies are several times as likely to be a site for vapor deposited metal clusters to bind or begin nucleation [109], so it is reasonable to assume that they might also be places of high reactivity for the binding of plutonium in solution. The excess electron density in an oxygen vacancy would attract a positively-charged plutonyl molecule, possibly even on an overall negatively charged surface, at least long enough to transfer one or more of the excess electrons to the plutonium. A less ordered surface is more likely to have more oxygen vacancies, and oxygen vacancies on SiO_2 surfaces consist of the two extra electrons being trapped in an Si-Si bond rather than contributing to free electron density [109]. Thus, the mesoporous ferrihydrite likely has many fewer oxygen vacancies than dried ferrihydrite, possibly explaining the higher reactivity of dried ferrihydrite over the mesoporous ferrihydrite. This may be supported by the fact that although they have the same XRD pattern, the two materials are of slightly different colors, the mesoporous ferrihydrite being of a redder hue, meaning that it absorbs more green light. Oxygen vacancies can also change the color of a material [109], and could be a possible reason for both the color and reactivity differences.

The mesoporous ferrihydrite should have a band gap similar to that of the dried ferrihydrite and hematite based on the synthesis. There may be slight differences based on structural differences from the thermal decomposition, but because most iron oxides have been measured to have similar band gaps, there is no reason to expect that the mesoporous ferrihydrite should differ significantly. However, the more important difference between the two approaches is that the nanocasting method leaves behind some of the silica template on the ferrihydrite surface, in some cases up to 20 atom % and averaging around 2-6 % as measured by EDS (see Section 5.4). Silica (SiO_2) is well known as an insulator, and its

presence on the ferrihydrite surface is likely to interfere with surface transfer of electrons even if a large number of electron-hole pairs are formed. The silica may also interfere with the solubilization of Fe(II), potentially eliminating the reductant from solution. Given the data presented in Section 5.9.6, this second possibility seems the more likely one.

These factors explain the observations seen in Figures 5.33 to 5.41 and highlight the differences between three materials that are often considered to be the same. The dried ferrihydrite and the suspended "ferri-goethite" both have band gaps at the appropriate energy, a high enough surface reactivity to interact well with the plutonium in solution, and nothing hindering the transfer of electrons to the plutonium. The suspended ferrihydrite, on the other hand, likely experiences quantum size effects that shift the band gap outside the range of emission of the glovebox lights and a higher degree of disorder to cause the recombination of any electron-hole pairs produced by higher energy mercury lines. The mesoporous ferrihydrite is likely to produce a sufficient number of electron-hole pairs, but also has a lower surface reactivity and a thin covering of an insulator to limit the ability to transfer any of those electrons to the plutonium.

5.9.4 Plutonium Uptake Capacity Measurements

After the determination of the average sorption curves for the three materials (dried, suspended, and mesoporous ferrihydrite), the pH corresponding to the maximum sorption was chosen for further investigation at a higher Pu(VI) concentration. In each material the sorption at the maximum was nearly 100 %, implying that the true capacity could be much higher and further testing was necessary.

Unfortunately, a true capacity or saturation coverage measurement for plutonium sorption is a complicated experimental problem. Plutonium solubility is a limiting factor, particularly at higher pH values around pH 8 and pH 9 where these materials exhibit their maximum sorption. Plutonium(VI) is only soluble to the micromolar range (see Figure 2.3, although the effective solubility has been seen to increase in the presence of a solid or carbonate, so there is a fine line between sorption and precipitation. Not only do the kinetics of sorption need to be relatively fast, the amount of plutonium put into solution cannot greatly exceed the sorption capacity of the solid. One might therefore assume that adding repeated smaller quantities of plutonium until the sorption does not reach 100 % anymore would be a more appropriate method of measurement where at least the sorption could be assured over the possibility of precipitation due to exceeding the solubility. While this is a valid approach, past experience in our laboratory has shown that often materials will only bind 60-80 % of the added plutonium(VI) for each consecutive addition, so waiting for 100 % sorption before adding another aliquot might not be reasonable. This is likely a kinetic effect; as the concentration in solution decreases due to sorption, the probability that a plutonium ion in solution will encounter a free surface site decreases drastically. However, if experiments are prolonged significantly to ensure that the solid has ample time to bind each added aliquot, then the average oxidation state begins to decrease (see Section 2.4). So, a true capacity measurement for Pu(VI) is very difficult by either of these methods.

Thus, the experiments described here are not intended to be full capacity measurements. A set concentration was chosen, added as a single aliquot, and the resulting solution concentration measured at a set time after. This experiment was intended to hopefully measure

Material	pH_{24h}	% Bound 24 h	% Bound 120 h	pH_{120h}
Dried	7.6	92 ± 12	93 ± 12	7.7
Suspended	7.9	95 ± 12	94 ± 12	7.8
Mesoporous	8.2	80 ± 11	80 ± 11	8.6

Table 5.5: Percent of plutonium bound to the solid. Initial loading was 99 ± 10 μM Pu(VI) on 8 mg of dried and suspended ferrihydrite and 13 mg of mesoporous ferrihydrite in 8 mL. pH_{24h} and pH_{120h} refer to the measured pH at 24 and 120 hours, respectively.

Material	pH_{24h}	Loaded	mg/g - 24 h	mg/g - 120 h	pH_{120h}
Dried	7.6	23 ± 2	22 ± 3	22 ± 3	7.7
Suspended	7.9	24 ± 2	23 ± 3	22 ± 3	7.8
Mesoporous	8.2	15 ± 1	12 ± 2	12 ± 2	8.6

Table 5.6: Amount of plutonium bound to the solid in milligrams of Pu per gram of solid. pH_{24h} and pH_{120h} refer to the measured pH at 24 and 120 hours, respectively.

the capacity, but at worst at least get a lower bound for the capacity at the pH of maximum sorption.

Inspection of the sorption curves for each material (see Figures 5.28, 5.29, and 5.30) shows that the pH of maximum sorption is near pH 8 for the nanoparticulate ferrihydrite (both dried and suspended) and closer to pH 8.9 for the mesoporous ferrihydrite. These pH values were chosen for the solution pH. To truly compare the binding strength of the materials and not just the surface area, the amount of solid added to each solution was normalized to surface area rather than mass. This led to using 8 mg of dried and 13 mg of mesoporous ferrihydrite in 8 mL. Unfortunately, the suspended ferrihydrite surface area is not known, so 8 mg was used for that material as well. This means that the solution to solid ratio for the mesoporous ferrihydrite is no longer 1 g/L, but it was more desirable to have the same surface area and same plutonium concentration than to have the same solution to solid ratio. All solutions were 0.1 M $NaClO_4$ and loaded with sufficient plutonium to reach 99 ± 10 μM Pu(VI). This value was more than six times the previous maximum concentration tested of 16 μM Pu(VI). Aliquots were removed after 1 day and 5 days for measurement by LSC. Results of these experiments are shown in Tables 5.5 and 5.6.

The suspended ferrihydrite is expected to have a higher capacity than the dried [46]. The amount of plutonium bound to the surface of the nanoparticulate ferrihydrite is very close to the amount loaded (92 ± 12 % for the dried and 95 ± 12 % for the suspended), suggesting that at this concentration the surface is not yet saturated. It is also unlikely that this is due to precipitation because there was a larger amount of plutonium left in solution in both the mesoporous ferrihydrite sample and in other experiments at higher pH conditions. It can be stated that the capacity of the dried ferrihydrite is at least 22 ± 3 milligrams of Pu(VI) per gram of solid, and that the capacity of the suspended ferrihydrite capacity is at least 23 ± 3 mg/g (Table 5.6).

The mesoporous ferrihydrite, on the other hand, may have reached its capacity, as only 80 ± 11 % bound. The amount remaining in solution is still less than the concentrations found at higher pH conditions, so it is again unlikely that this is due to precipitation. This result again highlights the differences in surface chemistry that arise from a very different synthetic technique. Not only is the point of zero charge significantly higher (Section 5.8), the plutonium affinity for equal surface area is significantly lower. This lower capacity unfortunately hampers the strength of the mesoporous ferrihydrite as a plutonium sorbent. Although 12 ± 2 mg Pu(VI) per gram of ferrihydrite is a decent capacity, the fact that the nanoparticulate ferrihydrite capacity is so much higher means that the current mesoporous form is not the best for the ferrihydrite. Perhaps the formation of mesoporous ferrihydrite from a joint precipitation-nanocasting method that would yield a more similar surface to the nanoparticulate would produce a material both ordered in structure and with a more reactive surface.

5.9.5 Desorption Measurements

Several samples where the sorption portion of the experiment was completed after only 5 days were chosen for desorption experiments to determine how much of the plutonium sorption was reversible. It was important to choose "young" samples in order to determine the desorption characteristics of Pu(VI) from ferrihydrite rather than the other more reduced oxidation states that would be in solution with increasing sample age.

For the desorption experiments, samples in equilibrium at pH values between 6 and 10 and containing a Pu(VI) concentration of either 16 or 99 μM were brought to a pH between 2.49 and 2.60 for 24 hours and the Pu concentration measured again by LSC. A lower pH risked dissolving the ferrihydrite, and a higher pH risked sorption, so 2.5 was chosen as a middle ground. The results of these experiments are shown in Table 5.7. Overall, the sorption of plutonium on these three materials was reversible, although small amounts plutonium did remain bound to the surface after 24 hours. The amount remaining on the surface was greatest for the dried ferrihydrite, which is consistent with the greater aggregation expected for that material [46], although it was not significantly higher than the amount remaining on the suspended ferrihydrite for these concentrations. This suggests that the binding to the nanoparticulate ferrihydrite is stronger than the plutonium binding to the mesoporous ferrihydrite. Although all of the samples were held primarily in the dark, there may also be greater reduction of the Pu(VI) on the nanoparticulate ferrihydrite (see Section 5.9.3), which could influence the amount of Pu(VI) available for removal from the surface. The binding of Pu(IV) is likely stronger and thus Pu(IV) is more likely to remain on the surface even under acidic conditions.

These results suggest that the mesoporous ferrihydrite may be more suited to applications where the recovery of 100 % of the Pu is required, but the capacity need not be as high. On the other hand, the high sorption, light-induced reduction, lower desorption of Pu(VI) on dried ferrihydrite, tied to the much higher levels of aggregation, could make dried ferrihydrite a great sequestering agent for plutonium. It is also environmentally friendly and relatively inexpensive.

Material	pH_i	Pu(VI) Loaded	Initial Binding	Left After Desorp.	pH_f
Dried	7.68	0.79 ± 0.08	0.7 ± 0.1	0.07 ± 0.08	2.57
Dried	7.73	0.79 ± 0.08	0.7 ± 0.1	0.05 ± 0.08	2.53
Dried	5.95	0.13 ± 0.01	0.06 ± 0.02	0.03 ± 0.01	2.54
Dried	9.05	0.13 ± 0.01	0.04 ± 0.02	0.01 ± 0.01	2.58
Dried	10.01	0.13 ± 0.01	0.02 ± 0.01	0.01 ± 0.01	2.55
Suspended	7.74	0.79 ± 0.08	0.8 ± 0.1	0.05 ± 0.09	2.57
Suspended	7.76	0.79 ± 0.08	0.8 ± 0.1	0.04 ± 0.09	2.58
Suspended	9.04	0.13 ± 0.01	0.05 ± 0.01	0.00 ± 0.01	2.57
Suspended	10.00	0.13 ± 0.01	0.03 ± 0.01	0.00 ± 0.01	2.56
Mesoporous	8.53	0.79 ± 0.08	0.6 ± 0.1	0.01 ± 0.09	2.59
Mesoporous	8.68	0.79 ± 0.08	0.6 ± 0.1	0.00 ± 0.09	2.60
Mesoporous	6.41	0.13 ± 0.01	0.03 ± 0.01	0.01 ± 0.01	2.49
Mesoporous	7.32	0.13 ± 0.01	0.09 ± 0.02	0.03 ± 0.01	2.57
Mesoporous	7.98	0.13 ± 0.01	0.11 ± 0.02	0.03 ± 0.01	2.57

Table 5.7: Amount of plutonium bound to the solid before and after treatment with acid to remove the plutonium. All Pu(VI) concentrations are listed in micromoles.

5.9.6 XAS Measurements

X-ray absorption spectroscopy (XAS) includes multiple different techniques, including X-ray absorption near edge structure (XANES) and extended X-ray absorption fine structure (EXAFS). Both of these techniques are contained within one spectrum, but at different energy regions within that spectrum (see Figure 5.43). High-energy X-rays produced by accelerated electrons from a synchrotron are sent through a monochromator and are directed to the sample. When these X-rays are of a sufficient energy, they eject a particular core electron, giving what is called the absorption edge. For plutonium, we use the L_{III} edge, which corresponds to the $2p^{(3/2)}$ electron and is at 18062.3 eV. When the photoelectron is ejected, it interacts with the electrons of the surrounding atoms, creating oscillations in the resulting spectrum from the scattering. Data are displayed as absorption as a function of energy for XANES and as the Fourier transform for EXAFS. The XANES region extends from before the absorption edge to about 50 eV above the edge. Because the exact energy of the absorption edge is dependent on the electronic structure of the atom, XANES is used to identify the oxidation state. The oscillations caused by interactions with the surrounding atoms at increasing energies make up the EXAFS region and can be used for information about the coordination environment around the element of interest when compared to model complexes. The distance between these oscillations indicates the distance to neighboring atoms, while the amplitude of the oscillations is representative of the number of neighboring atoms. It should be noted that XAS does not allow for the calculation of geometries and oxidation states without comparison to standards and model complexes. [92]

Samples prepared for measurement by XAS were prepared in a similar fashion to the sorption samples. Approximately 100 mg of sample (50 mg for the suspended ferrihydrite)

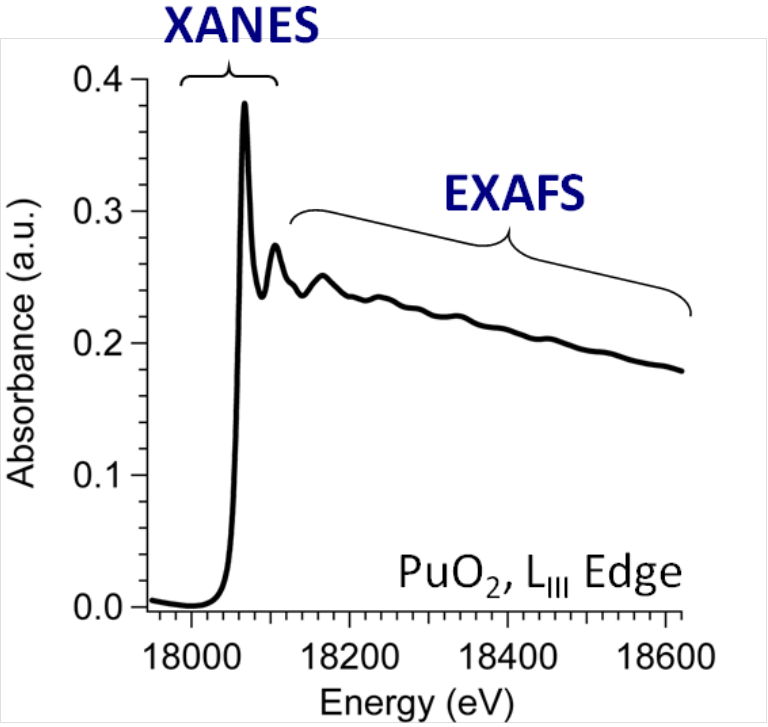


Figure 5.43: Representative Pu L_{III} edge XAS spectrum with the XANES and EXAFS regions labeled. Courtesy of D. L. Wang.

was added to 8 mL of 0.1 M $NaClO_4$ and the pH adjusted before the addition of approximately 0.25-0.30 mg of Pu(VI). The solutions were quickly pH adjusted with NaOH and $HClO_4$ and allowed to sit on a rocker for 2-4 days. The pH was checked and maintained daily. Samples were opened to air and no effort was made to exclude carbonate. The day before transport to the beamline, the samples were assayed with LSC, the pH measured, and a portion of the solid removed into the sample holder (see the thesis of Yung-Jin Hu [61] for details). The solid was triply contained for transport to the Stanford Synchrotron Radiation Lightsource (SSRL) for XAS measurements. All samples were measured within 7 days of adding the plutonium, which was always verified by UV-visible spectroscopy to be Pu(VI), so alpha particle-induced reduction should not be a significant factor in any of the results.

All measurements were taken on beamline 11-2 at SSRL and maintained at 30 K using a liquid helium flow cryostat. All samples were only exposed to the X-ray beam once the temperature in the cryostat was at 50 K or below to prevent beam-induced chemistry [63]. Spectra were collected using a 50 % detuned Si(220) $\phi - 0°$ double-crystal monochromator in fluorescence mode using a 32-element germanium detector. Fourteen scans of each sample were collected and then averaged, with the exception of the dark sample that was measured again after light exposure. The spectra were then dead-time corrected and energy calibrated by setting the first inflection point of the L_{III} edge of a $^{242}PuO_2$ reference sample to be 18062.3 eV. XANES were fit using a least-squares method to normalized Pu reference spectra (Figure 5.44) to determine the percentage contribution from each oxidation state [22, 110]. Results are shown in Table 5.8. The error displayed was estimated by an inversion of the covariance matrix, and the calculated percentages were not constrained to add to 100 %. Further data analysis will not be discussed here, as the process was carried out by Deborah L. Wang. More information can be found in the thesis of Yung-Jin Hu (2011) [61].

Most of these samples were prepared and measured with full exposure to laboratory lighting. The exception is one sample of dried ferrihydrite, which was prepared and transported with minimal exposure to light. Once it had been measured, the sample was then exposed to light for the remainder of the experimental run, and was measured again 2 days later to confirm that under exposure to light the material would cause the same chemistry that was observed for the other dried ferrihydrite sample. All other samples were only measured once.

The results of the XANES measurements of the three ferrihydrite materials are presented in Table 5.8. The fits of the standards to the experimental data are shown for the pH 7.77 dried ferrihydrite in the dark and after light exposure (Figures 5.45 and 5.46) and for the pH 7.88 dried ferrihydrite exposed to light (Figure 5.47). The fits for the other samples are not shown for brevity.

There are some important trends visible in the data presented in Table 5.8, which will be discussed by material rather than by pH or light exposure.

The dried ferrihydrite showed a significant increase in the amount of Pu(IV) with exposure to light. The sample held in the dark still shows some Pu(IV), but this is likely due to the fact that the sample was not able to be loaded and transported entirely in the dark. Unfortunately, the amount of light exposure was not able to be measured, as the most likely exposure would have occurred during shipment when the samples were under the control of other laboratory personnel. However, the difference between the dark and light samples is clear, and the sample originally held in the dark showed a significant gain in Pu(IV) during the two days of exposure to light at the beamline following the initial measurement. Finally,

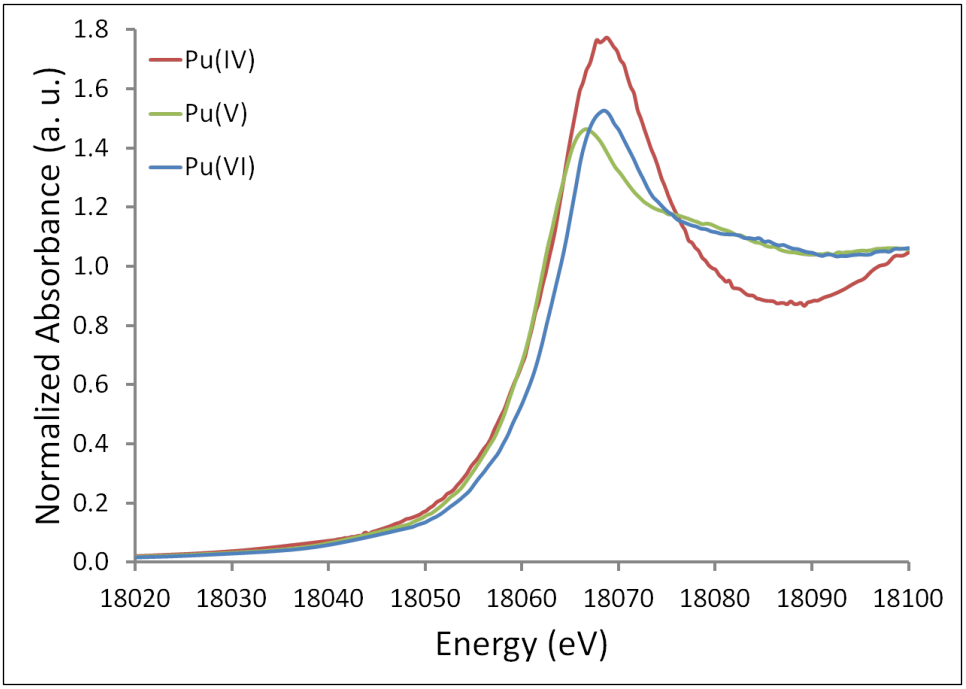


Figure 5.44: Standard XANES spectra used for fitting Pu(IV), Pu(V), and Pu(VI) during XAS data processing. The shoulder from about 18070 to 18090 eV caused by scattering from the axial oxygens is clearly visible for Pu(V) and Pu(VI), and missing for Pu(IV). The edge shift based on oxidation state is also visible. [22, 110]

Material	**pH**	**% Pu(IV)**	**% Pu(V)**	**%Pu(VI)**	**mg Pu(IV)**
Dried Light	4.14	78 ± 1	17 ± 1	6 ± 1	0.039
Dried Dark	7.77	9 ± 1	49 ± 2	41 ± 2	0.025
Dried Dark After Light	7.77	12 ± 1	38 ± 2	50 ± 2	0.032
Dried Light	7.88	14 ± 1	47 ± 2	38 ± 2	0.038
Suspended Light	5.70	54 ± 1	41 ± 1	6 ± 1	0.135
Suspended Light	7.94	76 ± 2	26 ± 3	0 ± 3	0.211
Mesoporous Light	7.48	10 ± 2	25 ± 1	66 ± 1	0.029
Mesoporous Light	8.86	84 ± 2	19 ± 2	0 ± 2	0.247

Table 5.8: Percentage of Pu(IV), Pu(V), and Pu(VI) determined from least-squares fitting of Pu L_{III} data. The "Dark" and "Light" labels indicate if the sample was exposed to laboratory lights or not. The mg of Pu(IV) is calculated based on the percent shown here and the amount of Pu bound to the surface.

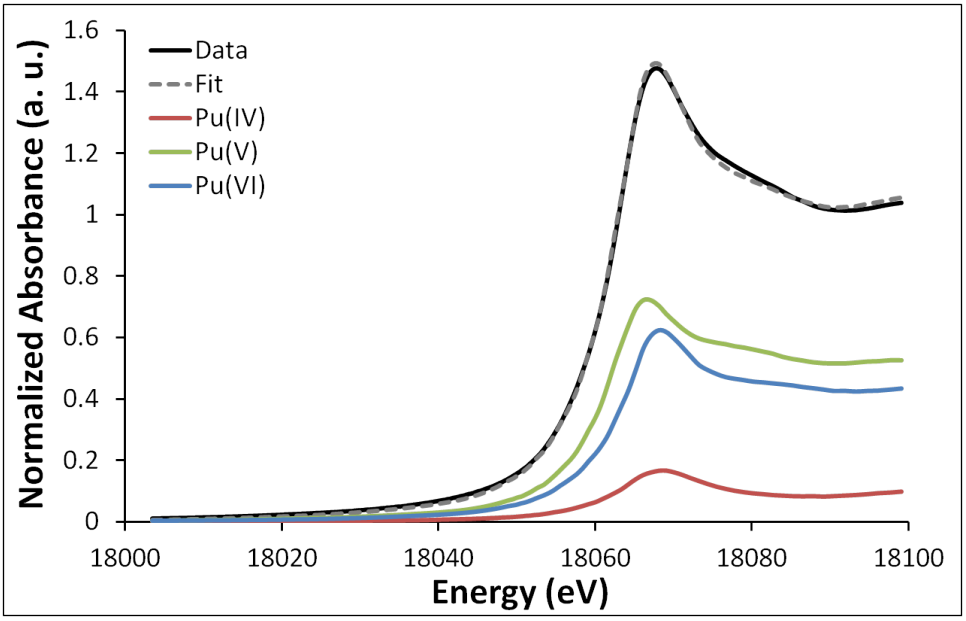


Figure 5.45: Fit of experimental XANES data to Pu(IV), Pu(V), and Pu(VI) standard XANES spectra for dried ferrihydrite at pH 7.77, which was kept in the dark as much as possible.

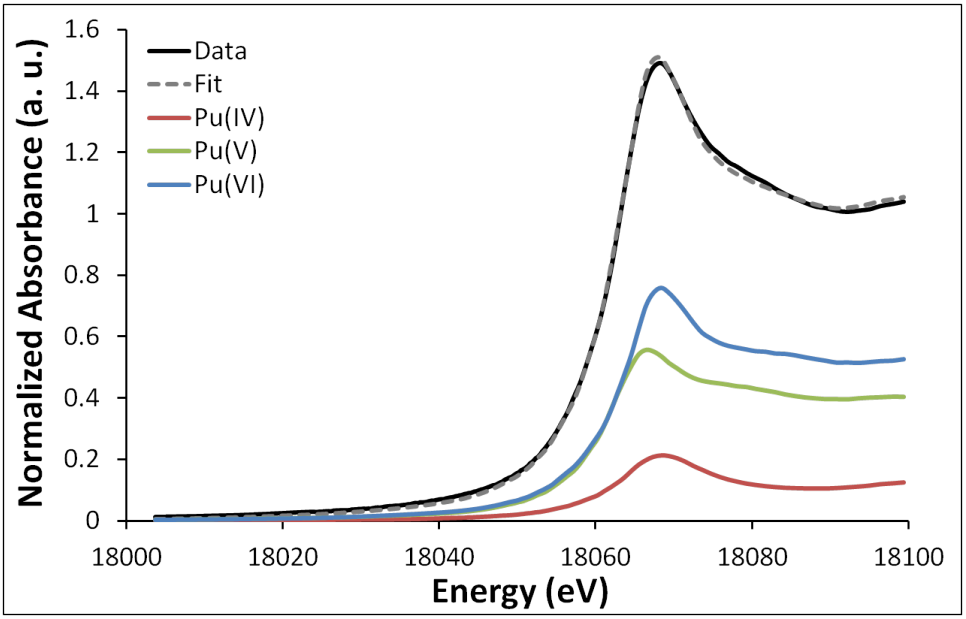


Figure 5.46: Fit of experimental XANES data to Pu(IV), Pu(V), and Pu(VI) standard XANES spectra for dried ferrihydrite at pH 7.77 after exposure to light (after previously limiting light exposure as much as possible).

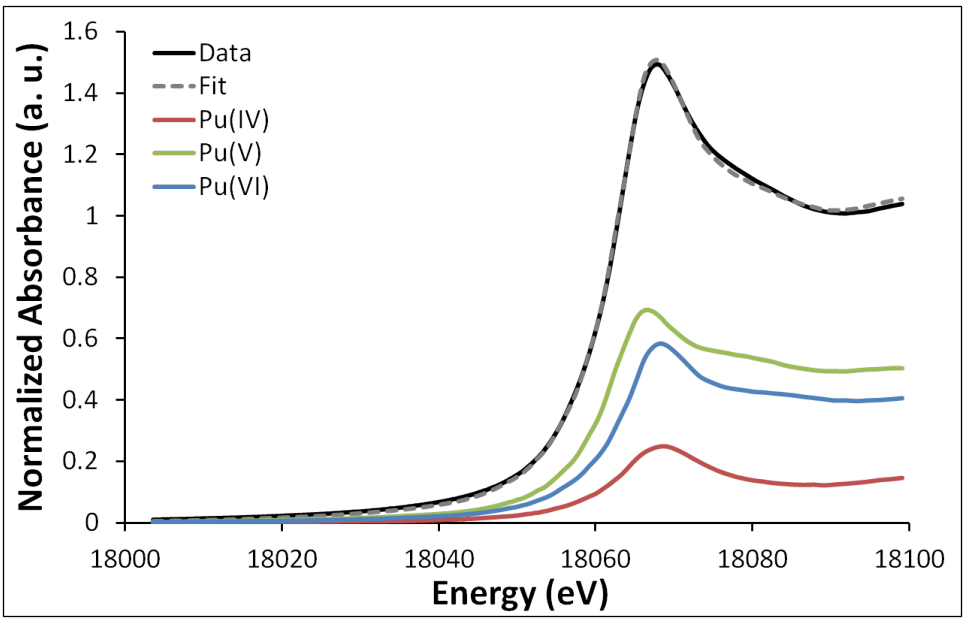


Figure 5.47: Fit of experimental XANES data to Pu(IV), Pu(V), and Pu(VI) standard XANES spectra for dried ferrihydrite at pH 7.88, which was exposed to light as much as possible.

the overall amount of plutonium reduced to Pu(IV) was nearly the same for the pH 4.14 and pH 7.88 samples; the percentages differ considerably because although the same amount of Pu was added to the solutions, the sorption at pH 4 is likely to be very low unless it has reduced to Pu(IV) (see Section 5.9.3). This highlights an important factor that must be considered when looking at other ferrihydrite or iron oxide results. XAS data is normally only taken on samples with high plutonium uptake to guarantee that a large enough amount of Pu is present to give a good fluorescence signal. However, the downside of using samples with such high uptake is that a slow rate of light-induced Pu reduction would not be a high percentage of the total Pu, and thus would likely not be noticed in the data. Leaving samples longer before measurement could increase the amount of Pu(IV) whose creation is from photochemistry, but it would also increase the amount of alpha particle-induced reduction (Section 2.4). Therefore, if photochemistry is suspected, lower plutonium amounts bound to the surface should be compared to the samples with higher amounts loaded.

The results for the suspended ferrihydrite differ from the batch experiment results, showing a much higher proportion of Pu(IV) than was expected based on the weak photochemistry at pH 4. However, these samples are at a higher pH than those presented in Section 5.9.3, and the increase in Pu(IV) does appear to be pH dependent. Unfortunately the sorption at pH 6-8 for Pu(VI) is high enough that batch experiment results would not show a difference between binding of Pu(VI) and binding of Pu(IV); for that differentiation, XANES data is necessary. The XANES results do not necessarily contradict the batch data or discussion, however. It is well known that increasing the pH of suspended ferrihydrite causes further aggregation [46], and this likely also causes an increase in the crystallinity. This increase could significantly change the band gap properties of the suspended ferrihydrite,

reducing both the band gap and the electron-hole recombination rate enough to cause the photo-induced reduction of Pu(VI) to occur. This is evident in the batch sorption results of the "ferri-goethite" samples in Section 5.9.3. Assuming that all of the Pu bound in the pH 4 batch experiments was Pu(IV), that would correspond to approximately 0.001 mg of Pu(IV). While this is significantly less than the amount of Pu(IV) at pH 5.70 and 7.94, it is not unreasonable to expect significant changes in the ferrihydrite aggregation with that significant of a pH increase.

The more important question is why the suspended ferrihydrite had such a greater amount of Pu(IV) than the dried ferrihydrite. This is likely due to surface area, which is likely far greater for the suspended ferrihydrite than it is for the dried ferrihydrite (Section 5.7.4). Once the band gap has changed to an energy in line with fluorescent lighting, the larger surface area and the well-dispersed particles would greatly increase the interaction with the plutonium and thus the ability to transfer an electron. The dried ferrihydrite would not show this pH dependence because the particles are already aggregated when added to even the low pH solutions. Additionally, it is unlikely that the Pu(VI) speciation plays a role under pH 8 because no differences were seen between the behavior of the dried at pH 4.14 and at pH 7.88.

The mesoporous ferrihydrite showed unexpectedly high amounts of Pu(IV) as well, particularly for the pH 8.86 sample. While these results were unexpected, they are not unexplainable, and there are several explanations that may apply. A strong explanation for the reduction to Pu(IV) when sorption experiments at pH 4 showed none stems from the presence of silica in the sample. EDS measurements showed that silica is still present in non-negligible quantities on the surface of the pores. Hu *et al.* (in preparation) [63] showed clearly that X-ray beam-induced reduction of Pu(VI) to Pu(IV) is quite significant in the presence of silica. Therefore, it is unclear if the large amount of Pu(IV) on the mesoporous ferrihydrite samples is from chemistry prior to beam exposure, or if it is caused by the X-ray beam.

However, there is still a clear pH dependence for the behavior of the mesoporous ferrihydrite. There are several options to explain this behavior. It is possible that pH 4 was too low of a pH for the mesoporous ferrihydrite to show light-induced sorption. The PZC of the mesoporous ferrihydrite is so much higher than that of the nanoparticulate ferrihydrite that it is possible that the mesoporous ferrihydrite surface is so positively charged at pH 4 that the plutonium will not interact at all to undergo electron transfer. It is also possible, as mentioned in Section 5.9.3 that the silica prevents the solubilization of Fe(II) from the ferrihydrite surface, ensuring that no Pu(VI) reduction would occur in solution. Because the sorption of Pu(VI) to mesoporous ferrihydrite increases drastically from pH 4 to the maximum described here of pH 8.86, it is not unreasonable to assume that the amount of reduction would also increase. If no Fe(II) is available in solution, the only possible mechanism for Pu(IV) reduction is through binding to the surface. The greater the sorption, the greater the Pu reduction. Thus, these results suggest that the silica does not interfere with electron transfer, but only with the release of Fe(II) into solution.

Based on these discussions, it is likely that the reduction on the mesoporous ferrihydrite is a combination of both a small contribution from beam-induced chemistry and a larger contribution from the increased sorption with increasing pH. This would indicate that the band gap of the mesoporous ferrihydrite is likely to be similar to that of the dried nanoparticulate

ferrihydrite, but it further confirms that the two materials act differently in solution. It is particularly notable that the dried ferrihydrite does not reach the same levels of reduction as the mesoporous ferrihydrite (the amount of reduction does not increase with increasing pH only because the dried ferrihydrite actually exhibits photochemistry at low pH and not just high pH). One factor may be the contribution from the beam-induced chemistry just discussed. Another factor may be the differences in particle morphology of the two materials. When an electron-hole pair is created, the electron must be transported to the surface of the particle to either release a Fe(II) ion or be transfered to a Pu(IV) molecule. The particle sizes are not significantly different between the two materials (Section 5.5), but the mesoporous ferrihydrite is filled with pores. This means that an electron would have to travel a significantly smaller distance to reach a surface of the mesoporous ferrihydrite as it would to reach a surface in the dried ferrihydrite. Once the mesoporous ferrihydrite is put into conditions where the surface electron transfer process is possible, the shorter electron travel distance would greatly increase the efficiency of the surface electron transfer, causing a much larger amount of Pu(IV) to be produced.

The data in Table 5.8 are an important addition to the data in Sections 5.9.2 and 5.9.3, and further elucidate the behavior of these three materials. All three ferrihydrite materials can act as photocatalysts for the reduction of Pu(VI) to Pu(IV), but under different solution conditions that affect the material properties or the reduction mechanism. Although none of these data are proof of the suggested mechanisms, there is no doubt that the photochemistry exists.

There is also the possibility that the presence of Pu(IV) was caused by precipitation during the experiment. Most of these samples were in relatively high pH conditions, and the addition of too much base too quickly after the plutonium addition can cause the immediate precipitation of Pu(IV). To rule out this possibility, the EXAFS region of the data needs to be analyzed. A Fourier transform of the raw data will give an indication of the coordination shells, as coordinating atoms cause the scattering that gives rise to the EXAFS oscillations. If the Pu had precipitated to the surface in any significant quantity, there would be a Pu-Pu scattering path at about 3.9 Å. This analysis will need to be made to confirm that no significant amount of Pu precipitated to the surface, and that the reduction seen is legitimate chemistry and not an experimental error. Although this analysis is still underway, no precipitation is expected for these samples. For further data and discussion on this topic the reader is referred to [10].

Chapter 6

Conclusions

6.1 Final Remarks

The work presented in this thesis represents a significant step forward in the understanding of 2-line ferrihydrite, particularly with respect to its interactions with plutonium. Although there is often little distinction in the literature between the chemistry of suspensions of ferrihydrite that have never been dried and suspensions created by adding dried ferrihydrite back into solution, the results presented in Chapter 5 clearly indicate that these two must be considered separately. Although both materials showed high plutonium uptake and a very similar sorption envelope, they showed very different light-induced chemistry. The fact that the suspended ferrihydrite experiences quantum size effects may also cause there to be even greater differences in reactivity, electronic properties, and overall behavior when compared to the dried ferrihydrite, particularly at low pH. Researchers must be cognizant of how these two materials differ.

The light-induced chemistry also has important implications for how future experiments involving ferrihydrite and other redox active species should be designed, and how the data from past experiments should be considered. The discovery of the photocatalysis for Pu reduction was more of an unintended consequence than a direct aim of the original research, and other researchers may have seen effects of this sort without realizing it. The fact that it will occur under general laboratory lighting and that a high powered lamp is not required means that care should be taken in future research to control the light exposure when not attempting to investigate the role of the surface electron transfer. It is also noteworthy that the photocatalysis can be greatly affected by the solution pH depending on the material in question and the mechanism by which the electron transfer to the plutonium occurs.

Another interesting result of these studies is that the mesoporous ferrihydrite actually has a lower surface area and a lower apparent surface reactivity than the dried nanoparticulate ferrihydrite, making its use as a sorbent questionable. However, the fact that this work has shown that the synthesis method between the mesoporous ferrihydrite and dried ferrihydrite (thermal decomposition versus precipitation) yields materials with very different properties, the differences in surface reactivity may be accounted for. Thus, this work does not preclude the successful implementation of a mesoporous ferrihydrite for use in a through-process. However, this ferrihydrite likely must be made by precipitation in order to have the same

high surface reactivity. The synthesis routes of Smith *et al.* [139], Xia *et al.* [177], and Khaleel [71] offer some promising characteristics toward a better mesoporous ferrihydrite synthesis that would have both the regular pore structure and the high surface reactivity.

6.2 Future Work

There are many avenues down which continuations of the work presented here can be pursued. Described here are just a few of these avenues that may have the greatest potential for gain to the scientific community, in the humble opinion of the author.

With respect to the manganese-substituted goethite, it would be of great interest to pursue a technique like laser ablation ICP-MS rather than the the kinetics of particle dissolution. With laser ablation ICP-MS one could be sure to obtain the concentration of iron and manganese as a true function of the depth into the particle rather than confounding the measurement by detaching crystallites before dissolving them. When performed on a variety of substitution percentages and particle sizes, this type of experiment would greatly improve the understanding of elemental substitution and particle formation. This could be paired with both XPS and EDAX measurements as well.

There are a far greater number of interesting experiments relating to ferrihydrite. The first relate to the material itself. As mentioned in Section 5.3.2, the mesoporous ferrihydrite is formed by thermal decomposition rather than forced precipitation, and this leads to a lower level of surface reactivity, as described in Section 5.9.4. The synthesis of a precipitated mesoporous ferrihydrite may allow for the high reactivity of the nanoparticulate material, but in a more regular and larger-scale particle that would be easier to manipulate for through-processes. It is not unreasonable to assume that this could still be nanocast, but it could also more closely relate to the syntheses of Khaleel [71] and Xia [177]. The synthesis of Smith *et al.* [139] is also promising. Additionally, the role of both particle structure and silica percentage has yet to be fully determined for ferrihydrite. The ferrihydrite used over the course of this work was unusually stable with respect to aging, and it would be very informative for the future use of ferrihydrite to determine what caused such stability and if that cause could be further exploited. It is well known that the presence of silica slows or prevents aging, but it would be interesting to determine if there is a cut-off percentage below which aging still occurs. A simple synthesis variation and long-term XRD study could answer this question.

The surface of ferrihydrite also could use further characterization. The point of zero charge was only really measured with powder addition (Section 5.8), but there are many other techniques available. For example, minimal efforts were made here to use potentiometric titration and mass titration; these efforts could easily be expanded. Zeta potential measurements could also be made. It would be informative to see how well these different PZC measurements line up to fully understand the surface interactions. Surface area is also an area needing further investigation. The use of other techniques beside nitrogen adsorption, such as EGME adsorption or potentiometric titration against standards, would be helpful in determining what the surface and pore structure look like. Additionally, an actual measurement of the suspended ferrihydrite surface area would be completely new. The area has been calculated, but perhaps an unconventional method like potentiometric

titration would allow for a measurement. Methylene blue adsorption showed promise, but was unfortunately flawed due to the large size of the dye in comparison to the ferrihydrite particle size. However, the methylene blue technique could be greatly bolstered for use by others by determining the smallest particle size that the methylene blue molecule will bind to, and to what extent the surface is covered by the dye. This could be accomplished through prudent use of a variable-sized material like ferrihydrite, a centrifuge, and a TEM.

There are also several missing pieces of information relating to the sorption of plutonium to ferrihydrite. For example, the shortest time scale measured in this work was approximately 24 hours because the goal was to measure equilibrium sorption properties, and it was clear that the majority of the sorption that was going to occur had already occurred by the time 24 hours had passed. It would therefore be prudent to measure the binding kinetics on much shorter time scales to see how the speed of binding changes as a function of the ferrihydrite material and the solution pH. The long-term behavior of the ferrihydrite-plutonium interface could also prove quite interesting. Ferrihydrite is known to cycle surface iron with solution iron when Fe(II) is present in solution (which is nearly all the time, at least in very small quantities). This means that over time a plutonium bound to the surface could gradually be incorporated into the center of the particle. Not only would this behavior provide an interesting insight into iron cycling and particle surface changes over time, an EXAFS study on the plutonium once it had been incorporated could provide very useful information about the ferrihydrite structure. There has been much debate in the literature about the structure of ferrihydrite, and EXAFS of a foreign atom incorporated into that structure could provide great insight.

Far more interesting is the obtainment of a greater understanding of the light-induced chemistry described in Section 5.9.3. To narrow down the band gap values for ferrihydrite, the sorption as a function of wavelength could be measured, provided suitable lamps were available. The most novel part of the experiment is the use of plutonium as a probe for ferrihydrite electronic structure. Further understanding of the relationship between the particle characteristics (size, crystallinity, etc.) could be obtained by synthesizing other related iron oxides, such as nanoparticulate suspended hematite, and submitting them to the same light and dark conditions for plutonium sorption. The behavior of these three materials should also be elucidated by performing light and dark batch experiments at a greater range of pH conditions, as well as XAS measurements on a wider variety of samples.

Potentially the most useful experiment for the application of ferrihydrite to an industrial process is the exploitation of the fast light-induced chemistry. For example, lanthanides and actinides that exist almost entirely in the trivalent state, such as americium or europium, will be soluble and will exist as the +3 cation in solution at pH 4. Due to the surface charge factors discussed in Section 5.9.2, no binding to the surface would be expected at pH 4. Because these elements are stable with respect to their oxidation state, the light-induced surface electron transfer that caused the Pu reduction described in Section 5.9.3 would not be a factor, and no oxidation state change that might cause precipitation or sorption would occur. Thus, there is a good possibility that a mixed solution of Pu and Am, for example, would be able to be separated by ferrihydrite exposed to the light at low pH. The plutonium would bind to the surface (if it is tetravalent, it will sorb and if it is a higher oxidation state, it would be reduced and then sorb), and the americium would remain in solution. The americium could be isolated by filtration of the solution. The stripping experiments in

Section 5.9.5 suggest that the plutonium may be removed relatively well from the ferrihydrite surface, meaning that the plutonium could also be recovered.

There are likely far more possible experiments to build upon the work presented here, but these are the experiments that the author, if presented with the opportunity to continue this line of research beyond graduate school, would choose to pursue.

Bibliography

[1] M. Alvarez, E. H. Rueda, and E. E. Sileo. Structural characterization and chemical reactivity of synthetic Mn-goethites and hematites. *Chemical Geology*, 231(4):288–299, 2006.

[2] M. Alvarez, E. H. Rueda, and E. E. Sileo. Simultaneous incorporation of Mn and Al in the goethite structure. *Geochimica Et Cosmochimica Acta*, 71(4):1009–1020, 2007.

[3] M. Alvarez, E. E. Sileo, and E. H. Rueda. Effect of Mn(II) incorporation on the transformation of ferrihydrite to goethite. *Chemical Geology*, 216(1-2):89–97, 2005.

[4] C. A. J. Appelo, M. J. J. Van Der Weiden, C. Tournassat, and L. Charlet. Surface complexation of ferrous iron and carbonate on ferrihydrite and the mobilization of arsenic. *Environmental Science & Technology*, 36:3096–3103, 2002.

[5] D. Armstrong. Measurement of ultra-pure water in the semiconductor industry. *www.waterworld.com*, 2008.

[6] J. R. Bargar, R. Reitmeyer, and J. A. Davis. Spectroscopic confirmation of uranium(VI)-carbonato adsorption complexes on hematite. *Environmental Science & Technology*, 33(14):2481–2484, 1999.

[7] J. R. Bargar, R. Reitmeyer, J. J. Lenhart, and J. A. Davis. Characterization of U(VI)-carbonato ternary complexes on hematite: EXAFS and electrophoretic mobility measurements. *Geochimica Et Cosmochimica Acta*, 64(16):2737–2749, 2000.

[8] R. Brina and A. de Battisti. Determination of the specific surface area of solids by means of adsorption data. *Journal of Chemical Education*, 64(2):175–176, 1987.

[9] L. Brinza, L. G. Benning, and P. J. Satham. Adsorption studies of Mo and V onto ferrihydrite. *Mineralogical Magazine*, 72(1):385–388, 2008.

[10] L. K. Brogan, D. L. Wang, and H. Nitsche. Interactions of Pu(VI) with nanoparticulate and mesoporous 2-line ferrihydrite. *Environmental Science & Technology*, In Preparation.

[11] S. Brunauer, P. H. Emmett, and E. Teller. Adsorption of gases in mulimolecular layers. *Journal of the American Chemical Society*, 60:309–319, 1938.

[12] K. Büppelmann, J. I. Kim, and C. Lierse. The redox-behaviour of plutonium in saline solution under radiolysis effects. *Radiochimica Acta*, 44-5:65–70, 1988.

[13] G. V. Buxton and R. M. Sellers. The radiation chemistry of metal ions in aqueous solution. *Coordination Chemistry Reviews*, 22:195–274, 1977.

[14] A. S. Campbell, U. Schwertmann, H. Stanjek, J. Friedl, A. Kyek, and P. A. Campbell. Si incorporation into hematite by heating Si-ferrihydrite. *Langmuir*, 18(21):7804–7809, 2002.

[15] L. Charlet and A. Manceau. X-ray absorption spectroscopic study of the sorption of Cr(III) at the oxide water inferface. II. Adsorption, coprecipitation, and surface precipitation on hydrous ferric-oxide. *Journal of Colloid and Interface Science*, 148:443–458, 1992.

[16] I. V. Chernyshova, S. Ponnurangam, and P. Somasundaran. On the origin of an unusual dependence of (bio)chemical reactivity of ferric hydroxides on nanoparticle size. *Physical Chemistry Chemical Physics*, 12(42):14045–14056, 2010 2010.

[17] G. R. Choppin. Redox speciation of plutonium in natural waters. *Journal of Radioanalytical and Nuclear Chemistry*, 147:109–116, 1991.

[18] G. R. Choppin, A. H. Bond, and P. M. Hromadka. Redox speciation of plutonium. *Journal of Radioanalytical and Nuclear Chemistry*, 219(2):203–210, 1997.

[19] G. R. Choppin, J.-O. Liljenzin, and Jan Rydberg. *Radiochemistry and Nuclear Chemistry*. Butterworth Heinemann, 3rd edition, 2002.

[20] D. L. Clark. The chemical complexities of plutonium. *Los Alamos Science*, 26:364–381, 2000.

[21] J. M. Cleveland. *The Chemistry of Plutonium*. American Nuclear Society, La Grange Park, IL, 2nd edition, 1979.

[22] S. D. Conradson. Application of X-ray absorption fine structure spectroscopy to materials and environmental science. *Applied Spectroscopy*, 52:252A–279A, 1998.

[23] J. Cornejo. The effect of heat treatment on textural evolution of ferrihydrite. *Materials Chemistry and Physics*, 15:369–377, 1986.

[24] J. Cornejo. Porosity evolution of thermally treated hydrous ferric-oxide gel. *Journal of Colloid and Interface Science*, 115(1):260–263, 1987.

[25] R. M. Cornell, A. M. Posner, and J. P. Quirk. Kinetics and mechanisms of acid dissolution of goethite alpha-FeOOH. *Journal of Inorganic & Nuclear Chemistry*, 38(3):563–567, 1976.

[26] R. M. Cornell and U. Schwertmann. *The iron oxides: structure, properties, reactions, occurrences and uses*. Wiley, 2003.

[27] E. Cristiano, Y.-J. Hu, M. Siegfried, D. Kaplan, and H. Nitsche. A comparison of point of zero charge measurement methodology. *Clays and Clay Minerals*, 59(2):107–115, 2011.

[28] T. Cseri, S. Bekassy, G. Kenessey, G. Liptay, and F. Figueras. Characterization of metal nitrates and clay supported metal nitrates by thermal analysis. *Thermochimica Acta*, 288(1-2):137–154, 1996.

[29] B. D. Cullity. *Elements of X-ray Diffraction*. Addison-Wesley, 2nd edition, 1978.

[30] K. Dardenne, T. Schafer, M. A. Denecke, J. Rothe, and J. I. Kim. Identification and characterization of sorbed lutetium species on 2-line ferrihydrite by sorption data modeling, TRLFS and EXAFS. *Radiochimica Acta*, 89(7):469–479, 2001.

[31] K. Dardenne, T. Schafer, P. Lindqvist-Reis, M. A. Denecke, M. Plaschke, J. Rothe, and J. I. Kim. Low temperature XAFS investigation on the lutetium binding changes during the 2-line ferrihydrite alteration process. *Environmental Science & Technology*, 36:5092–5099, 2002.

[32] G. M. Därr and U. Ludwig. Determination of the specific surface by adsorption from solution. *Materials and Structures*, 6:233–237, 1973.

[33] J. A. Davis and J. O. Leckie. Effect of adsorbed complexing ligands on trace metal uptake by hydrous oxides. *Environmental Science & Technology*, 12(12):1309–1315, 1978.

[34] J. A. Davis and J. O. Leckie. Surface ionization and complexation at the oxide-water interface. II. Surface properties of amorphous iron oxyhydroxide and adsorption of metal ions. *Journal of Colloid and Interface Science*, 67(1):90–107, 1978.

[35] J. H. de Boer. The BET-method. In D. H. Everett and R. H. Ottewill, editors, *Surface Area Determination*. International Union of Pure and Applied Chemistry, 1969.

[36] J. H. de Boer, B. C. Lippens, B. G. Linsen, J. C. P. Broekhoff, A. van den Heuvel, and Th. J. Osinga. The t-curve of multimolecular N_2-adsorption. *Journal of Colloid and Interface Science*, 21(4):405–414, 1966.

[37] M. C. Duff and C. Amrhein. Uranium(VI) adsorption on goethite and soil in carbonate solutions. *Soil Science Society of America Journal*, 60(5):1393–1400, 1996.

[38] L. Duraes, A. Moutinho, I. J. Seabra, B. F. O. Costa, H. C. de Sousa, and A. Portugal. Characterization of iron(III) oxide/hydroxide nanostructured materials produced by solgel technology based on the $Fe(NO_3)_{39}H_2OC_2H_5OHCH_3CHCH_2O$ system. *Materials Chemistry and Physics*, 130:548–560, 2011.

[39] D. A. Dzombak and F. M. M. Morel. *Surface Complexation Modeling: Hydrous Ferric Oxide*. John Wiley & Sons, New York, 1990.

[40] M. A. A. Elmasry, A. Gaber, and E. M. H. Khater. Thermal decomposition of Ni(II) and Fe(III) nitrates and their mixture. *Journal of Thermal Analysis and Calorimetry*, 52(2):489–495, 1998.

[41] Z. Feng, J. Zhao, F. E. Huggins, and G. P. Huffman. Agglomeration and phase-transition of a nanophase iron-oxide catalyst. *Journal of Catalysis*, 143(2):510–519, 1993.

[42] H. Foerstendorf, K. Heim, and A. Rossberg. The complexation of uranium(VI) and atmospherically derived CO_2 at the ferrihydrite-water interface probed by time-resolved vibrational spectroscopy. *Journal of Colloid and Interface Science*, 377:299–306, 2012.

[43] P. M. Fox, J. A. Davis, and J. M. Zachara. The effect of calcium on aqueous uranium(VI) speciation and adsorption to ferrihydrite and quartz. *Geochimica Et Cosmochimica Acta*, 70:1379–1387, 2006.

[44] U. G. Gasser, R. Nuesch, M. J. Singer, and E. Jeanroy. Distribution of manganese in synthetic goethite. *Clay Minerals*, 34(2):291–299, 1999.

[45] D. E. Giammar and J. G. Hering. Time scales for sorption-desorption and surface precipitation of uranyl on goethite. *Environmental Science & Technology*, 35(16):3332–3337, 2001.

[46] B. Gilbert, R. K. Ono, K. A. Ching, and C. S. Kim. The effects of nanoparticle aggregation processes on aggregate structure and metal uptake. *Journal of Colloid and Interface Science*, 339(2):285–295, 2009.

[47] D. C. Girvin, L. L. Ames, A. P. Schwab, and J. E. McGarrah. Neptunium adsorption on synthetic amorphous iron oxyhydroxide. *Journal of Colloid and Interface Science*, 141:67–78, 1991.

[48] M. Grätzel. *Heterogeneous Photochemical Electron Transfer*. CRC Press, Boca Raton, FL, 1989.

[49] S. J. Gregg and K. S. W. Sing. *Adsorption, Surface Area and Porosity*. Academic Press, 1967.

[50] J. C. Groen, L. A. A. Pefffer, and J. Perez-Ramirez. Pore size determination in modified micro- and mesoporous materials. Pitfalls and limitations in gas adsorption data analysis. *Microporous and Mesoporous Materials*, 60:1–17, 2003.

[51] Z. Guo, Y. Li, and W. Wu. Sorption of U(VI) on goethite: Effects of pH, ionic strength, phosphate, carbonate and fulvic acid. *Applied Radiation and Isotopes*, 67(6):996–1000, 2009.

[52] A. Gurses, C. Dogar, M. Yalcin, M. Acikyildiz, R. Bayrak, and S. Karaca. The adsorption kinetics of the cationic dye, methylene blue, onto clay. *Journal of Hazardous Materials*, 131(1-3):217–228, 2006.

[53] J. P. Gustafsson, E. Dassman, and M. Backstrom. Towards a consistent geochemical model for prediction of uranium(VI) removal from groundwater by ferrihydrite. *Applied Geochemistry*, 24:454–462, 2009.

[54] P. T. Hang. Methylene blue adsorption by clay minerals - Determination of surface areas and cation exchange capacities. *Clays and Clay Minerals*, 18(4):203–212, 1970.

[55] T. M. Harris and E. T. Knobbe. Assessment of porosity in sol-gel silica thin films by dye adsorption. *Journal of Materials Science Letters*, 15(2):153–155, 1996.

[56] T. Hiemstra, W. H. Van Riemsdijk, A. Rossberg, and K. U. Ulrich. A surface structural model for ferrihydrite. II. Adsorption of uranyl and carbonate. *Geochimica Et Cosmochimica Acta*, 73(15):4437–4451, 2009.

[57] A. E. Hixon, Y. J. Hu, D. I. Kaplan, R. K. Kukkadapu, H. Nitsche, O. Qafoku, and B. A. Powell. Influence of iron redox transformations on plutonium sorption to sediments. *Radiochimica Acta*, 98(9-11):685–692, 2010.

[58] C. H. Ho and D. C. Doern. The sorption of uranyl species on a hematite sol. *Canadian Journal of Chemistry*, 63(5):1100–1104, 1985.

[59] C. H. Ho and N. H. Miller. Effect of humic-acid on uranium uptake by hematite particles. *Journal of Colloid and Interface Science*, 106(2):281–288, 1985.

[60] C. K. D. Hsi and D. Langmuir. Adsorption of uranyl onto ferric oxyhydroxides - application of the surface complexation site-binding model. *Geochimica Et Cosmochimica Acta*, 49(9):1931–1941, 1985.

[61] Y. J. Hu. *Reaction of Plutonium(VI) with the Manganese-Substituted Iron Oxide Mineral Goethite*. PhD thesis, University of California, Berkeley, 2011.

[62] Y. J. Hu, L. K. Schwaiger, C. H. Booth, R. K. Kukkadapu, E. Cristiano, D. Kaplan, and H. Nitsche. Molecular interactions of plutonium(VI) with synthetic manganese-substituted goethite. *Radiochimica Acta*, 98(9-11):655–663, 2010.

[63] Y. J. Hu, R. E. Wilson, C. H. Booth, L. K. Brogan, T. Parsons-Moss, and H. Nitsche. Synchrotron X-ray beam-induced chemistry of plutonium(VI) sorbed to various substrates. In Preparation.

[64] M. Iwamoto, T. Abe, and Y. Tachibana. Effect of competing anions on the adsorption of arsenite and arsenate by ferrihydrite. *Journal of Molecular Catalysis A: Chemical*, 155:143–153, 2000.

[65] J. L. Jambor and J. E. Dutrizac. Occurrence and constitution of natural and synthetic ferrihydrite, a widespread iron oxyhydroxide. *Chemical Reviews*, 98(7):2549–2585, 1998.

[66] L. Jelinek and E. S. Kovats. True surface areas from nitrogen adsorption experiments. *Langmuir*, 10:4225–4231, 1994.

[67] K. Jiratova. Isoelectric point of modified alumina. *Applied Catalysis*, 1(3-4):165–167, 1981.

[68] G. Kahr and F. T. Madsen. Determination of the cation exchange capacity and the surface area of bentonite, illite and kaolinite by methylene blue adsorption. *Applied Clay Science*, 9(5):327–336, 1995.

[69] S. N. Kalmykov, V. V. Kriventsov, Y. A. Teterin, and A. P. Novikov. Plutonium and neptunium speciation bound to hydrous ferric oxide colloids. *Comptes Rendus Chimie*, 10(10-11):1060–1066, 2007.

[70] W. M. Keely and H. W. Maynor. Thermal studies of nickel, cobalt, iron and copper oxides and nitrates. *Journal of Chemical & Engineering Data*, 8(3):297–300, 1963.

[71] A. A. Khaleel. Nanostructured pure gamma-Fe_2O_3 via forced precipitation in an organic solvent. *Chemistry - A European Journal*, 10(4):925–932, 2004.

[72] J. J. Kipling and R. B. Wilson. Adsorption of methylene blue in the determination of surface areas. *Journal of Applied Chemistry*, 10(3):109–113, 1960.

[73] F. Kleitz, S. H. Choi, and R. Ryoo. Cubic *Ia3d* large mesoporous silica: synthesis and replication to platinum nanowires, carbon nanorods and carbon nanotubes. *Chemical Communications*, pages 2136–2137, 2003.

[74] P. Klobes, K. Meyer, and R. G. Munro. *Porosity and Specific Surface Area Measurements for Solid Materials*. National Institute of Standards and Technology, 2006.

[75] M. Kosmulski. The pH-dependent surface charging and the points of zero charge. *Journal of Colloid and Interface Science*, 253:77–87, 2002.

[76] M. Kosmulski. pH-dependent surface charging and points of zero charge. II. Update. *Journal of Colloid and Interface Science*, 275:214–224, 2004.

[77] M. Kosmulski. pH-dependent surface charging and points of zero charge. III. Update. *Journal of Colloid and Interface Science*, 298:730–741, 2006.

[78] D. I. Kreller, G. Gibson, G. W. vanLoon, and J. H. Horton. Chemical force microscopy investigation of phosphate adsorption on the surfaces of iron(III) oxyhydroxide particles. *Journal of Colloid and Interface Science*, 254:205–213, 2002.

[79] J. L. Krumhansl, P. V. Brady, and P. C. Zhang. *Geochemistry of soil radionuclides*, chapter Soil mineral backfills and radionuclide retention. Soil Society of America, 2002.

[80] J. K. Leland and A. J. Bard. Photochemistry of colloidal semiconducting iron-oxide polymorphs. *Journal of Physical Chemistry*, 91(19):5076–5083, 1987.

[81] J. J. Lenhart and B. D. Honeyman. Uranium(VI) sorption to hematite in the presence of humic acid. *Geochimica Et Cosmochimica Acta*, 63(19-20):2891–2901, 1999.

[82] Z. Li, T. Zhang, and K. Li. One-step synthesis of mesoporous two-line ferrihydrite for effective elimination of arsenic contaminants from natural water. *Dalton Transactions*, 40(9):2062–2066, 2011.

[83] R. Lim-Nunez and R. J. Gilkes. Acid dissolution of synthetic metal-containing goethites and hematites. In *Proceedings of the International Clay Conference, Denver, 1985*, pages 197–204, 1987.

[84] B. C. Lippens and J. H. de Boer. Studies on pore systems in catalysts .V. t method. *Journal of Catalysis*, 4(3):319–323, 1965.

[85] B. C. Lippens, B. G. Linsen, and J. H. de Boer. Studies on pore systems in catalysts .1. The adsorption of nitrogen - apparatus and calculation. *Journal of Catalysis*, 3(1):32–37, 1964.

[86] G. Liu, S. Debnath, K. W. Paul, W. Han, D. B. Hausner, H. A. Hosein, F. M. Michel, J. B. Parise, D. L. Sparks, and D. R. Strongin. Characterization and surface reactivity of ferrihydrite nanoparticles assembled in ferritin. *Langmuir*, 22(22):9313–9321, Oct 24 2006.

[87] N. Lu, C. R. Cotter, H. D. Kitten, J. Bentley, and I. R. Triay. Reversibility of sorption of plutonium-239 onto hematite and goethite colloids. *Radiochimica Acta*, 83(4):167–173, 1998.

[88] W. W. Lukens, P. Schmidt-Winkel, D. Zhao, J. Feng, and G. D. Stucky. Evaluating pore sizes in mesoporous materials: A simplified standard adsorption method and a simplified Broekhoff-de Boer method. *Langmuir*, 15:5403–5409, 1999.

[89] Y. L. Ma, Z. R. Xu, T. Guo, and P. You. Adsorption of methylene blue on Cu(II)-exchanged montmorillonite. *Journal of Colloid and Interface Science*, 280(2):283–288, 2004.

[90] T. Mathew, K. Suzuki, Y. Ikuta, Y. Nagai, N. Takahashi, and H. Shinjoh. Mesoporous ferrihydrite-based iron oxide nanoparticles as highly promising materials for ozone removal. *Angew. Chem., Int. Ed.*, 50(32):7381–7384, 2011.

[91] T. Mathew, K. Suzuki, Y. Nagai, T. Nonaka, Y. Ikuta, N. Takahashi, N.o Suzuki, and H. Shinjoh. Mesoporous 2-line ferrihydrite by a solution-phase cooperative assembly process for removal of organic contaminants in air. *Chemistry - A European Journal*, 17(4):1092–1095, 2011.

[92] P. A. Maurice. *Environmental Surfaces and Interfaces from the Nanoscale to the Global Scale*. John Wiley & Sons, 2009.

[93] T. D. McKinley. *The Electron Microprobe*. John Wiley & Sons, 1966.

[94] F. M. Michel, V. Barron, J. Torrent, M. P. Morales, C. J. Serna, J. F. Boily, Q. Liu, A. Ambrosini, A. C. Cimasu, and G. E. Jr. Brown. Ordered ferrimagnetic form of ferrihydrite reveals links among structure, composition, and magnetism. *Proceedings of the National Acadamy of Sciences*, 107:2787–2792, 2010.

[95] F. M. Michel, L. Ehm, S. M. Antao, P. L. Lee, P. J. Chupas, G. Liu, D. R. Strongin, M. A. A. Schoonen, B. L. Phillips, and J. B. Parise. The structure of ferrihydrite, a nanocrystalline material. *Science*, 316(5832):1726–1729, 2007.

[96] T. Missana, M. Garcia-Gutierrez, and C. Maffiotte. Experimental and modeling study of the uranium(VI) sorption on goethite. *Journal of Colloid and Interface Science*, 260(2):291–301, 2003.

[97] J. R. Moody and R. M. Lindstrom. Selection and cleaning of plastic containers for storage of trace-element samples. *Analytical Chemistry*, 49(14):2264–2267, 1977.

[98] S. J. Morrison, R. R. Spangler, and V. S. Tripathi. Adsorption of uranium(VI) on amorphous ferric oxyhydroxide at high concentrations of dissolved carbon(IV) and sulfur(VI). *Journal of Contaminant Hydrology*, 17:333–346, 1995.

[99] L. N. Moyes, R. H. Parkman, J. M. Charnock, D. J. Vaughan, F. R. Livens, C. R. Hughes, and A. Braithwaite. Uranium uptake from aqueous solution by interaction with goethite, lepidocrocite, muscovite, and mackinawite: An X-ray absorption spectroscopy study. *Environmental Science & Technology*, 34(6):1062–1068, 2000.

[100] M. Mullet, P. Fievet, J. C. Reggiani, and J. Pagetti. Surface electrochemical properties of mixed oxide ceramic membranes: Zeta-potential and surface charge density. *Journal of Membrane Science*, 123(2):255–265, 1997.

[101] S. Mustafa, B. Dilara, K. Nargis, A. Naeem, and P. Shahida. Surface properties of the mixed oxides of iron and silica. *Colloids and Surfaces A - Physicochemical and Engineering Aspects*, 205(3):273–282, 2002.

[102] National Diagnostics. Fundamentals of liquid scintillation counting. *https://www.nationaldiagnostics.com/liquid-scintillation/articles*.

[103] V. Neck, M. Altmaier, A. Seibert, J. I. Yun, C. M. Marquardt, and Th Fanghaenel. Solubility and redox reactions of Pu(IV) hydrous oxide: Evidence for the formation of $PuO(^{+}_{2}x)$(shyd). *Radiochimica Acta*, 95(4):193–207, 2007.

[104] T. W. Newton. The kinetics of the oxidation-reduction reactions of uranium, neptunium, plutonium, and americium in aqueous solutions. Technical report, U. S. Energy Research and Development Administration Technical Information Center, Oak Ridge, TN, 1975.

[105] T. W. Newton, D. E. Hobart, and P. D. Palmer. The formation of Pu(VI)-colloid by the alpha-reduction of Pu(V) or Pu(VI) in aqueous solutions. *Radiochimica Acta*, 39:139–47, 1986.

[106] H. Nitsche. Solubility studies of transuranium elements for nuclear waste disposal: Principles and overview. *Radiochimica Acta*, 52/53:3–8, 1991.

[107] J. S. Noh and J. A. Schwarz. Estimation of the point of zero charge of simple oxides by mass titration. *Journal of Colloid and Interface Science*, 130(1):157–164, 1989.

[108] A. C. Oliveira, G. S. Marchetti, and M. D. Rangel. The effect of the starting material on the thermal decomposition of iron oxyhydroxides. *Journal of Thermal Analysis and Calorimetry*, 73(1):233–240, 2003.

[109] G. Pacchioni. Oxygen vacancy: The invisible agent on oxide surfaces. *ChemPhysChem*, 4:1041–1047, 2003.

[110] P. J. Panak, C. H. Booth, D. L. Caulder, J. J. Bucher, D. K. Shuh, and H. Nitsche. X-ray absorption fine structure spectroscopy of plutonium complexes with *Bacillus sphaericus*. *Radiochimica Acta*, 90:315–321, 2002.

[111] G. A. Parks and P. L. de Bruyn. Zero point of charge of oxides. *Journal of Physical Chemistry*, 66(6):967–973, 1962.

[112] T. E. Payne, J. A. Davis, and T. D. Waite. Uranium adsorption on ferrihydrite - effects of phosphate and humic acid. *Radiochimica Acta*, 74:239–243, 1996.

[113] S. I. Pechenyuk and S. I. Matveenko. Changes in the acid-base properties of hydrogels of metal oxide hydroxides induced by aging in solutions of electrolytes. *Russian Chemical Bulletin, International Edition*, 49:1323–1326, 2000.

[114] M. L. Pierce and C. B. Moore. Adsorption of arsenite on amorphous iron hydroxide from dilute aqueous solution. *Environmental Science & Technology*, 14:214–216, 1980.

[115] B. A. Powell, R. A. Fjeld, D. I. Kaplan, J. T. Coates, and S. M. Serkiz. $Pu(V)O_2^+$ adsorption and reduction by synthetic hematite and goethite. *Environmental Science & Technology*, 39(7):2107–2114, 2005.

[116] X. Qian, X. Zhang, Y. Bai, T. Li, X. Tang, E. Want, and S. Dong. Photoelectrochemical characteristics of α-Fe_2O_3 nanocrystalline semiconductor thin film. *Journal of Nanoparticle Research*, 2:191–198, 2000.

[117] S. W. Rabideau, M. J. Bradley, and H. D. Cowan. Alpha-particle oxidation and reduction in aqueous plutonium solutions. Technical report, Los Alamos Scientific Laboratory, 1958.

[118] Y. Ralchenko, A. E. Kramida, and J. Reader. NIST atomic spectra database (ver. 4.1.0), 2011.

[119] J. Ralph and I. Chau. Goethite. *http://www.mindat.org/min-1719.html*, 1993-2012.

[120] T. Reich, H. Moll, T. Arnold, M. A. Denecke, C. Hennig, G. Geipel, G. Bernhard, H. Nitsche, P. G. Allen, J. J. Bucher, N. M. Edelstein, and D. K. Shuh. An EXAFS study of uranium(VI) sorption onto silica gel and ferrihydrite. *Journal of Electron Spectroscopy and Related Phenomena*, 96(1-3):237–243, 1998.

[121] A. Y. Romanchuk, S. N. Kalmykov, and R. A. Aliev. Plutonium sorption onto hematite colloids at femto- and nanomolar concentrations. *Radiochimica Acta*, 99(3):137–144, 2011.

[122] A. Rossberg, K. U. Ulrich, S. Weiss, S. Tsushima, T. Hiemstra, and A. C. Scheinost. Identification of uranyl surface complexes on ferrihydrite: Advanced EXAFS data analysis and CD-MUSIC modeling. *Environmental Science & Technology*, 43(5):1400–1406, 2009.

[123] W. Runde. Chemical interactions of actinides in the environment. *Los Alamos Science*, 26:392–411, 2000.

[124] J. C. Ryden, J. R. McLaughlin, and J. K. Syers. Mechanisms of phosphate sorption by soils and hydrous ferric-oxide gel. *The Journal of Soil Science*, 28:72–92, 1977.

[125] A. L. Sanchez, J. W. Murray, and T. H. Sibley. The adsorption of plutonium-IV and plutonium-V on goethite. *Geochimica Et Cosmochimica Acta*, 49(11):2297–2307, 1985.

[126] U. Schwertmann and R. M. Cornell. *Iron Oxides in the Laboratory*. VCH Publishers, Inc., New York, 1991.

[127] U. Schwertmann and E. Murad. Effect of pH on the formation of goethite and hematite from ferrihydrite. *Clays and Clay Minerals*, 31(4):277–284, 1983.

[128] W. M. Shaheen. Thermal behaviour of pure and binary $Fe(NO_3)_3 \cdot 9\,H_2O$ and $(NH_4)_6Mo_7O_{24} \cdot 4\,H_2O$ systems. *Materials Science and Engineering A - Structural Materials Properties Microstructure and Processing*, 445:113–121, 2007.

[129] D. A. Shaughnessy, H. Nitsche, C. H. Booth, D. K. Shuh, G. A. Waychunas, R. E. Wilson, H. Gill, K. J. Cantrell, and R. J. Serne. Molecular interfacial reactions between Pu(VI) and manganese oxide minerals manganite and hausmannite. *Environmental Science & Technology*, 37:3367–3374, 2003.

[130] D. M. Sherman. Electronic structures of iron(III) and manganese(IV) (hydr)oxide minerals: Thermodynamics of photochemical reductive dissolution in aquatic environments. *Geochimica Et Cosmochimica Acta*, 69(13):3249–3255, 2005.

[131] D. M. Sherman, C. L. Peacock, and C. G. Hubbard. Surface complexation of U(VI) on goethite (alpha-FeOOH). *Geochimica Et Cosmochimica Acta*, 72(2):298–310, 2008.

[132] X. Shuibo, Z. Chun, Z. Xinghuo, Y. Jing, Z. Xiaojian, and W. Jingsong. Removal of uranium(VI) from aqueous solution by adsorption of hematite. *Journal of Environmental Radioactivity*, 100(2):162–166, 2009.

[133] E. E. Sileo, M. Alvarez, and E. H. Rueda. Structural studies on the manganese for iron substitution in the synthetic goethite-jacobsite system. *International Journal of Inorganic Materials*, 3(4-5):271–279, 2001.

[134] K. S. W. Sing. Physisorption of nitrogen by porous materials. *Journal of Porous Materials*, 2:5–8, 1995.

[135] K. S. W. Sing, D. H. Everett, R. A. W. Haul, L. Moscou, R. A. Pierotti, J. Rouquerol, and T. Siemieniewska. Reporting physisorption data for gas/solid systems with special reference to the determination of surface area and porosity. *Pure and Applied Chemistry*, 57(4):603–619, 1985.

[136] A. Singh, K. U. Ulrich, and D. E. Giammar. Impact of phosphate on U(VI) immobilization in the presence of goethite. *Geochimica Et Cosmochimica Acta*, 74(22):6324–6343, 2010.

[137] D. S. Smith and F. G. Ferris. Proton binding by hydrous ferric oxide and aluminum oxide surfaces interpreted using fully optimized continuous pKa spectra. *Environmental Science & Technology*, 35:4637–4642, 2001.

[138] D. S. Smith and F. G. Ferris. Specific surface chemical interactions between hydrous ferric oxide and iron-reducing bacteria determined using pKa spectra. *Journal of Colloid and Interface Science*, 266:60–67, 2003.

[139] S. J. Smith, K. Page, H. Kim, B. J. Campbell, J. Boerio-Goates, and B. F. Woodfield. Novel synthesis and structural analysis of ferrihydrite. *Inorganic Chemistry*, 51:6421–6424, 2012.

[140] R. G. Sowden. Radiolytic problems in water reactors. *Journal of Nuclear Materials*, 8:81–101, 1963.

[141] L. Spadini, P. W. Schindler, L. Charlet, A. Manceau, and K. V. Ragnarsdottir. Hydrous ferric oxide: evaluation of CdHFO surface complexation models combining CdK EXAFS data, potentiometric titration results, and surface site structures identified from mineralogical knowledge. *Journal of Colloid and Interface Science*, 266:1–18, 2003.

[142] G. Sposito. The operational definition of the zero point of charge in soils. *Soil Science Society of America Journal*, 45:292–297, 1981.

[143] G. Sposito. *The Chemistry of Soils.* Oxford University Press, 2nd edition, 2008.

[144] M. Stefanescu, O. Stefanescu, M. Stoia, and C. Lazau. Thermal decomposition of some metal-organic precursors. *Journal of Thermal Analysis and Calorimetry*, 88(1):27–32, 2007.

[145] B. D. Stewart, R. T. Amos, P. S. Nico, and S. Fendorf. Influence of uranyl speciation and iron oxides on uranium biogeochemical redox reactions. *Geomicrobiology Journal*, 28(5-6):444–456, 2011.

[146] W. Stumm. *Chemistry of the Solid-Water Inferface.* J. Wiley & Sons, Inc., 1992.

[147] W. Stumm. Aquatic colliods as chemical reactants - Surface-structure and reactivity. *Colloids and Surfaces A - Physicochemical and Engineering Aspects*, 73:1–18, 1993.

[148] S. Stumpf, T. Stumpf, K. Dardenne, C. Hennig, H. Foerstendorf, R. Klenze, and T. Fanghnel. Sorption of Am(III) onto 6-line-ferrihydrite and its alteration products: Investigations by EXAFS. *Environmental Science & Technology*, 40:3522–3528, 2006.

[149] D. A. Sverjensky and K. Fukushi. A predictive model (ETLM) for As(III) adsorption and surface speciation on oxides consistent with spectroscopic data. *Geochimica Et Cosmochimica Acta*, 70:3778–3802, 2006.

[150] S. D. Tanner, V. I. Baranov, and D. R. Bandura. Reaction cells and collision cells for ICP-MS: a tutorial review. *Spectrochimica Acta Part B - Atomic Spectroscopy*, 57:1361–1452, 2002.

[151] R. Thomas. A beginner's guide to ICP-MS - part III: The plasma source. *Spectroscopy*, 16(6):26–30, 2001.

[152] R. Thomas. A beginner's guide to ICP-MS - part IV: The interface region. *Spectroscopy*, 16:26–34, 2001.

[153] R. Thomas. A beginner's guide to ICP-MS - part V: The ion focusing system. *Spectroscopy*, 16(9):38–44, 2001.

[154] R. Thomas. Beginner's guide to ICP-MS - part VI - the mass analyzer. *Spectroscopy*, 16(10):44–48, 2001.

[155] R. Thomas. Spectroscopy tutorial - a beginner's guide to ICP-MS - part II: The sample-introduction system. *Spectroscopy*, 16(5):56–60, 2001.

[156] R. Thomas. A beginner's guide to ICP-MS - part IX - mass analyzers: Collision/reaction cell technology. *Spectroscopy*, 17(2):42–48, 2002.

[157] R. Thomas. A beginner's guide to ICP-MS part XII - a review of interferences. *Spectroscopy*, 17(10):24–31, 2002.

[158] E. Tipping. The adsorption of aquatic humic substances by iron oxides. *Geochimica Et Cosmochimica Acta*, 45:191–199, 1981.

[159] G. Tong, J. Guan, Z. Xiao, X. Huang, and Y. Guan. In situ generated gas bubble-assisted modulation of the morphologies, photocatalytic, and magnetic properties of ferric oxide nanostructures synthesized by thermal decomposition of iron nitrate. *Journal of Nanoparticle Research*, 12(8):3025–3037, 2010.

[160] Semitracks Online Training. Energy dispersive X-ray spectrometry. *www.semitracks.com*, 2012.

[161] P. Trivedi and L. Axe. Ni and Zn sorption to amorphous versus crystalline iron oxides: Macroscopic studies. *Journal of Colloid and Interface Science*, 244:221–229, 2001.

[162] P. Trivedi, J. A. Dyer, and D. L. Sparks. Lead sorption onto ferrihydrite. 1. A macroscopic and spectroscopic assessment. *Environmental Science & Technology*, 37:908–914, 2003.

[163] J. K. Tuli. *Nuclear Wallet Cards*. Brookhaven National Laboratory, National Nuclear Data Center, 8th edition, 2011.

[164] H. Tüysüz, E. L. Salabas, C. Weidenthaler, and F. Schuth. Synthesis and magnetic investigation of ordered mesoporous two-line ferrihydrite. *Journal of the American Chemical Society*, 130(1):280–287, 2008.

[165] R. K. Vempati, R. V. Morris, H. V. Lauer, and P. A. Helmke. Reflectivity and other physicochemical properties of Mn-substituted goethites and hematites. *Journal of Geophysical Research - Planets*, 100(E2):3285–3295, 1995.

[166] T. D. Waite. Photo-redox processes at the mineral-water interface. *Reviews in Mineralogy*, 23:559–603, 1990.

[167] T. D. Waite, J. A. Davis, T. E. Payne, G. A. Waychunas, and N. Xu. Uranium(VI) adsorption of ferrihydrite - application of a surface complexation model. *Geochimica Et Cosmochimica Acta*, 58(24):5465–5478, 1994.

[168] N. A. Wall, S. B. Clark, and J. L. McHale. Synthesis and characterization of 1:1 layered uranyl silicate mineral phases. *Chemical Geology*, 274:149–157, 2010.

[169] G. A. Waychunas, C. S. Kim, and J. F. Banfield. Nanoparticulate iron oxide minerals in soils and sediments: unique properties and contaminant scavenging mechanisms. *Journal of Nanoparticle Research*, 7(4-5):409–433, 2005.

[170] G. A. Waychunas, B. A. Rea, C. C. Fuller, and J. A. Davis. Surface-chemistry of ferrihydrite. I. EXAFS studies of the geometry of coprecipitated and adsorbed arsenate. *Geochimica Et Cosmochimica Acta*, 57(10):2251–2269, 1993.

[171] M. Wazne, G. P. Korfiatis, and X. G. Meng. Carbonate effects on hexavalent uranium adsorption by iron oxyhydroxide. *Environmental Science & Technology*, 37(16):3619–3624, 2003.

[172] P. G. Weidler. BET sample pretreatment of synthetic ferrihydrite and its influence on the determination of surface area and porosity. *Journal of Porous Materials*, 4(3):165–169, 1997.

[173] D. A. Wheeler, G. Wang, Y. Ling, Y. Li, and J. Z. Zhang. Nanostructured hematite: synthesis, characterization, charge carrier dynamics, and photoelectrochemical properties. *Energy and Environmental Science*, 5:6682–6702, 2012.

[174] K. Wieczorek-Ciurowa and A. J. Kozak. The thermal decomposition of $Fe(NO_3)_3 \cdot 9\,H_2O$. *Journal of Thermal Analysis and Calorimetry*, 58(3):647–651, 1999.

[175] I. R. Willett, C. J. Chartres, and T. T. Nguyen. Migration of phosphate into aggregated particles of ferrihydrite. *Journal of Soil Science*, 39(2):275–282, Jun 1988.

[176] R. E. Wilson. *Reactions of Plutonium(VI) with the Iron Oxide Goethite*. PhD thesis, University of California, Berkeley, 2005.

[177] W. Xia, W. Meng, K. Zhu, R. Yu, X. Xing, and D. Wang. Preparation of a porous iron oxyhydroxide from layered double hydroxides precursors. *Clay Science*, 12:285–288, 2006.

[178] Y. Yukselen and A. Kaya. Comparison of methods for determining specific surface area of soils. *Journal of Geotechnical and Geoenvironmental Engineering*, 132(7):931–936, 2006.

[179] Y. Yukselen and A. Kaya. Suitability of the methylene blue test for surface area, cation exchange capacity and swell potential determination of clayey soils. *Engineering Geology*, 102(1-2):38–45, 2008.

[180] J. M. Zachara, D. C. Girvin, R. L. Schmidt, and C. T. Resch. Chromate adsorption on amorphous iron oxyhydroxide in the presence of major groundwater ions. *Environmental Science & Technology*, 21(6):589–594, 1987.

[181] H. Zeng, A. Singh, S. Basak, K. U. Ulrich, M. Sahu, P. Biswas, J. G. Catalano, and D. E. Giammar. Nanoscale size effects on uranium(VI) adsorption to hematite. *Environmental Science & Technology*, 43(5):1373–1378, March 2009.

[182] J. Zhao, F. E. Huggins, Z. Feng, F. L. Lu, N. Shah, and G. P. Huffman. Structure of a nanophase iron-oxide catalyst. *Journal of Catalysis*, 143(2):499–509, 1993.

[183] J. M. Zhao, F. E. Huggins, Z. Feng, and G. P. Huffman. Ferrihydrite - surface-structure and its effects on phase-transformation. *Clays and Clay Minerals*, 42(6):737–746, 1994.

Appendix A

Inductively Coupled Plasma Mass Spectrometry

A.1 Introduction

Trace analysis of non-plutonium aqueous elements was performed using inductively coupled plasma mass spectrometry (ICP-MS), an analytical instrument designed to perform trace metal analysis. In order to better describe the reasoning behind standard and sample preparation, data analysis, and experimental difficulties, a brief discussion of the instrument is required. The preparation of both standards and samples will be discussed, as will the difficulties and limitations involved in preparation and analysis.

A.2 Advantages of the System

ICP-MS is a valuable instrument due to the very large analytical working range, covering approximately nine orders of magnitude and extending down below the part per trillion (ppt) range for many elements. The sample introduction is often very straightforward and a wide range of sample compositions can be accommodated. Although there can be interferences with the analytes of interest, tools like the dynamic reaction chamber (DRC) can be used to reduce or eliminate those interferences. Sample analysis is rapid (less than 5 minutes for most samples) and results are relatively easy to analyze.

A.3 Instrument Description

The instrument used during the course of these experiments was a Perkin Elmer Elan DRC II (see Figure A.1). Aqueous samples acidified to approximately 2 % nitric acid are injected into a nebulizer using a peristaltic pump. The nebulizer creates an aerosol that is then sent to a spray chamber to remove droplets that are too large before entering the plasma torch. The plasma torch consists of concentric quartz tubes wrapped at the end by a radio frequency (RF) coil. Argon flows in, and using seed electrons from an electron gun couples with the energy from the RF generator to create a plasma. Temperatures in the

plasma are generally around 6000 K, and the purpose is to dry the aerosol, dissociate any molecules, and remove an electron from each atom to form singly-charged ions. [155, 151]

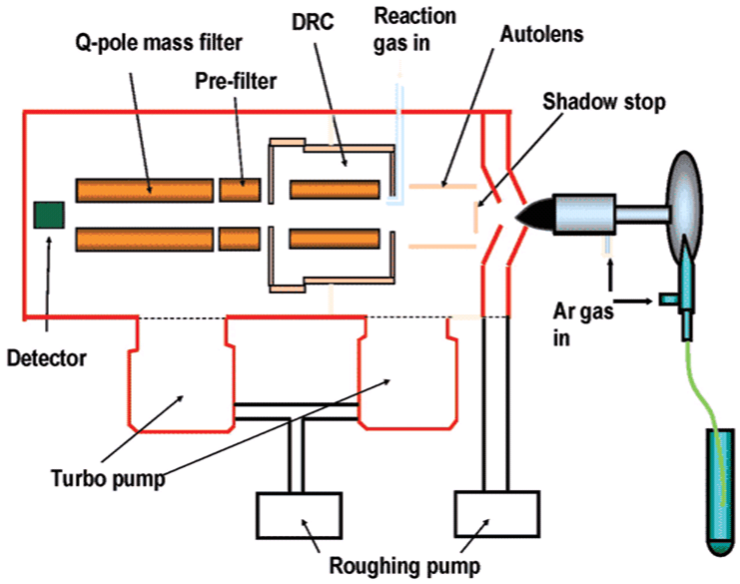


Figure A.1: Diagram of a Perkin Elmer Elan DRC II instrument. From Armstrong (2008) [5].

The ionized samples are then sent through ion optics to direct the sample stream into a quadrupole mass spectrometer, remove neutral species and photons, and to bring the sample from the atmospheric pressure plasma to the vacuum system of the quadrupole. This system consists of sample and skimmer cones, a vacuum system, and an ion deflection device. The cones reduce the pressure of the sample while reducing the beam divergence. The vacuum is maintained using a roughing pump followed by a turbomolecular pump. The ion deflection device is generally a quadrupole at a right-angle to the ion path, but for the particular ICP-MS used in these studies, it is a circular lens with a shadow stop. This removes photos and will select the appropriate masses to introduce into the quadrupole by varying the lens voltage. [152, 153]

Interferences arise when ions from the sample and/or plasma have the same mass-to-charge ratio as the analyte, raising the background and making it more variable [157]. Common interferences for the analysis in this work include $^{40}Ar^{16}O$ for ^{56}Fe, $^{40}Ar^{16}O^{1}H$ for ^{57}Fe, and $^{38}Ar^{16}O^{1}H$ for ^{55}Mn. Because these cover all of the elements of interest for most experiments, all samples were directed through the dynamic reaction cell (DRC) to remove interferences when possible.

The DRC is a system specific to the Perkin Elmer Elan series ICP-MS instruments, and consists of a quadrupole inside a reaction chamber. The reaction chamber is filled with a reaction gas, specifically selected for the matrix and interferences in question. For the experiments herein, the reaction gas was ammonia, which is very common. The reaction gas

interacts with the interfering ions to change the mass in several ways: collisional dissociation, electron transfer, proton transfer, or oxidation. All of these methods change the interference to a non-interfering product at a different mass. A dynamic bandpass tuning (DBT) mechanism also removes all other ions prior to entering the DRC to prevent these products from forming secondary interferences. The DBT uses the DRC quadrupole to define a mass bandpass window to only allow a specific mass into the DRC, significantly increasing the effectiveness of the reaction cell. [150, 156]

Each analyte is measured usually by the most abundant isotope, but if there are several isotopes with significant abundances, then multiple isotopes can be measured for comparison. A significant difference between concentrations measured for isotopes of the same element generally indicates a problem in the cell gas flow optimization through the DRC for that element.

Once they have passed through the DRC, analyte ions enter the quadrupole mass spectrometer. The quadrupole mass spectrometer changes the voltages and radio frequencies between its four rods to only allow ions with the correct mass-to-charge ratio to pass through. During measurement, it scans across all of mass-to-charge ratios of interest. Each analyte is assayed multiple times per sample to gain good statistics. [154] The ions passing through the mass spectrometer reach the dynode of an electron multiplier detection system. Each ion to hit the dynode releases an electron that multiplies on subsequent dynodes to create a cascade until a measurable pulse is reached. [154] The measured pulses are calibrated to a standard series to determine the sample concentrations. The detector in the Elan DRC II can operate in both digital and analog mode, depending on the analyte concentration. The analog mode is more sensitive, but as is not able to measure above approximately 500 parts per billion (ppb), efforts are generally made to keep samples under that concentration.

A.4 Data Handling

The software that accompanies the instrument performs data analysis using the calibration standards. This analysis average the replicates, subtracts the blank, and rounds to the nearest whole count. This rounded average is used for calculations, and although it is close, there is still some rounding error that ideally would not be taken until later. The larger difficulty arises when considering the internal standard correction. The software simply multiplies the intensities in the data by the ratio of the measured intensity of the internal standard element in the first standard to the measured intensity in the samples. The concentration in the first standard is assumed to be the exact concentration of the internal standard in the remaining standards and all of the samples. Unfortunately, there is no way to account for any internal standard concentration differences between the samples, thus leading to potentially large inaccuracies in the final data if there is significant variation in the internal standard concentration of both the standards and the samples. While in theory it is possible to obtain the same concentration in all of the samples, due to human error in addition, it is unlikely that this will be the case. Additionally, the software data analysis provides no error or uncertainty values other than the relative standard deviation between the replicates.

To account for these inaccuracies, data analysis is performed on the raw data outside of

the software package. The rounding is removed from the replicate averaging, and a correction is made for the differences in the internal standard concentrations. To maintain consistency with the software analysis, all the internal standard concentrations of the standard series are corrected to the first standard. A correction factor that relates the counts of the standard in question to the counts of the first standard is applied to the net counts, adjusting it based on the measured and calculated internal standard concentration. If this correction is not made, then the calculations match the software to within 10 %. However, with this correction made, the differences can be quite significant, and it seems an appropriate correction given that when these large differences are observed, the internal standard counts measured for the samples are considerably lower than those observed for the standards. This is not an error in the run because checking the concentration of the standards mid-run returns correct concentrations. It seems that there might be a matrix effect in the samples that causes Ga (the internal standard) to measure with a low intensity, perhaps the perchlorate. However, because the samples are uniformly low by approximately the same amount, it appears that this is systematic error that can be accounted for. Because the software package does not adequately account for these differences, a separate analysis is required.

The separate analysis also contains a more rigorous error calculation that uses the error in the counts (square root of the counts), the relative error of the replicates, and the preparation error for each of the standards and samples (based primarily on the uncertainty in balance measurements), and propagates this error through all of the calculations.

A.5 Preparation of Standards for ICP-MS

All ICP-MS standards are prepared by weight in order to prevent any temperature effects on concentration. They are prepared to match the matrix of the measured samples to prevent any differences in nebulizing efficiency, elemental interactions, etc. The concentrations range from near the minimum detection expected to the maximum (ideally 500 ppb, see A.6). Additionally, detection minimums on the instrument vary based on the element, but are generally about 5-10 ppt because the instrument is not located in a clean room. These concentration ranges for the samples give standard series generally ranging from 100 ppt to 500 ppb, with a higher point only if sample concentrations are significantly higher than 500 ppb. These standards must be remade periodically, particularly the dilute ones, and are run with every ICP-MS run. The standards and samples also contain an internal standard. This internal standard is the same concentration in all of the standards and samples, generally around 20 ppb, and allows for adjustments for instrumental drift. The element for this standard is an element that is nearby in the periodic table so that ionization energies are similar. It should, however, be at least one element away so that there is no overlap in the element peaks to prevent concentration changes in the sample from causing fluctuations in the measured internal standard concentration.

A.6 Preparation of Samples for ICP-MS

Samples are also prepared by weight if possible to prevent temperature effects on concentration. Additionally, the error from pipettors, even well-calibrated ones, is often greater

than the error produced from using a balance, increasing the overall accuracy of the measurement. As mentioned above, the ideal maximum for samples should be less than 500 ppb in order to stay within the best range of the dual-detector system. If higher concentrations are necessary due to solution composition, they should be under 10 ppm to prevent clogging the sample cones.

The general procedure is to calculate the desired final mass for the prepared sample to achieve the correct concentrations, then calculate the mass of internal standard necessary for that final mass. The sample is weighed into an acid-washed 15 mL Falcon tube, the appropriate amount of HNO_3 to reach about 2 % added, and the calculated amount of internal standard weighed in. The final mass necessary is then recalculated and the sample diluted to this value using the 2 % HNO_3 blank solution. Extra care should be taken to add the correct amounts for both the internal standard and the final addition of blank. If the solution amount is the same as the ideal final amount, an exactly equal or greater amount of internal standard must be added. Otherwise the total solution volume is guaranteed to be too much for the internal standard amount added.

A.7 General Notes

Ultra high purity chemicals should be used when possible; the impurities in reagents can significantly affect the measurements otherwise. All sample containers should also be tested with various cleaning procedures to determine the cleaning procedure that produces the lowest background levels (see Appendix C). For the experiments performed in this work, background levels for the vials were determined to be of acceptable levels to not subtract them. Backgrounds for vials washed using reagent grade acid were less than 10 ppt for manganese and less than 250 ppt for iron. Because these values were well within the error limits of almost all experiments, no corrections for the vials were made.

A.8 Fe Bleeding into the Mn Peak

When measuring samples with a high concentration of iron and a low concentration of manganese it is theoretically possible for the large Fe peak to overlap into the Mn window for measurement, causing artificially higher concentrations of Mn to be measured. To determine if this can happen for the concentrations of Fe typically measured in the measurements described in this work, Fe samples of various concentrations ranging from 0.5 to 1000 ppb were measured and analyzed for Mn content. Results showed that while the higher concentrations of Fe did give counts in the Mn window, they were not greater than the average background levels given by the vials themselves (see Appendix C for background levels), with the highest measurement being 30 ppt. Thus, it was determined that no subtraction from Mn peaks apart from standard background corrections needed to be performed.

Appendix B

Solubility of Cryptomelane and Pyrolusite

Two manganese minerals, pyrolusite (β-MnO_2) and cryptomelane ($K(Mn^{4+}Mn^{2+})_8O_{16}$), were added to 0.1 M $NaClO_4$ to create solutions of 4 g/L in glass media jars. The mineral solutions were pH balanced to pH values between 3 and 9.5 and left on an orbital shaker at room temperature (22-25 °C). The samples were opened to air and no effort was made to exclude carbonate in order to more closely mimic a natural system. The cryptomelane samples were also held in the dark. After 2.5 weeks (pyrolusite) or 14 months (cryptomelane), aliquots were withdrawn, filtered with Amicon 4mL regenerated cellulose filters, and measured using ICP-MS for manganese content. The results of these measurements are shown in Figures B.1 and B.2.

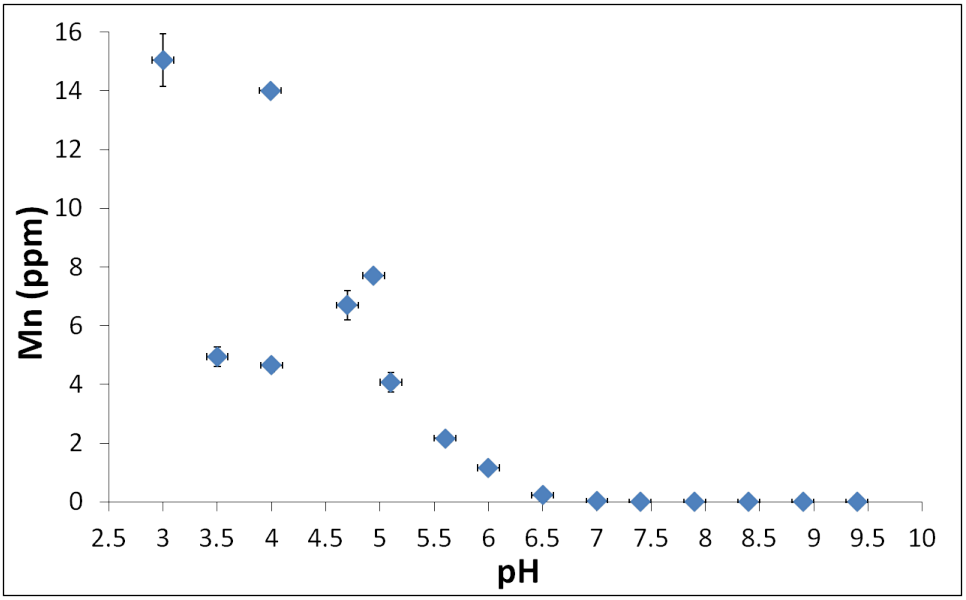


Figure B.1: Pyrolusite solubility in parts per million as a function of pH in 0.1 M $NaClO_4$.

Cryptomelane is clearly more soluble than pyrolusite at low pH, but the solubility falls to the limit of detection of the experiment by approximately pH 5.5 compared to pH 7 for

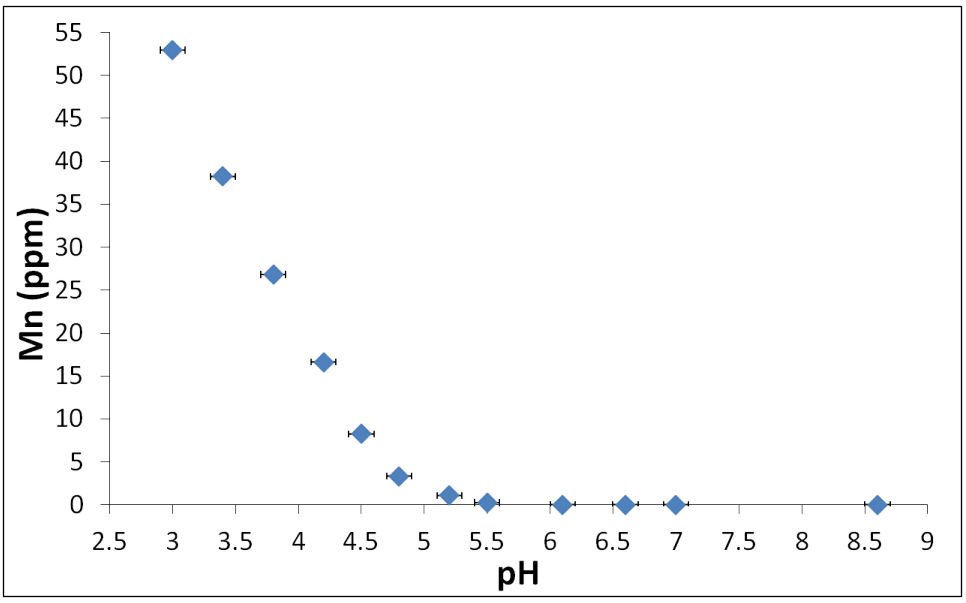


Figure B.2: Cryptomelane solubility in parts per million as a function of pH in 0.1 M $NaClO_4$.

pyrolusite. The cryptomelane points also form a much cleaner curve. Two of the pyrolusite samples, originally pH 3.5 and pH 4, did not fall on the curve for pyrolusite, and were significantly lower in concentration than expected. Repeats of these samples were made and then measured 31 months later, and were somewhat higher in concentration than expected. This change suggests either that the pyrolusite samples were not at equilibrium when they were originally measured or the pH was not accurately measured the second time. The most likely is that the original solutions were not yet at equilibrium due to the short equilibration time of only 2.5 weeks. However, the remeasured samples were not significantly higher than if they were fit nicely into the curve, meaning that the original curve is at least not significantly off from the equilibrium curve.

Appendix C

Acid Cleaning of Glassware

As shown by Table C.1, plastic tends to have fewer contaminants than glass. However, even plastic has metal and non-metal contaminants, and the level of various contaminants depends on the type of plastic, the manufacturer, and the manufacturing location. Therefore, it is a good idea to acid leach all plastics to remove these contaminants and prevent them from entering into solutions and disrupting the integrity of the results. It is also a good idea to acid wash laboratory glassware, although this will likely not leach as well as most plastics.

The general procedures determined for both heavy cleaning and routine cleaning are outlined below for both plastic and glass. Clean glass and, to a some extent, plastic, is hydrophilic and will have a uniformly wetted surface when distilled water is used as a final rinse. Contaminants such as detergent residues or grease will cause the water to bead and indicate that the cleaning procedure should be repeated. This provides an easy method to tell by eye if your cleaning procedure is effective.

While HCl may be better overall for leaching out of various plastics, both HCl and HNO_3 leach different elements with varying efficiency. Therefore, it is suggested to use both acids (one after the other) to achieve the greatest leaching for heavily contaminated plastic or experiments requiring the greatest amount of elemental accuracy. The general procedure accepted in our laboratory for heavy cleaning, adapted from Moody (1977) [97] is described below.

1. Wash/soak thoroughly with Alconox soap and water to remove most chemicals and their residues, ensuring that no solids are lodged on the surface (this maintains the cleanliness of the acids used following this step). Rinse well with water. NOTE: This step is not necessary for new containers.

2. Soak for one day in 1:1 HCl:Milli-Q water (fill the container carefully to the brim and cap it for each of the following steps).

3. Rinse with Milli-Q water.

4. Soak for one day in 1:1 HNO_3:Milli-Q water.

5. Rinse with Milli-Q water.

6. Soak for one day in Milli-Q water.

Material	No. of Elements	Total Conc. (ppm)	Major Constituents
PS	8 (8 N.D.*)	4	Na, Ti, Al
PSF	16 (12 N.D.*)	17	Na, Fe, Ca
TFE	24	19	Ca, Pb/Fe, Cu
LDPE	18	23	Ca, Cl, K
PC	10	85	Cl, Br, Al
PMP	14	178	Ca, Mg, Zn
FEP	25	241	K, Ca, Mg
PVC-tubing	9	280	Fe, Zn, Sb
PP	21	519	Cl, Mg, Ca
HDPE	22	654	Ca, Zn, Si
ETFE	32	1.007	Cl, Pb, Si
PVC-rigid	7 (11 N.D.)	2.541	Sn, Ca, Mg
Borosilicate Glass	14	497,249	Si, B, Na

* N.D. Not Detected NOTE: Values listed in the chart above represent typical contents for major constituents. Various NNI grades of plastics may vary from these values.

Table C.1: Summary of average element content of 12 plastics and borosilicate glass. From Moody and Lindstrom 1977. [97]

7. Store in Milli-Q water or allow to dry.

8. Neutralize and dispose of acids after approximately ten uses.

Care should be taken when soaking with Alconox soap, as extended soaking (on the order of weeks to months) in high concentration Alconox can remove the exterior markings from beakers, vials, and bottles. While in some cases this is desired, removal of volume markings, etc. is definitely not. The soaking times for HCl and Milli-Q water can be extended if necessary or desired, but care must be taken not to over soak plastics in nitric acid, as this leads to yellowing and degradation of the plastic. If this occurs, then the procedure can actually make the plastic dirtier. For containers that are likely to begin cleaner or are to be used in experiments requiring less elemental purity, a simpler procedure can be used, described below. This procedure is also desirable for use with more brittle plastics, as nitric acid is a strong oxidizer and can embrittle some plastics.

1. Wash thoroughly with Alconox soap and water. Rinse well with water. Note: This step is not necessary for new containers.

2. Soak for one day in 10 % HCl made with Milli-Q water.

3. Rinse with Milli-Q water.

4. Soak for one day in Milli-Q water.

5. Store in Milli-Q water or allow to dry.

Vial	Fe (ppt)	Mn (ppt)	Al (ppt)
Ultra High Purity, New Vial	261 ± 5	14.0 ± 0.7	146 ± 4
Ultra High Purity, Old Vial 1	680 ± 10	10.7 ± 0.6	133 ± 5
Ultra High Purity, Old Vial 2	2820 ± 30	6.0 ± 0.4	14 ± 2
Reagent Grade, New Vial	209 ± 4	3.7 ± 0.3	25 ± 2
Reagent Grade, Old Vial 1	19 ± 2	3.0 ± 0.3	-21 ± 3
Reagent Grade, Old Vial 2	8 ± 1	3.0 ± 0.3	-16 ± 2
Non Acid Washed, New Vial	92 ± 3	5.3 ± 0.3	124 ± 3
10 Use HCl, New Vial	-9 ± 2	1.0 ± 0.1	-51 ± 4

Table C.2: Background levels of Fe, Mn, and Al in 15 mL Falcon polypropylene vials as measured by ICP-MS for vials leached with 10 % HCl. Note that concentrations are in ppt.

6. Neutralize and dispose of acid after approximately ten uses.

These procedures apply to all containers that can be sealed. For those than cannot be sealed (beakers, for example), a 2 % HNO_3 bath for one week followed by thorough rinsing in Milli-Q water will generally suffice. If heavy cleaning of glassware is desired, a base bath must be used. This technique will not be described here.

Testing was performed on new vials and vials that had been used for previous experiments with Fe and Mn and had sat with sample solution for several months to determine what level of acid purity was necessary. Vials were leached with the specified purity, then filled with blank ultra high purity (UHP) 2 % HNO_3 for measurement with ICP-MS. For the HCl and HNO_3, reagent grade acid has been found to be sufficient for up to 10 uses (see Table C.2, although these tests also suggest that for the 15 mL Falcon brand vials, acid washing is not necessary. Certainly ultra high purity acids have been shown to not be necessary, and actually appear to make the contamination worse, although it is still quite low and this may be an artifact of normal blank fluctuations. If the procedure is desired for greater than 10 uses or with a different brand of vials, further testing should be done to ensure that there is no metal accumulation, although with initially new vials greater than 10 uses is probably not a problem. However, planning ahead so that the minimum amount of acid can be used for the desired cleaning, and establishing a regular cleaning routine with just a few common containers can drastically reduce the acid waste produced. Additionally, although these procedures can be used to regain the use of old plasticware, vials, and bottles, it is recommended that these reused containers are not used for trace metal analysis. ICP-MS analysis of old vials that sat with iron-containing solutions for months and then were cleaned using the second of the procedures above showed that some of the vials contained residual iron. There were many of the vials that were clean of iron, but the irregularity in predicting which vials will and will not have excess metals in them is not worth the risk of ruining a trace metal analysis experiment.

Finally, care should be taken while handling the containers throughout this process. Both HCl and HNO_3 are strong acids, and safety procedures should be observed at all times. Anyone using this procedure should have acid use and neutralization training. Additionally, mishandling of containers can undo the cleaning provided by this process. For example,

remember that gloves and the outsides of these containers have not been acid washed, and therefore Milli-Q rinse water should never touch the outside before the inside. The means that containers should be rinsed individually or in careful handfuls and not just dumped into a Milli-Q bucket. The same is true for caps, which are often harder to rinse cleanly.

Appendix D

Ultrafiltration

D.1 Introduction

Accurate determination of the concentration of analyte metals in solution is dependent on several factors. One important factor is quantitative measurement of the analyte, and discussion of this factor for the analytes described here can be found in Chapter 2 and Appendix A. However, measurement results can be entirely invalid if there is incomplete phase separation, for both solubility and batch sorption experiments.

Phase separation is usually achieved by either centrifugation or filtration, although filtration is somewhat more common because not all solids can be effectively centrifuged. Many authors use 0.22 μm filters, but the pore size of this type of filter is far too large for filtering nanoparticulate solids, colloids, and hydrolytic polymers. Therefore, the use of ultrafiltration filters with pore sizes less than or equal to 0.1 μm is necessary. Although ultrafiltration filters are rated based on their molecular weight cut-off (MWCO), the effective pore size can be estimated. For most applications, 30,000 MWCO filters have proven sufficient, with a pore size between 3 and 4 nm. Most of these filters are made from regenerated cellulose. The Nanosep filters described below are formed from polyethersulfone.

A potential problem in ultrafiltration is adsorption of the soluble species of interest onto the filtration membrane [106]. This adsorption may change as a function of the filter membrane material, the solute concentration, the hydrophobic nature of the solute, temperature, the solution pH, the solution species, and the length of time the solute is in contact with the filter. Filters must therefore be tested for sorption for each species in each matrix at the full range of pH values used in the experiments.

Additional problems can arise from trace chemicals remaining on the filtration membrane. In the case of the Millipore Amicon Ultra and Microcon, Pall Nanosep, and Sartorius Vivacon filtration systems, this chemical is glycerine. If there is any interaction between the analyte metal and the glycerine, pretreatment is necessary to remove it. The prescribed pretreatment for all of these filter brands is flushing with buffer (for biological applications), water, or 0.1 M NaOH followed by water. The unfortunate side-effect of pretreatment, however, is filling the holdup volume of the filter with water. This holdup volume may dilute the concentration of the analyte solution (because the filters should not be dried once wetted), and it must be determined if the glycerine or the excess water has a greater effect on the accuracy of the

final measurement. Because glycerine is water-soluble, and any metal-glycerine complexes should also be water-soluble, the glycerine is not predicted to have an effect on the metal concentration in the filtrate.

Finally, the chemical compatibility of the membranes and membrane housing must be tested. Many ultrafiltration devices are designed for use with protein and DNA recovery, and thus have not been tested with a large variety of chemicals used for other applications. Of particular interest in this study is the compatibility with hydrochloric and perchloric acids.

The testing undertaken will be presented in two different sections. The first details studies with Fe, Mn, and Al that were measured using ICP-MS. The second section covers the use of these filters for plutonium batch experiments and were measured using LSC. Several different methods of testing will be employed based on the desired use of the filters for particular experiments and the analyte metals. For transition metals the potential for concentration change comes from sorption to the filters, leaching of metals from the filter membrane or membrane housing, or sample dehydration. For plutonium the concerns are only sorption to the filters and sample dehydration.

D.2 Testing Filters With Transition Metals

Both the 0.5 and 4 mL filters are required for filtering solutions containing iron and manganese (and aluminum in the future) for solubility studies, percent composition by dissolution, and dissolution kinetics experiments. All of these solutions are measured afterward by ICP-MS, so small variations in the filter performance are readily measurable with the good limit of detection of the ICP-MS. The experiments listed above use both hydrochloric and perchloric acids, so both must be tested with similar Fe, Mn, and Al concentrations as would be commonly filtered in experiments for those experiments to be valid.

Several different types of testing were performed over the course of this work. At the start, filters were tested by filtering solutions of Fe, Mn, or Al in both 5.5 M hydrochloric acid (for dissolution kinetics) and at pH 3, 6, and 9 in perchloric acid (for solubility studies), and then comparing the concentration in the solution before and after filtering. Following some disappointing results (see below) that suggested that the metals were possibly being leached out of the filters into the solution, further testing included filtering through water and clean acid.

An important problem in these studies is the cleanliness of the receiving vial and the vial used to prepare ICP-MS solutions. For the 0.5 mL filters cleaning the receiving vial would be overly time consuming and tedious, and thus that vial was tested as a part of the filtration system. For the 4 mL vials and vials that the 0.5 mL samples were prepared in for ICP-MS measurements, the cleanliness of the vial could be both tested and, in theory, improved by acid washing (see Appendix C). However, poor vial cleanliness due to outdated acid washing procedures may have affected some of the results presented here. The vials were allowed to soak in HNO_3 for one week, which degrades the plastic, and the acid used had been previously used for acid washing a considerable number of times. This treatment may have decreased the vial cleanliness rather than increased it.

Preparation of the solution for measurement varies depending on the initial solution. For 0.5 mL filters the filtrate will need to be transfered into a 15 mL Falcon tube, acidified (if

the overall acid concentration of the filtrate is less than 2 %), and diluted to 4 mL. The final solution also needs to contain internal standard. For 4 mL filters the filtrate needs to be acidified (depending on initial acid concentration) and an internal standard added (with appropriate dilution to match the internal standard). This will allow for a better limit of detection for the 4 mL filters.

The solution put through the filters should both mimic the concentrations that would normally be sent through, and allow the limit of detection for ICP-MS to be at least 5 % of the overall solution concentration.

The ICP-MS (Perkin Elmer Elan II DRC) lists a detection limit for Fe and Mn of 0.1-1 ppt in a Class 100 clean room, and < 0.1 ppt for Al under the same conditions. The laboratory space used for preparation of these samples is nowhere near a Class 100 clean room, so one can easily assume that the actual limit of detection is about five times the listed limit. The limit of detection will also decrease due to preparatory techniques and human errors. This generally increases the limit of detection by two to ten times the listed limit. This gives an overall limit of detection range of 4-200 ppt for Fe and Mn, and less than 4 ppt for Al.

Based on the original dissolution and dissolution kinetics experiments, the concentrations of Fe and Mn are around 12-80 ppm and 700-1700 ppb, respectively. The Fe is significantly higher, but will also have a very low value for solubility experiments. Therefore, the iron range for dissolution kinetics in HCl will differ from the range for solubility in $HClO_4$.

D.2.1 Testing Results

The first testing was performed with Fe, Mn, and Al in 5.5 M HCl through 0.5 mL Microcon filters, as the filters were not rated for this high of acid concentration, but it was necessary if dissolution kinetics experiments (Section 4.4) were going to work. Metal concentrations ranged from around 75 ppt to 4 ppm. Assays of the clean acid showed no Fe, Mn, or Al, but filtration of that acid through a filter resulted in a large increase to 180 $\pm$ 30 ppb Fe, 37 $\pm$ 8 ppb Mn, and 80 $\pm$ 20 ppb Al. Additionally, the solutions of Fe, Mn, and Al all showed not only much higher concentrations of the metal that was supposed to be in the solution, but also higher concentrations of the other two metals. In fact, which solution was filtered or measured did not appear to affect the concentrations, making it unlikely that the measured concentrations came only from the solutions added.

However, the original Fe, Mn, and Al solutions also measured as far more concentrated than expected, suggesting that the HCl either leached elements from the filters or vials, or interacted in an unexpected way with the ICP-MS (experiments are normally measured in nitric acid). Because the vials for this experiment were acid washed with the outdated method described above (involving treatment with old HNO_3 for far too long) that may have damaged the plastic, it is possible that the excess metal concentration came from the vials. However, the clean acid was also measured in the same vials and was measured to be free of metals, suggesting that the metals excess came from the filters or filter housing. This excess was somewhat variable around 10 to 100 ppb Fe, 5 to 50 ppb Mn, and 5 to 300 ppb Al, and subtraction of these excesses did not reasonably account for the high metal concentrations measured. They were also so variable that a reliable subtraction was not reasonable, particularly for the Al.

Overall, the filtration of 5.5 M HCl appears to leach metals from either the filter or the filter housing. This is not surprising given the strong concentration of the acid, the fact that the filters were not rated for concentrations over 1 M, and the fact that the filters were designed for DNA assays. Fe, Mn, and Al are all common metals, and would not be expected to be controlled during the manufacturing of the Microcon filters.

The Nanosep filters, on the other hand, when measured with 1.8 M HCl showed very good agreement with the values measured for the clean acid, although the concentrations after filtering were almost always lower than those prior to filtering. Nonetheless, the difference between the two solutions was never greater than 21 ppb Fe, 0.5 ppb Mn, and 3 ppb Al. This suggests that if the dissolution kinetics experiments were resumed that the Nanosep filter would be a good choice to use, although further testing would be necessary to confirm this conclusion.

The next testing was with approximately 2.5 ppb Fe, Mn, and Al in pH 3, 6, and 9 0.1 M $NaClO_4$ solutions to test the conditions and pH range of the solubility experiments (Section 4.5 and Appendix B). The concentrations were kept low to better mimic the solubility samples. These tests were performed at all three pH conditions with the Amicon (4 mL) and Microcon (0.5 mL) filters, and at pH 6 for the Nanosep and Vivacon (0.5 mL) filters. The results of these experiments were far more promising. The solutions were measured before and after filtration. Subtracting the former from the latter did not always result in a positive number, but the majority of the samples did, implying that some of the metal was leaching out of the filter or the samples were being somewhat concentrated. In all cases the results were the most variable for Al and the least variable for Mn.

The Microcon filters were never more than 30 ppb Fe, 3 ppb Mn, and 48 ppb Al off from zero, which is still a large percentage off from what it should be, but a far lower amount off than was found with HCl. The Nanosep and Vivacon filters had a lower variability, with a maximum off from zero of 22 ppb Fe, 2.5 ppb Mn, and 60 ppb Al, but this was also only measured with a pH 6 solution. The Amicon filters, which were actually used for all of the solubility sample measurements, had a far more promising maximum difference from zero of 3 ppb Fe, 1.3 ppb Mn, and 4 ppb Al. In most cases, the concentration differences were far less than this as well. This was by far the best result of any of the filters, and was serendipitously for the filters actually needed for the experiment.

The Amicon filters were also tested with clean 0.1 M $NaClO_4$ solution at pH 7.5, and showed concentrations very close to the values measured for the solution prior to filtering. The only notable difference was a 0.5 ppb increase in Fe, which is not a very large increase.

Several experiments also tested the filter leaching using the ultra-high purity HNO_3 blank solution from the ICP-MS. The Microcon filters showed an excess metal concentration of around 58 ppb Fe, 8.5 ppb Mn, and 17 ppb Al. The Amicon filters showed an excess of 0.8 ppb Fe, 0.1 ppb Mn, and 1.7 ppb Al, all of which were very low. The Vivacon and Nanosep filters were tested with two rounds of acid through the same filter to see if the concentration would decrease with multiple treatments. The Vivacon filters gave a maximum of 3.98/2.97 ppb Fe (first round/second round), 0.18/0.15 ppb Mn, and 11.73/5.98 ppb Al. The Nanosep filters showed a maximum of 1.53/2.21 ppb Fe, 0.22/0.09 ppb Mn, and 1.71/1.64 ppb Al. Overall both filters showed concentrations far below those of the Microcon filters, which is encouraging because the Microcon filters are no longer in production. The Vivacon filters did not show much improvement with a second filtration, and the Pall filters showed a slight

improvement. However, neither improved significantly enough to recommend this as a filter pretreatment method.

Overall, these results show some important findings. The cellulose-based filters do not hold up well to concentrated HCl, but the polyethersulfone filters may hold up better. Most filters seem to perform fairly well in the pH range of 3 to 9 in a perchlorate matrix or with 2 % HNO_3 solutions, with the worst performance being for Al concentration. The worst performing filter was the Microcon filter, but this is now irrelevant because they are no longer manufactured. Both the Vivacon and the Nanosep filters had fairly clean results, but the best filter by far was the Amicon filter. Unfortunately, these are 4 mL filters, and not all samples are suitable to such a large filter. This does mean, however, that the solubility results presented in Section 4.5 and Appendix B are valid, as they were all filtered with the Amicon filter.

D.3 Testing Filters with Plutonium(VI)

Two different types of testing were performed using plutonium(VI)-239: straight filtering to determine the performance of the filters as a function of both pH and plutonium concentration, and pretreatment of the filters to determine if that performance could be improved by first flushing the filter with different solutions. These tests were carried out on two different filter types, both of which were 0.5 mL capacity 30,000 MWCO filters. The first filters are the Nanosep series from Pall, and are made from polyethersulfone (PES). They have a much lower retention volume, centrifuge cleanly, and were cited as non-complexing for plutonium by Neck *et al.* (2007) [103]. The second filters are the Vivacon 500 series from Sartorius Stedim, which are made from regenerated cellulose. These filters have a higher retention volume, but are the most similar to the filters used previously in this laboratory and by Nitsche (1991) [106]. Both filters are listed by the manufacturer as having small amounts of glycerine on the filters, and the Nanosep filters also have sodium azide.

The pretreatment options were designed to either remove the glycerine and sodium azide in case these chemicals were causing and interaction, or to saturate the filter for Pu sorption so that the actual sample would not be affected. The first two pretreatments were filtering through 0.5 mL Milli-Q water, or 0.5 mL 0.1 M NaOH followed by 0.5 mL Milli-Q water. These options were designed based on the suggestions of the filter companies for removal of glycerine. A secondary reason was to determine the effect of deprotonating any surface groups on the filters. The third pretreatment option is similar, replacing the NaOH with HCl. HCl was chosen as a good complexer to remove any metals that might interfere, and to determine the effect of protonating all of the surface groups on the filters. The final pretreatment option, hereafter called direct filtering, was to filter multiple aliquots of the analyte solution through the filter hoping to reach a number of a aliquots sufficient to saturate the surface sites for Pu sorption. This is a technique used in both Nitsche (1991) [106] and Hixon *et al.* (2010) [57] and was expected to be the most promising.

Samples for these tests contained solids with known sorption tendencies that settled well to enable a filtered and unfiltered measurement. The solids were added to increase the apparent solubility of the Pu(VI), as the plutonium might otherwise precipitate at higher pH conditions. All solutions were prepared at 1 g/L in pH-balanced 0.1 M $NaClO_4$. Pu(VI)

was added and the pH quickly returned to the desired value using small amounts of NaOH and $HClO_4$. The samples were shaken, and then allowed to settle for at least 30 minutes prior to assay. With the exception of the SBA-15 used at pH 1-4, all solids were brightly colored and thus easy to visibly verify as having settled. Aliquots were removed directly from the very top of the sample to LSC vials before and after removing larger aliquots to the filters to determine the actual solution concentration at the time of filtration. Many samples were also retained and measured again using the same pretreatment options one week later to mimic experiments that often run for at least one week.

For all experiments other than a small number at very low plutonium concentration, aliquots into the filters were 40 μL, which gave two 10 μL aliquots taken after filtration for measurement by liquid scintillation counting. This is the standard aliquot size for all plutonium experiments performed in the course of this work. For the most dilute solutions, the original aliquot was 250 μL, producing two 100 μL aliquots for LSC measurement. Because all but a very small number of experiments had the same conditions and to reflect the practical nature of the investigation, results will be expressed as either a percentage of the plutonium or as the counts per minute (CPM) in the 10 μL aliquot that was lost during filtration, which is assumed to have sorbed to the filter. This representation of the data makes it more straightforward to compare these results to other laboratory results quickly and effectively. The data for the more dilute samples were adjusted to fit this scale. For reference, a value of 5000 CPM corresponds to about 15 μM ^{2}39Pu and 1000 CPM to about 3 μM ^{2}39Pu.

D.3.1 Testing Results

Initial tests (included in Figures D.5 through D.8) suggested that both types of filters were sorbing plutonium, and thus pretreatment options were explored as described above. The results of these pretreatments are shown in Figures D.1 to D.4. The solutions ranged from 2000 to 5000 CPM, which is in the concentration range where the concentration did not appear to play a large role in the filter behavior. Note that negative values were left in and are significant, because a negative value in the following data indicates that the solution became more concentrated due to filtration.

These results demonstrate several important trends. The trends with treatment by water, NaOH, and HCl will be discussed first. The Vivacon filters more consistently lost a smaller amount of Pu than the Nanosep filters did. The Nanosep filters showed a clear pH dependence, performing better at higher pH conditions. They also performed better one week later, suggesting that Pu(V) sorbs less well to the Nanosep filters than Pu(VI) does. The Vivacon filters showed only a weak pH dependence, sorbing only slightly more at neutral to higher pH conditions, and did not show any difference between a fresh or week-old solution.

The pretreatment expected to be the best—filtering one aliquot of analyte solution through before filtering the aliquot to be measured—did not prove to be a successful pretreatment method. For both brands, and particularly for the Vivacon filters, pretreatment with the analyte solution actually increased the concentration in the subsequent aliquots. It is possible that any plutonium sorbed in the first round of filtering is then removed from the filter in the following filtration, although it did not appear that the values supported this suggestions. It would suggest that this method of pretreatment might be improved by using

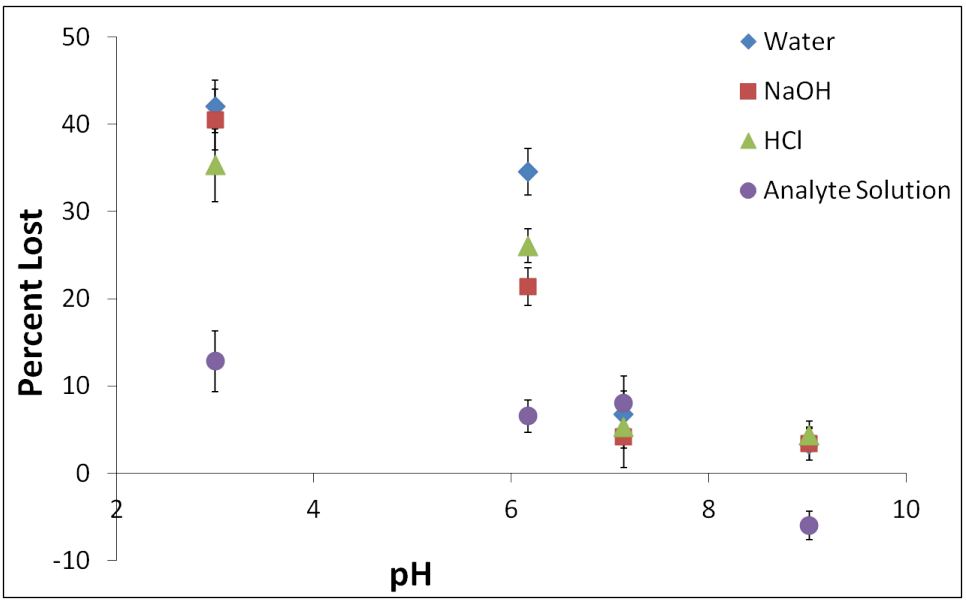


Figure D.1: Results of pretreatments for Nanosep filters measured on the same day as sample preparation, represented as the percent of the total Pu lost as a function of pH and pretreatment. Positive values indicate that Pu was lost during filtration; negative values indicate that the sample became more concentrated with filtration.

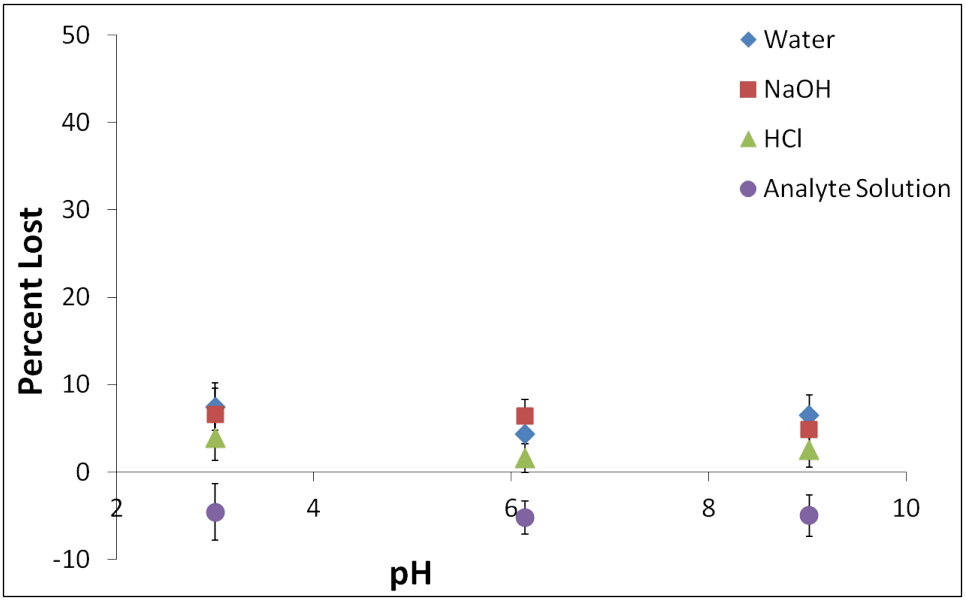


Figure D.2: Results of pretreatments for Nanosep filters measured one week after sample preparation, represented as the percent of the total Pu lost as a function of pH and pretreatment. Positive values indicate that Pu was lost during filtration; negative values indicate that the sample became more concentrated with filtration.

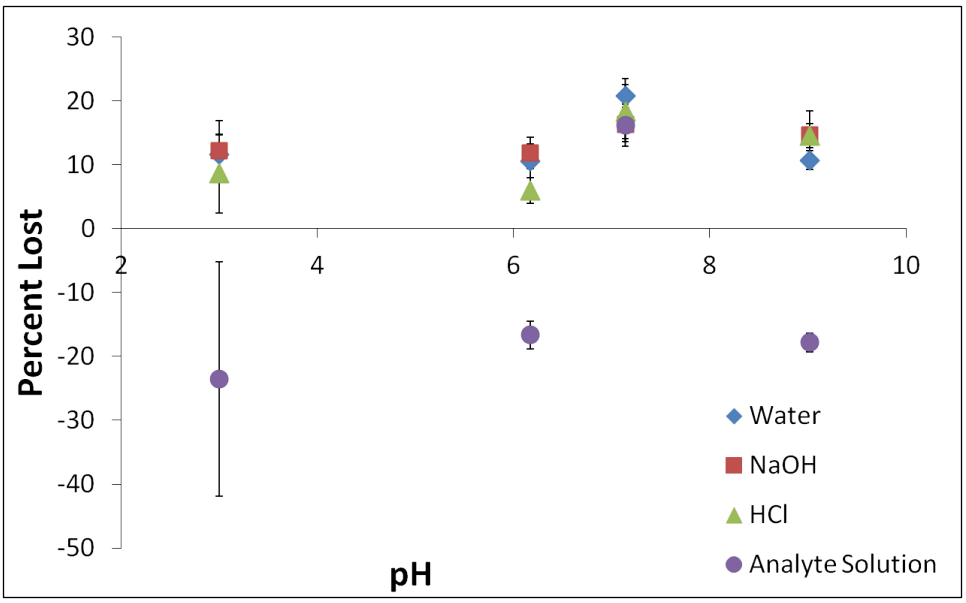


Figure D.3: Results of pretreatments for Vivacon filters measured on the same day as sample preparation, represented as the percent of the total Pu lost as a function of pH and pretreatment. Positive values indicate that Pu was lost during filtration; negative values indicate that the sample became more concentrated with filtration.

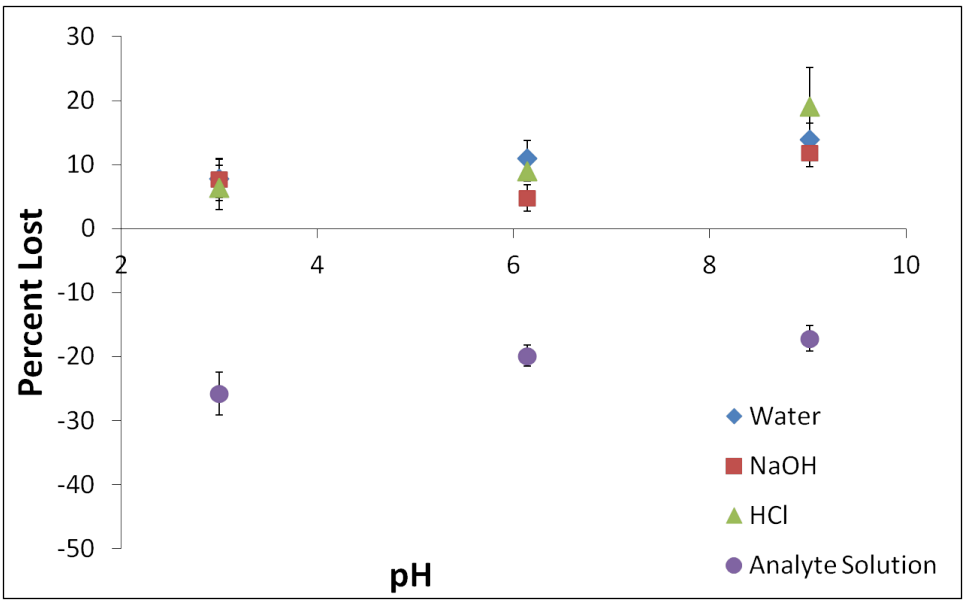


Figure D.4: Results of pretreatments for Vivacon filters measured one week after sample preparation, represented as the percent of the total Pu lost as a function of pH and pretreatment. Positive values indicate that Pu was lost during filtration; negative values indicate that the sample became more concentrated with filtration.

higher volumes of the analyte solution. However, this is not a feasible option without greatly increasing the sample sizes used for batch and kinetic experiments that are measured more than once, as it would remove too great of a volume of solution from the sample.

Based on these results, only limited further testing was performed with the Nanosep filters, as they performed significantly worse at low pH in pretreatment experiments (Figure D.1) and worse at both low pH and higher Pu concentration in direct filtering experiments (Figures D.5 and D.6). A large amount of further testing was performed with the Vivacon filters, as they were deemed more consistent and in less need of pretreatment to obtain consistent results.

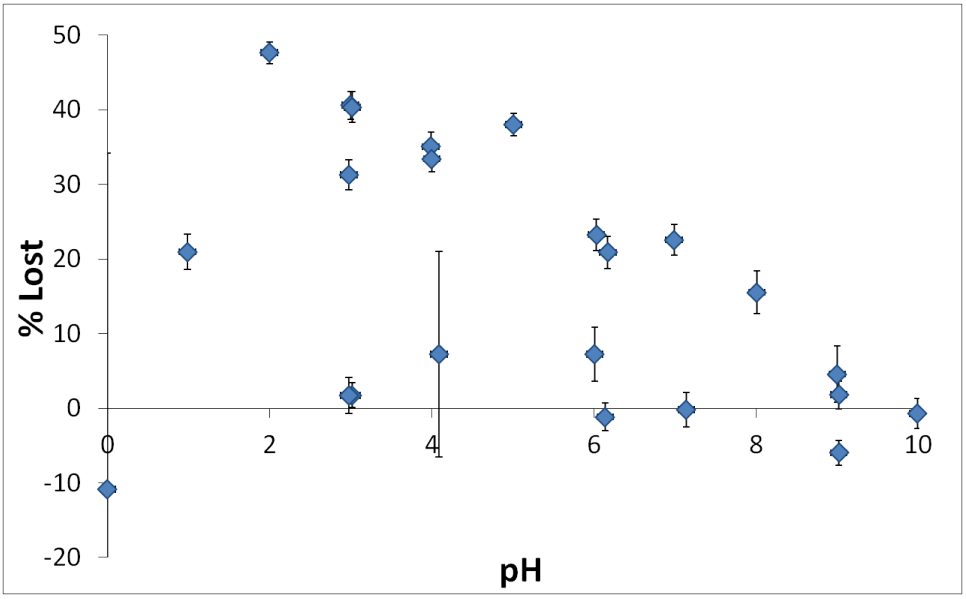


Figure D.5: Results of direct filtering for Nanosep filters, represented as the percent of the total Pu lost as a function of pH. Positive values indicate that Pu was lost during filtration; negative values indicate that the sample became more concentrated with filtration.

The behavior of the Nanosep filter performance in direct filtering experiments is shown in Figures D.5 and D.6. Both of these figures are informative for understanding the filter behavior, as the first shows the clear pH dependence and the second shows the Pu(VI) concentration dependence. Thinking about the Pu(VI) speciation (Figure 2.4), these results suggest that the PES binds well to the positively-charged plutonium species (PuO_2^{2+} and PuO_2OH^+), relatively well to the neutral species ($PuO_2(OH_2)$ and PuO_2CO_3), but does not bind well to the negatively-charged species ($PuO_2(CO_3)_2^{2-}$ and $PuO_2(CO_3)_3^{4-}$). This is not surprising given the electron withdrawing nature of sulfone functional groups.

The Vivacon filter performance in direct filtering experiments is shown in Figures D.7 and D.8. The notable trend here is the higher sorption at neutral pH, corresponding quite closely to the neutral carbonate species PuO_2CO_3. However, these were also the samples that were generally at the lowest plutonium concentration, which Figure D.8 clearly shows is the concentration range with the greatest percent sorption. Thus, from these results it is difficult to determine if the sorption is primarily due to the neutral carbonate species or the low concentration, although both are a possibility. There were also three samples, which are

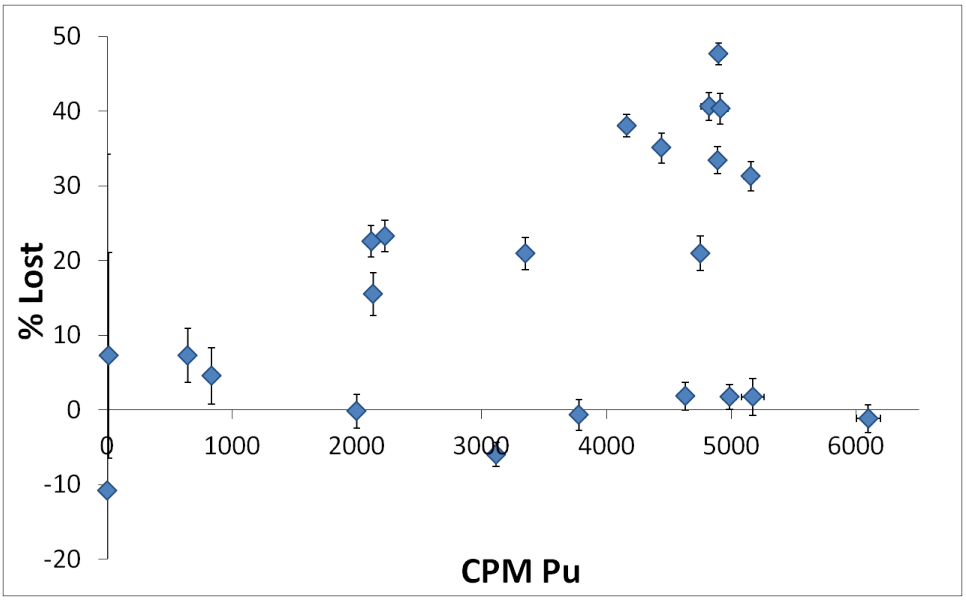


Figure D.6: Results of direct filtering for Nanosep filters, represented as the percent of the total Pu lost as a function of the concentration in CPM of Pu. Positive values indicate that Pu was lost during filtration; negative values indicate that the sample became more concentrated with filtration.

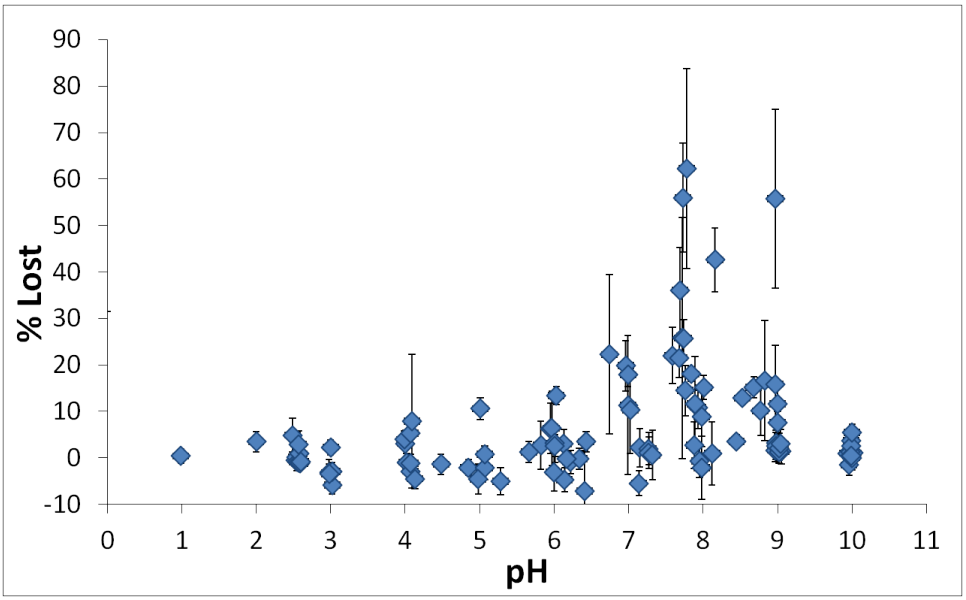


Figure D.7: Results of direct filtering for Vivacon filters, represented as the percent of the total Pu lost as a function of pH. Positive values indicate that Pu was lost during filtration; negative values indicate that the sample became more concentrated with filtration.

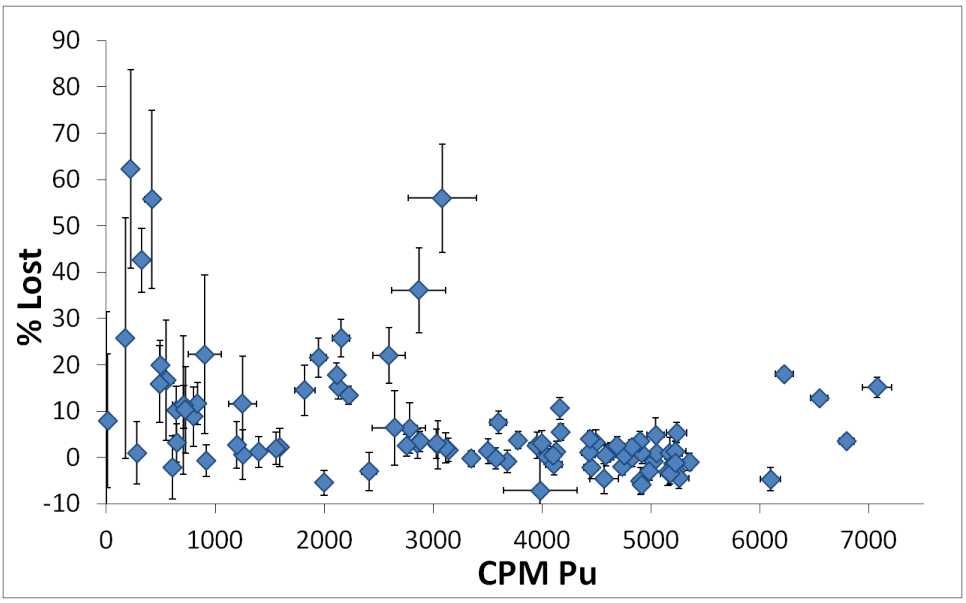


Figure D.8: Results of direct filtering for Vivacon filters, represented as the percent of the total Pu lost as a function of the concentration in CPM of Pu. Positive values indicate that Pu was lost during filtration; negative values indicate that the sample became more concentrated with filtration.

not shown on the plot, at greater than 30,000 CPM and near pH 2.5, none of which showed significant binding.

Overall the Vivacon filters proved to be fairly reliable at concentrations above 1000 CPM at pH conditions other than between pH 7 and pH 8. The two main outliers above 1000 CPM were both near pH 7.7. Particularly for mineral suspensions, the likeliest scenario is that the samples at neutral pH are also the least concentrated following a sorption experiment, meaning that the results could be heavily affected. However, in the course of this work a loss of even 50 % of the counts for those samples would only change the results of the sorption curve by less than 5 %. Because the aim of the sorption curves was to display a trend and not necessarily exact values, this level of error was deemed acceptable. Additionally, use of untreated Nanosep filters or either filter after a pretreatment would result in even worse data, making the use of the untreated Vivacon filters the best choice. Because the loss was not reproducible within a small margin, no correction was made to the data. The only condition where the Nanosep filters outperformed the Vivacon filters was at high pH and low Pu concentration. Likely the advantage of keeping a uniform filtration system for all samples outweighs the benefits switching for so few samples would impart.

In conclusion, these results show that the Vivacon filters are acceptable for general use without any pretreatment under almost all conditions as long as approximately 5 % error is acceptable. Although the ideal would be to find a filter with no sorption at all, the Vivacon filters are an acceptable substitute. The Nanosep filters should be used with more caution. It should also be noted that these results are for perchlorate matrices with primarily Pu(VI). Use of these filters with other matrices, actinides, or plutonium oxidation states should be preceded by a testing round to determine the filter performance under different conditions.

Unfortunately, as the results here were not highly reproducible and required a large number of tests for the trends to become apparent, a large number of experiments should be performed to ensure good results.